3-2020

The Effect of Passive and Active Boundary-layer Fences on Delta Wing Performance at Low Reynolds Number

Anna C. Demoret

THE EFFECT OF PASSIVE AND ACTIVE BOUNDARY-LAYER FENCES ON DELTA WING PERFORMANCE AT LOW REYNOLDS NUMBER

THESIS

Anna C. Demoret, Second Lieutenant, USAF

AFIT-ENY-MS-20-M-258

DEPARTMENT OF THE AIR FORCE
AIR UNIVERSITY

AIR FORCE INSTITUTE OF TECHNOLOGY

Wright-Patterson Air Force Base, Ohio

AFIT-ENY-MS-20-M-258

THE EFFECT OF PASSIVE AND ACTIVE BOUNDARY-LAYER FENCES ON DELTA WING PERFORMANCE AT LOW REYNOLDS NUMBER

THESIS

Presented to the Faculty

Department of Aeronautics and Astronautics

Graduate School of Engineering and Management

Air Force Institute of Technology

Air University

Air Education and Training Command

in Partial Fulfillment of the Requirements for the

Degree of Master of Science in Aeronautical Engineering

Anna C. Demoret, B.S.

Second Lieutenant, USAF

March 2020

AFIT-ENY-MS-20-M-258

THE EFFECT OF PASSIVE AND ACTIVE BOUNDARY-LAYER FENCES ON DELTA WING PERFORMANCE AT LOW REYNOLDS NUMBER

THESIS

Anna C. Demoret, B.S.
Second Lieutenant, USAF

Committee Membership:

Michael M. Walker, LtCol, USAF, Ph.D.
Chair

Mark F. Reeder, Ph.D., P.E.
Member

Levi M. Thomas, Ph.D.
Member

AFIT-ENY-MS-20-M-258

Abstract

The effect of passive and active boundary-layer fences (BLFs) on performance is evaluated on a NACA 0012 delta wing (c_{root} = 14in, c_{tip} = 2.8in, $\Lambda = 45°$, b = 23.5in) at a Reynolds number (Re) of 5.0 x 10^5 based on the root chord. The performance improvements of a passive BLF are replicated and improved upon using an active flow control (AFC) fluidic fence created by a wall-normal steady-blowing jet from a slot. The application of a passive BLF at a spanwise location of 70% z/b resulted in an 8.7% increase in C_{Lmax} compared to the baseline, with no destabilizing pitch moment characteristics and no significant change in angle of attack where stall occurs. The application of an AFC slot operating from $C_\mu = 0.49\%$ to 12.22% resulted in an increase in C_{Lmax} ranging from a 9.7% to 60.3% respectively and no destabilizing pitch moment characteristics. The blowing configuration $C_\mu = 0.49\%$ resulted in an early onset stall of -2.4°, while the configurations operating from $C_\mu = 1.95\%$ to 12.22% resulted in a delay of stall between 0.7° to 8.0° angle of attack respectively. This replication will allow for significant performance benefits at higher angles of attack (with AFC turned on), while still allowing for efficient performance at lower angles of attack (with AFC turned off). Aerodynamic performance was assessed by comparing global forces (lift, drag, and pitching moment) measured via a six-component load cell. Surface flow visualization was assessed with long exposure photos of fluorescent tufts under a black light. Overall, active flow control in the form of steady, slotted blowing is shown not only to replicate, but also to improve upon the performance gains of a passive BLF.

AFIT-ENY-MS-20-M-258

I would like to dedicate this thesis to Theodore Theodorsen, who has been a continual source of inspiration, encouragement, and home defense from squirrels. Thank you for always being the best boy.

Acknowledgements

I would like express my appreciation to my advisor, LtCol Michael Walker, for his support and assistance throughout this process. He has challenged me to grow into a better researcher and a better officer, and for that, I am extremely grateful.

My other committee members, Dr. Reeder and Maj Thomas, were helpful (and tolerant) of my incessant questions, and I am indebted to them for their valuable guidance during this process. I would also like to acknowledge the support of Mr. Joshua DeWitt in the execution and optimization of this investigation.

Finally, I must express my very profound gratitude to my family and friends for providing me with unfailing support and continuous encouragement throughout this process of researching and writing this thesis. A special thanks to my father for being a daily source of recipe advice, vaguely sympathetic “Mhmmm”s, and constant updates on his quest to make the perfect campfire stove out of old cans. A special thanks to my mother for telling me that I should stop whining and get back to work. This accomplishment would not have been possible without them.

Anna C. Demoret

Table of Contents

Page

List of Figures

Figure Page

List of Tables

List of Acronyms

AFC active flow control

AFIT Air Force Institute of Technology

BLF boundary-layer fence

BR blowing ratio

CFD computational fluid dynamic

LEVs Leading Edge Vortices

RCS Radar Cross Section

Re Reynolds number

SLPM standard liters per minute

UAV Unmanned Aerial Vehicle

THE EFFECT OF PASSIVE AND ACTIVE BOUNDARY-LAYER FENCES ON DELTA WING PERFORMANCE AT LOW REYNOLDS NUMBER

I. Introduction

1.1 Motivation

There is significant interest in improving the performance characteristics of aircraft at high angles of attack. A large-scale application of this goal is improving the performance of modern fighter aircraft, while the increasing prevalence of Unmanned Aerial Vehicles (UAVs) makes this issue just as applicable to lower Reynolds numbers. Various flow control strategies have been developed in an attempt to delay stall, increase lift performance, and minimize undesirable moment characteristics.

Passive flow control methods such as boundary-layer trips, winglets, and wing fences [1] [2] can be effective in preventing flow separation, but can be detrimental in off-design conditions. Active flow control methods, such as fluidic oscillators [3], pulsed jets[4], and fluidic fences [5] avoid this issue by only activating when required, thus avoiding the undesirable off-design results. To be practical, the benefits of these active flow control methods must be worth the additional energy required to operate them. Though popular historically, many passive flow control strategies, which involve geometric modifications that protrude into the flow, are no longer viable options for fighter aircraft that need to minimize a Radar Cross Section (RCS) or for passenger aircraft that need to minimize drag during cruise. The use of active flow control to replicate passive flow control improvements could reinstate flow control as a potential solution to avoiding separation and improving performance without the associated

drawbacks.

1.2 Problem Statement

This investigation seeks to evaluate the ability of a passive boundary-layer fence to improve the performance of a NACA 0012 cropped delta wing at high angles of attack. It also seeks to replicate and improve upon the effects of passive BLF with an active flow control fluidic fence via wall-normal, steady blowing from a single slot. Finally, it will compare these to results of a rectangular swept wing [5]. This investigation will also investigate the effectiveness of the current AFC setup to provide insight for future testing at the Air Force Institute of Technology (AFIT).

1.3 Methodology

Three configurations will be designed, manufactured, and tested to compare performance differences. These configurations will all be based on a NACA 0012 cropped delta wing. The first configuration will be a control, the second configuration will have a physical passive boundary-layer fence, and the third will have a slot through which air will be supplied to form a fluidic fence. Any change in performance will be quantified as changes in global forces (specifically lift, drag, pitching moment) via a six-component load cell. These tests will be run with the wind tunnel off and with the wind tunnel at 45 mph. Surface flow visualization will be collected using miniature fluorescent tufts, providing insight about the relative locations of steady, unsteady, and separated flow at different angles of attack. A more detailed explanation of the methodology can be found in Chapter III. Results will also be compared with previous studies.

1.4 Assumptions and Limitations

This investigation focuses on the ability of an AFC fluidic fence to improve performance of a delta wing. Very little AFC research has been accomplished with respect to swept wings and delta wings, so the focus of the investigation is less about immediate applications and more about the proof of a concept. It does not provide any recommendation about the application of this technology operationally.

The experiment involves filling an internal chamber from a pressurized air source. Data analysis does not examine the feasibility of including a fluidic fence into a normal wing structure nor the air source in an actual aircraft (bleed air from the engine, ect.). It does not include any details about how a fluidic fence would be integrated into the stability and control system.

The investigation looks to compare Walker et al's swept-wing experiment with a similar experiment with a delta wing. For this reason, a relatively thick airfoil was used, which is not directly applicable to fourth- and fifth-generation delta wing fighter aircraft. Additionally, the size and speed of the model corresponded to a Reynolds number of 5.0×10^5, while an F-22 flying at high speeds has a Reynolds number on the order of 10^8.

II. Literature Review

2.1 Straight-Wing vs. Swept-Wing Theory

Aerodynamic theory shows that a wing generates lift as air flows over the top of the wing. Typically, the majority of lift is generated at the front third of an airfoil section, with this region of low pressure often referred to as a suction peak [6]. After the suction peak, there is a region of higher pressure as one moves along the chord toward the trailing edge. As seen in Figure 1, the suction peaks align with angle of the leading-edge sweep. For a straight wing (absent leading-edge sweep), the majority of the airflow should travel parallel to the chordline, or normal to the trailing edge [7]. In the case of a straight wing of infinite length and the assumption of 2-D flow, the pressure distribution over a straight wing is identical regardless of spanwise location.

This phenomenon changes for a swept wing. The suction peaks still line up with the leading edge, but the swept leading edge of the delta wing causes the suction peaks to be offset toward the trailing edge. The peak nearest to the root chord is the furthest forward. The next peak, being further back, lines up with the higher pressure region of the first inboard peak. This causes a movement of air from the high-pressure inboard region out to the low-pressure suction peak. This spanwise momentum builds toward both the trailing edge and the wing tip. For this reason, spanwise flow near the wingtip is stronger than spanwise flow near the wing root. Subsequently, swept wings are much more susceptible to spanwise flow than traditional straight wings [8].

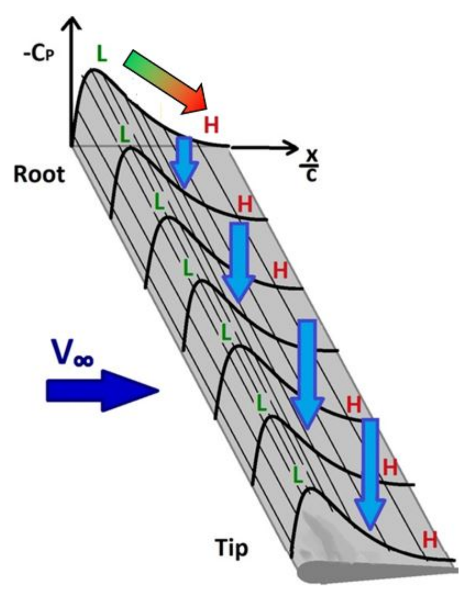

Figure 1. Suction Peak Alignment, Swept Wing

The concept of swept (or swept-back) wings were first introduced by Adolf Busemann in 1935. Swept wing theory suggests that for inviscid flow over a swept wing, the normal (chordwise) and tangential (spanwise) components of the flow can be considered independent [9]. The component of the airflow that travels chordwise generates lift and serves to increase the critical Mach number and reduce wave drag. Consequently, as the spanwise component of the flow increases, there is a reduction of lift created by the wing [9]. Spanwise flow is proportionally greatest at the wingtip, which corresponds to a decrease in effective airspeed and streamwise momentum of the flow, eventually causing the wingtips to stall. This can be especially detrimental because it means the loss of aileron control at the beginning of a stall.

2.2 Swept Rectangular Wing vs. Swept Delta Wing Theory

The two primary types of swept wing are swept rectangular wings and delta swept wings (named because the Greek letter Delta Δ resembles the triangular planform area of the wing). Delta wings have a large root chord, which allows for a high internal wing volume relative to the wing thickness. This space can be used for fuel, or in the case of this investigation, an internal chamber.

At low angles of attack, a swept rectangular wing and a swept delta wing have similar aerodynamic features, including the spanwise flow described in the previous section. As seen in Figure 2, separation and stall originate at the wingtip and propagate inward and forward toward the leading edge [10].

At high angles of attack, the main distinguishing aerodynamic feature of highly-swept delta wings (typically defined as $\Lambda > 45°$) is the generation and maintenance of Leading Edge Vortices (LEVs) [11]. These circular patterns of rotating air form when high pressure air under the wing curls around the leading edge from the pressure side to the suction side (Fig. 3). The flow separates over the sharp leading edge and

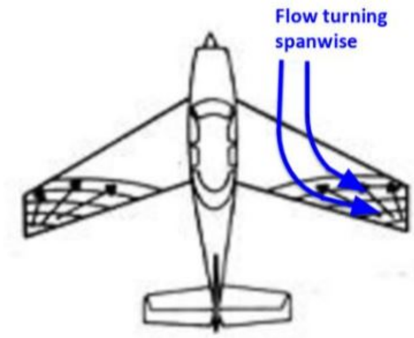

Figure 2. Spanwise Flow and Stall Propagation
[10]

reattaches to the surface of the wing further inboard. These leading-edge vortices are

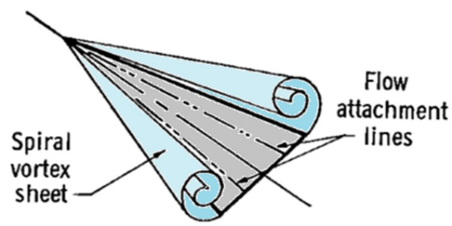

Figure 3. Leading-Edge Vortex on a Delta Wing

a source of high-energy, high-vorticity flow. The resulting low static pressure of the vortices creates a reduced surface pressure on the suction surface near the leading edge, which enhances the overall lift of the delta wing [12]. These vortices also cause additional lift generation by injecting of high energy flow through an entrainment effect (discussed further in Section 2.3.2.1). A similar lift-generation mechanism is seen in strakes and chines.

As angle of attack increases, eventually the vortices lose momentum and begin to break down, resulting in a loss of lift, an increase in unsteady flow, and wing buffeting. Spanwise flow moving across a vortex is thought to drain energy from the vortex core, which can lead to the breakdown of the LEV and the subsequent stall of the delta wing [13].

Because the present investigation uses a 45° sweep angle, which is more moderate,

the influence of the leading-edge vortex is anticipated to be much less prominent compared to previous studies with highly-swept delta wings. For this reason, the delta wing in this investigation is expected to perform similarly to previous studies with swept wings. A moderate sweep angle on a cropped delta wing was chosen for this investigation to mimic the planform shape of modern delta wings. The majority of modern fighter aircraft are some form of delta wing. The F-16 uses a simple cropped delta wing with a 40° sweep angle. The F-22, F-35, and the J-20 fifth-generation fighter aircraft all use cropped delta wings with forward-swept trailing edges with sweep angles between 34° and 47° [14].

2.3 Flow Control

Aerodynamic flow control is practice of manipulating the airflow over an aerodynamic body in order positively impact the performance characteristics. This can be accomplished passively with geometric modifications to the wing, or actively with the actuators that add momentum or energy to the flow.

2.3.1 Passive Flow Control

One option to passively improve aerodynamic performance and longitudinal static stability of delta wings is the addition of a physical boundary-layer fence (BLF), which is a flat plate fixed vertically to the upper surface of the wing. Also known as a stall fence or wing fence, these boundary-layer fences direct spanwise air back in the streamwise direction, allowing sections of the wing to continue to create lift and thus preventing the entire wing from stalling at once. The effective implementation of this concept can be seen in Figure 4, where Salmi et al. used multiple boundary-layer fences on a swept wing.

Salmi tested NACA 63_1-A012 swept wings ($AR = 8$, $\lambda = 0.45$, $\Lambda = 45°$, b = 29in)

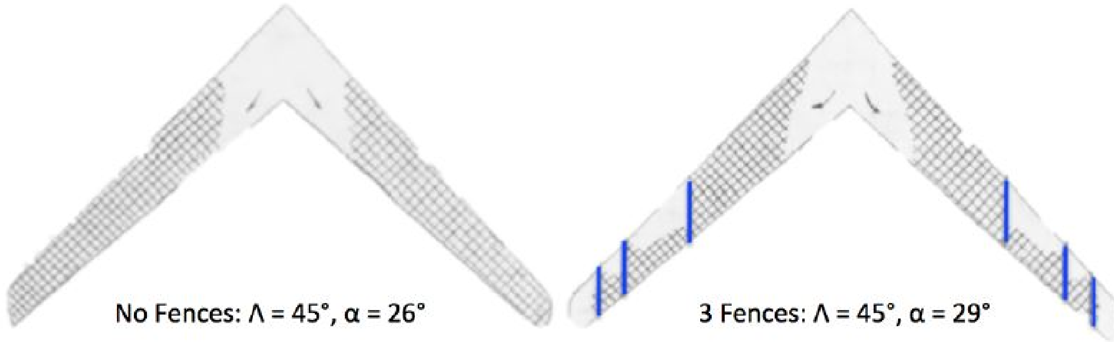

Figure 4. Effect of Boundary-Layer Fences on stall of a NACA 63_1-A012 [15]

in a 19 ft wind tunnel at a Reynolds number of 6.0 x 10^6. The two configurations pictured are the baseline at 26° and a boundary-layer fence model with three fences per side at 29°. Areas of stall are indicated with hatch marks. The lack of hash marks outboard of the blue fences indicates attached flow and thus regions that are still generating lift past the point where the baseline fence has already stalled.

Wing fences were very popular among many Soviet fighters and bombers, including the MiG-15, the MiG-17, MiG 19, MiG-21, the Tu-128 and the Tu-95. Some US fighter aircraft like the A-6 and the F-100 also featured small wing fences.

While physical wing fences and similar forms of passive flow control are effective at higher angles of attack or takeoff and landing, they reduce efficiency and performance during other stages of flight. Additionally, with stealth technology becoming a standard for modern high-performance aircraft, a fixed metal fence protruding into the flow is not a viable option when looking to maintain a sleek RCS signature. Although it would be possible to make a retractable metal fence that would only appear when needed, there is an additional cost in weight and maintenance labor to keep moving parts operational.

Boundary-layer fences still used on some U.S. modern aircraft like the Ratheon T-1 Jayhawk (Fig. 5), but they are predominantly cargo-type aircraft that need the

benefits during takeoff and landing, instead of during high angle of attack maneuvering. Though the Russian military still uses fourth-generation fighters (MiG-25, MiG-31) and bombers (Tu-95, Tu-22M, Tu-160 in swept-wing mode) with boundary-layer fences, there are no fifth-generation stealth aircraft with boundary-layer fences in any country [16].

2.3.2 Active Flow Control

Active flow control (AFC) presents a potential modern solution. Passive flow control methods are typically geometric modifications to the airframe that are always in operation, regardless of the performance improvement or loss. Active flow control involves a change in energy or momentum, and consequentially can be turned on or off. This would allow for more flexibility to "turn on" a wing fence when it can provide benefits at high angle of attacks, but "turn it off" during cruise when a fence is not beneficial. The obvious problem with active flow control is the requirement to add energy to the system to make it work, which requires more energy and cost to implement effectively. To practically implement this method, the performance benefits of an AFC must be worth the additional energy required.

The active flow control mechanism for this investigation is implemented with a

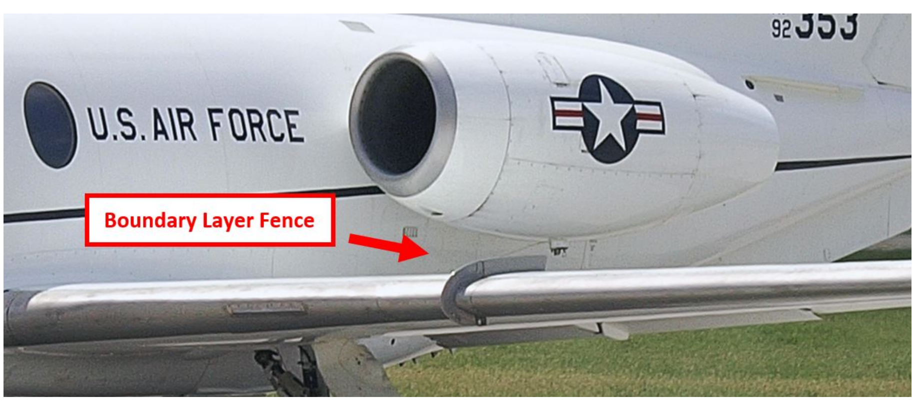

Figure 5. Ratheon T-1 Jayhawk Stall Fence
[17]

wall-normal, steady blowing jet of air from a single slot. The jet of air creates a "fluidic fence" that has a similar impact as a passive flow control physical wall, with the ability to "turn it off" when it is not required. Walker found that the fluidic fence disrupted spanwise flow like the passive BLF, with the additional benefit of entraining flow near the surface, energizing the boundary-layer and improving lift enhancement [5]. This is why an AFC fluidic fence is a better option than just an AFC physical fence (where a metal fence could pop up when needed).

2.3.2.1 Entrainment

Entrainment is a viscous effect of the interaction between two bodies of fluid of differing energy levels [18]. This phenomenon can be easily illustrated through the Dyson "Air Muliplier Bladeless Fan." As seen in Figure 6, the fan supplies the energy required to move a single unit of air through the fan and forward. This produces a jet of higher energy flow moving through the stationary air. Though air has relatively low viscosity, there is enough sheer interaction between the moving air and the stationary air that the stationary air is pulled along in the direction of the main jet. The net result is that a disproportionate amount of air (Dyson claims 15x) is moving forward compared to the energy that was put into the system: thus the amount of air seems to be "multiplied." The fan's ring design maximizes surface area for a given mass flow or exit area, thereby maximizing entrainment and increasing the effectiveness of the fan [19].

This principle is why active flow control has the potential to provide disproportionate gains compared to a passive boundary-layer fence, and thus worth the extra energy required to make the fluidic fence work. The wall of air pushed out through the slot is like the single unit of air pushed through the fan. The air along the top of the wing is also drawn toward the slot and up, which increases the strength of the

Figure 6. Illustration of Entrainment in Bladeless Fan
[19]

fluidic fence, while also energizing the flow over the top of the wing. This can be especially beneficial at high angles of attack, where the flow typically would be losing momentum and beginning to separate.

Because of the prevalence of delta wings in modern fighter aircraft, the expansion of the investigation into delta-wing type aircraft is an essential step toward the practical implementation off AFC. The overall investigation will see how the active and passive flow control methods work with a delta wing, and compare with the findings of Walker et al.'s swept rectangular wing.

2.4 Previous Studies

2.4.1 Boundary-Layer Fence Research

The passive boundary-layer fence was first used in 1938 by Wolfgang Liebe [20], and through experimental research and operational application, the designs of passive BLFs have become more effective. A 1952 NACA study by Pratt and Shields looked at various passive flow control devices on a 45° swept wing, including upper surface fences. They found that the use of a combination of fences and flaps together allowed for a 48.5% increase in maximum lift coefficient (C_{Lmax}) and a stabilization of the pitching moment characteristics. The use of a passive BLF provided a 4.0% increase

Figure 7. Multiple Wing Fences on Soviet Tu-95

in C$_{Lmax}$ when the fence located at z/b = 0.575, and a 28.7% increase in C$_{Lmax}$ when the fence was located at z/b = 0.80, as compared to the baseline. They also found that passive boundary-layer fences were shown to be more effective when wrapped around the leading edge with a span that covers entire upper surface of the wing, ending at the trailing edge [2]. There was a 21.5% increase in the maximum lift coefficient when the fence was wrapped around the leading edge and under the wing, as compared to when the fence was only on the upper surface (Fig. 8).

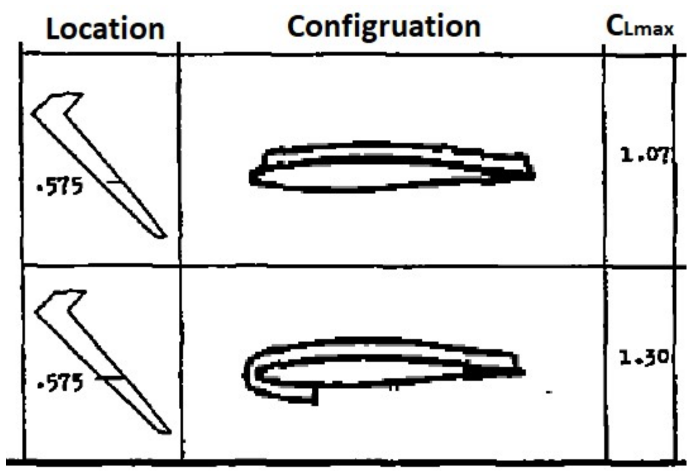

Figure 8. Performance Improvement of BLF Wrapped around Leading Edge
[2]

Pratt and Shields also found that the fence location had an impact on the performance. With the swept wing tested, the wing fence located further inboard, at z/b

= 0.575, had maximum lift coefficient that was 23.8% higher than the same fence located further toward the tip, at z/b = 0.80 (Fig. 9).

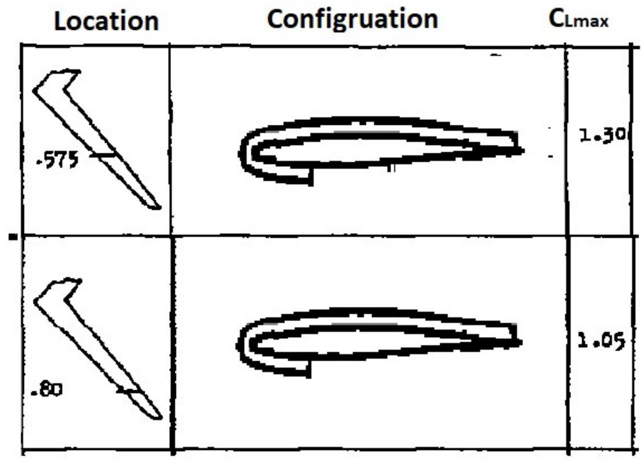

Figure 9. Performance Improvement of BLF Location
[2]

Additionally, it was found that a wing fence is most effective when placed at a spanwise location between z/b = 0.50 and 0.80, depending on aileron location to best maintain control surface effectiveness at high angles of attack [1].

There are multiple explanations as to why wing fences improve performance; reduction of spanwise flow along a wing, vortex generation near the leading edge, and alteration of the wing lift distribution [1, 2, 21].

Through computational fluid dynamic (CFD) analysis on the USAF T-38 ($\Lambda = 24°$), Solfelt and Williams et al. show that the generation of two distinct counter rotating vortices has a significant impact on success of BLF performance enhancement. The configurations with the strongest vortices saw the greatest performance improvement. It is also determined that for the T-38 wing, in agreement with previous studies, a wing fence which wraps around the leading edge of the airfoil provides the most beneficial improvement in lift performance (5% increase in C_{Lmax}) [22].

2.4.2 Active Flow Control Research

Much of the existing AFC research has been completed with respect to unswept wings, despite the fact that a large number of aircraft have some form of leading-edge sweep.

Seifert et al. investigated how oscillatory blowing was able to delay stall more effectively than steady blowing. This looked to combine two methods– jet blowing and periodic motion– to enhance boundary-layer control. Improvements depended on many parameters, including the slot location, the shape of the airfoil, and the frequency of the oscillation [23]. In 1998, he continued his work with Naveh to investigate investigated oscillatory blowing over a swept wing as a means of eliminating a separation bubble that was forming on a simulated Glauert-Goldschmied airfoil. They found the excitation slot was significantly more effective when located at x/c = 0.64 as compared to x/c = 0.59. This was because separation was occurring around x/c = 0.65, and the excitation weakens significantly with distance [24] [25].

Tewes et al. looked at a NACA 0012 airfoil on a flapped wing with an array of fluidic oscillators on the trailing edge at a x/c = 0.70. Fluidic oscillators have no moving parts, and work by funneling a steady supply of compressed air through an internal geometric chamber, which then creates alternating jets of air. Fluidic oscillators were found to be highly effective in delaying separation and improving lift performance. Tewes found that the a small number of the sweeping jets reduced spanwise flow on the wing, and substantially increased the lift performance and delayed a destabilizing pitch up stall characteristic of the wing. He proposed that the jets add momentum to the flow and act as large vortex generators, which add counter rotating streamwise vorticity to the flow [9].

Greenblatt et al. investigated the effectiveness of active flow control on straight wings and swept wings, and compared blowing slots located on the leading edge and

flap shoulder. This study was notable for its emphasis of the efficacy of AFC in the three dimensional flows experienced by low aspect ratio wings (which are commonly seen on fighter aircraft and UAVs.) These blowing slots were oriented to produce flow parallel to the wing surface. The introduction of sweep increases 3D effects. He noted that the stall location of the straight wing was inboard, while the swept wing initially stalled at the tip, which is consistent with the stall theory of each wing type. He also found that the leading-edge blowing slots increased C_{Lmax} and lift after stall, while flap-shoulder control was much more effective with unswept configurations. Greenblatt initially noted that swept wings experienced a decrease in lift enhancement near the tip. With an empirical model, he linked this poor swept wing tip performance with delta wings in the midst of vortex breakdown. The leading-edge slot re-energized the vorticies at the leading edge, enhancing the overall lift with minimal benefit at the tip [26].

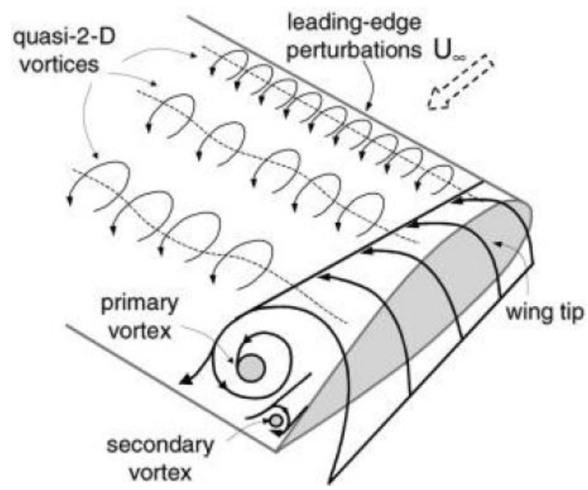

Figure 10. Leading-Edge Slot Energizing Vortex

[26]

A recent study by Walker et al. explored the effectiveness of AFC on swept rectangular wings, finding that the application of an AFC fluidic fence at 0.70 z/b was more effective than the passive BLF and the baseline wing in terms of delaying stall. He tested a 30° swept wing at a freestream velocity 38 mph, resulting in a Reynolds number of 100,000. Walker expresses his slot blowing levels in terms of isentropic blowing ratio (BR), which is calculated by dividing the averaged slot velocity (U_{slot}) by the estimated velocity at the local boundary-layer edge (U_{edge}). The BR values

have been nondimensionalized to coefficient of momentum (C_μ) in Table 1. C_μ is defined in Section 3.1.3. As shown in Figure 11), the addition of either a passive BLF or an AFC slot added to the swept wing resulted in an increase in C_{Lmax} compared to the baseline model, but the AFC model had a slightly lower peak value [5].

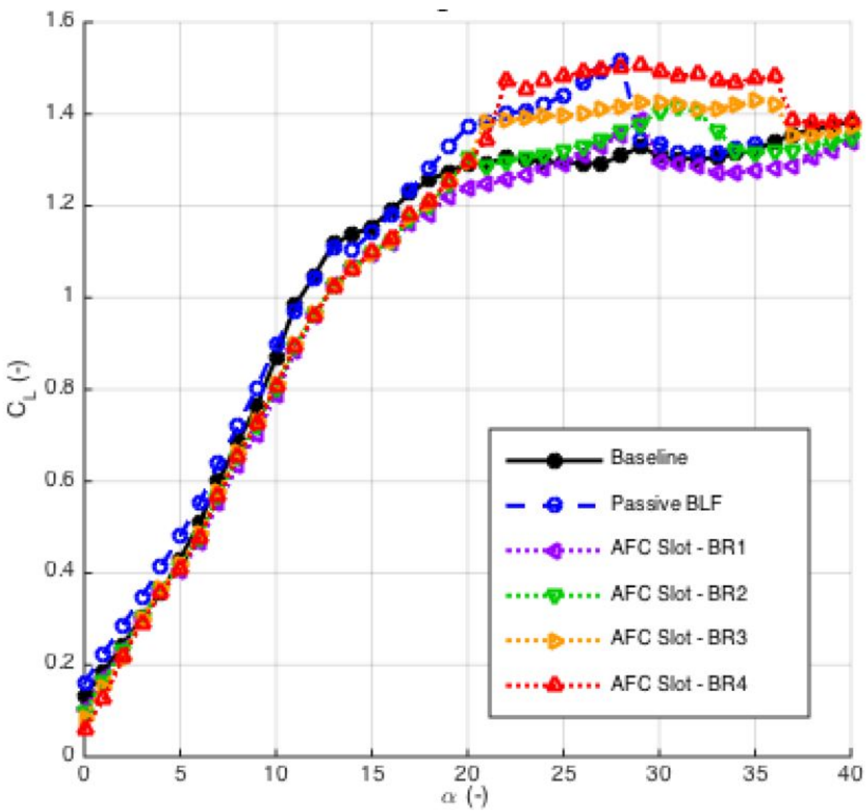

Figure 11. Walker et al. Coefficient of Lift.
[5]

Walker et al. saw a sharp increase in C_M at high angles of attack with the use

Walker et al Data, Uncorrected for Slot Forces				
Configuration	**Blowing Ratio**	C_μ	**Percentage ΔC_{Lmax}**	ΔC_{Lmax}
BLF	-	-	14.3%	0.19
Slot Model	1	0.69%	4.5%	0.06
	2	2.77%	6.8%	0.09
	3	6.23%	7.5%	0.10
	4	11.08%	12.8%	0.17

Table 1. Walker et al. Coefficient of Lift

of passive boundary-layer fences. The blue line of Walker's C_M vs. α plot (Fig. 12) shows the boundary-layer fence has a sudden increase in C_M around 27°. This corresponds to a sudden pitch up tendency when the wing nears stall. This is a destabilizing control characteristic, and one of the primary issues that Walker et al. hoped to improve with active flow control methods. As seen in the red line, for active flow control, the pitch up tendency was still present, but it was delayed by approximately 7° [5]. This pitch moment characteristic is one of the parameters that will assessed during the use of flow control on delta wings.

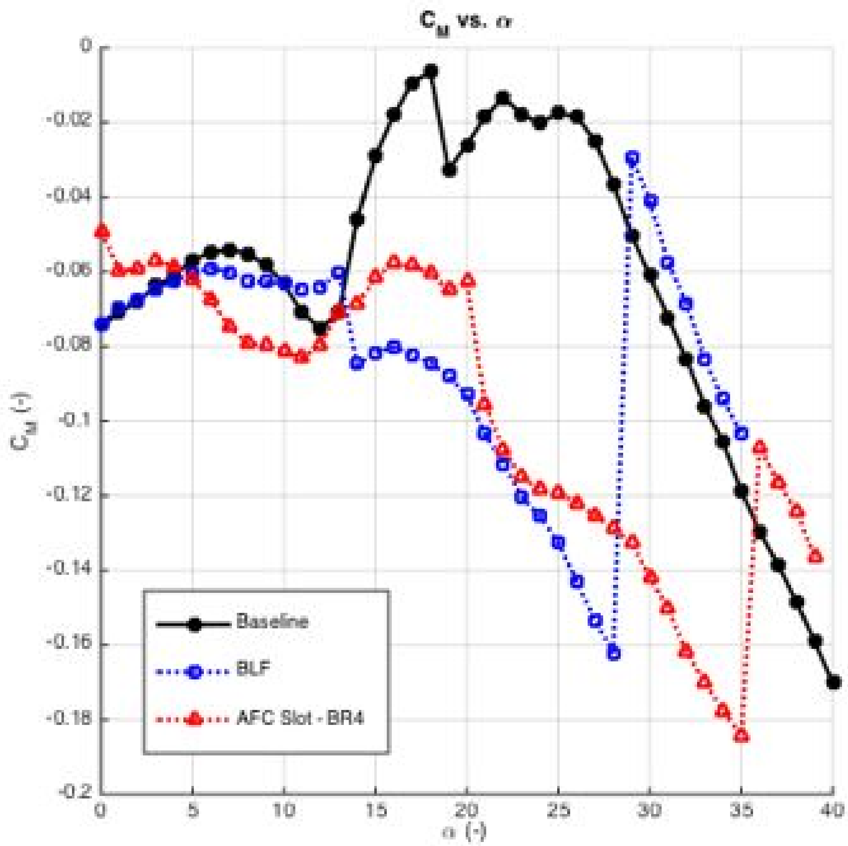

Figure 12. Walker et al. Pitch Moment Coefficient.

Additionally, Walker's stereo-PIV data revealed that passive fences created two counter rotating vortices. The tip vortex and a fence vortex both provided additional momentum and a corresponding increase in lift and delay in stall to the wing outboard

of the fence. Comparing the flow field of the passive BLF to that of the AFC slot, one can see the impact of entrainment as the flow outboard of the fence is redirected inboard toward the slot (Fig. 13).

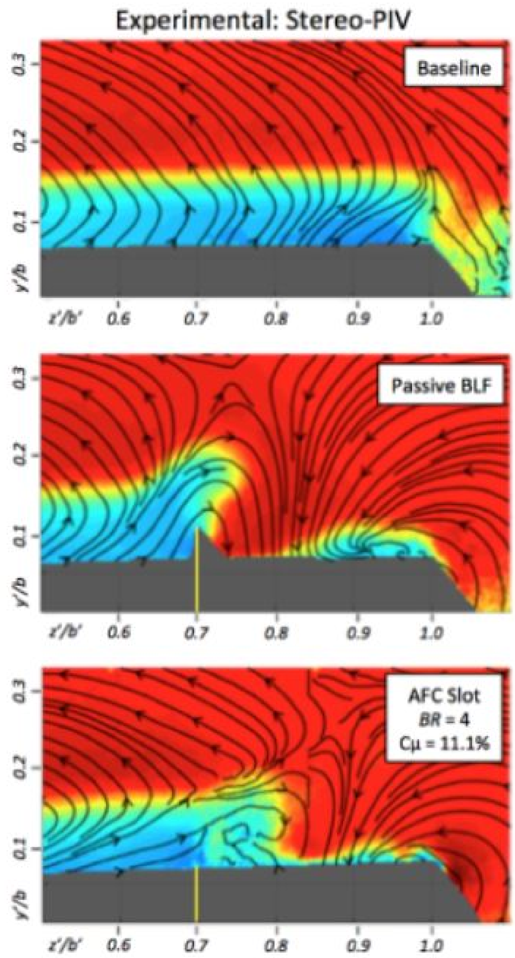

Figure 13. Walker Stereo PIV showing Entrainment
[10]

With the use of fluorescent tuft flow visualization, Walker et al. demonstrated how boundary-layer fences maintain lift at high angles of attack. At 25°, the baseline wing experienced a large region of separation, while the passive BLF and AFC slot is still attached and generating lift outboard of the fence (Fig. 14). It is also apparent that the BLF model has a greater separated region inboard of the fence compared to

the AFC model. Looking at the direction of the tufts, there is evidence of entrainment as the tufts inboard have been directed towards the AFC fence.

In his investigation, Walker et al. used mini-tufts glued to his model. Less intrusive tufts (which are typically smaller, with finer thread, and are glued to the model) allow the model to perform very similarly to the "clean" model without tufts. There is some variation in the technique when using tuft visualization. For this investigation, one set of models was manufactured. To preserve the potential of using the "clean" models for future testing, the tufts were taped instead of glued to the model. This meant that there was a section of tuft under the tape that was fixed in the streamwise direction, which impedes movement more than if just the tip of the tuft was glued to the surface. There was also a risk of the tuft getting caught on the edge of the tape behind it. [27]

A study performed by the University of Washington was published in Barlow's *Low Speed Wind Tunnel Testing* which examined the impact of various flow visualization methods on an airfoil's stall characteristics. It found that gluing mini-tufts to the model caused the least deviation of the stall characteristics. The use of glued No. 60 tufts, which is a thicker thread compared to a mini-tuft, caused a 0.4 decrease in the C_{Lmax} value, but very little variation in the angle of attack where stall occurred. Using taped No. 60 tufts caused an additional reduction C_L by 0.3, with stall occurring about 1° earlier [27]. This is significant because it allows the current investigation to examine a specific angle of attack in the tuft data and relate it directly to the original study (ie. it appears stall occurs at 25° in the data; what is happening at the 25° flow visualization photo?).

According to *NASA's Contributions to Aeronautics*, the X-48B subscale demonstrator, being a blended-wing body (BWB), may represent the next extension of the swept rectangular wing and the swept delta wing. Like delta wings, this blended

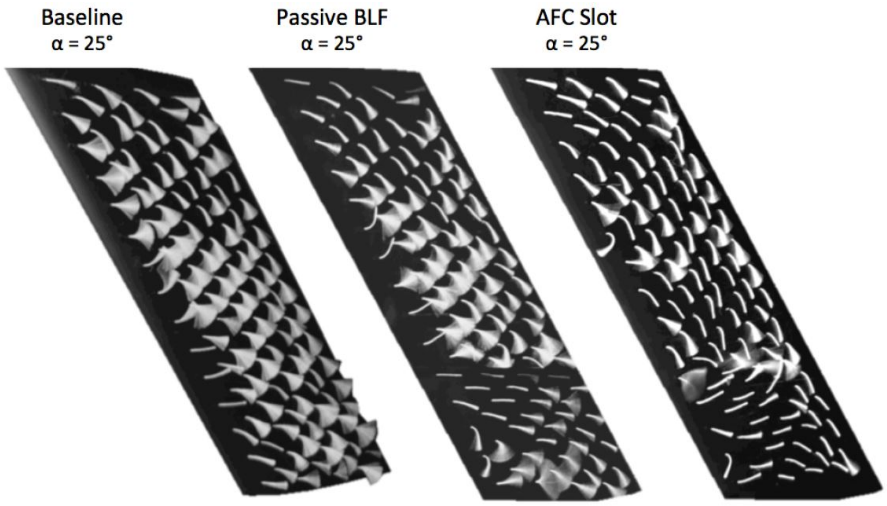

Figure 14. Walker et al. Flow Visualization Data.

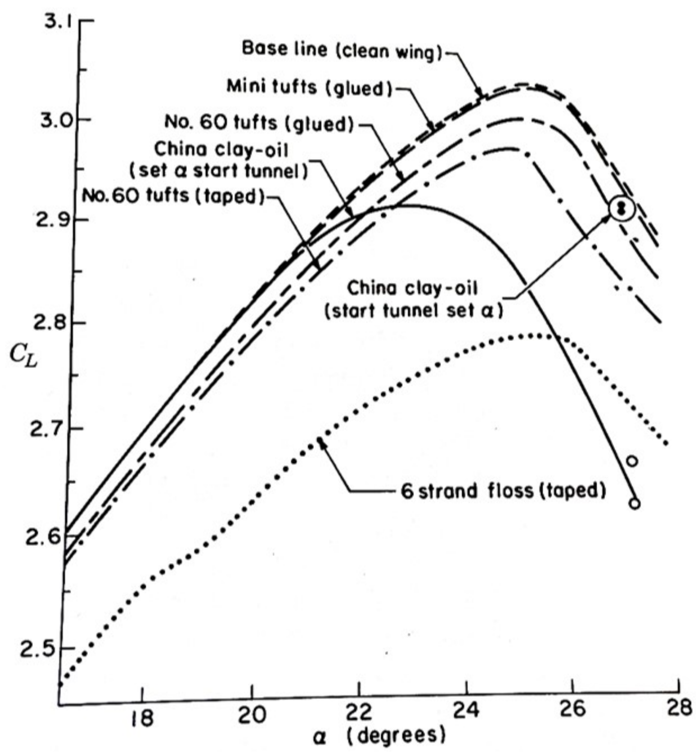

Figure 15. Effect of various tufts, china clay, and oil flow on lift curve near stall [27]

body has a large payload volume. It experiences spanwise flow, but also has many of the stall characteristics of a swept rectangular wing. The X-48B project was a collaboration between NASA and Boeing that highlights a shift in the aerospace industry

away from the transitional tube fuselage and wing design [28].

Figure 16. NASA Subscale X-48B
[28]

Continuing this trend in 2020, Airbus released the MAVERIC, a small-scale prototype that promises to generate of fuel savings of up to 20%. The press release specifically cited “low-speed and stall dynamics” as a specific challenge that future testing would focus on [29]. At low speeds (ie. during takeoff and landing) is a region where a boundary-layer fence would provide performance improvement. However, an airliner spends the majority of the flight time in a straight-and-level cruise configuration, where a physical wing fence would just be adding drag. The airline industry is hyper-focused on drag reduction, so active flow control could provide the performance benefit without the drag penalty.

A computational study by Ceron-Munoz et al. looked at the use of various passive flow control devices, including multiple wrap-around wing fences, on a blended wing body. They were attempting to reduce spanwise flow, but did not find wing fences to

be an effective solution. Looking at the streamlines of the computational solution in Figure 18, it appears that the presence of three fences is interfering with the leading-edge vortex of the blended wing. The study attributes this change to flow separation occurring on the external wing, while the center body is still producing lift [30].

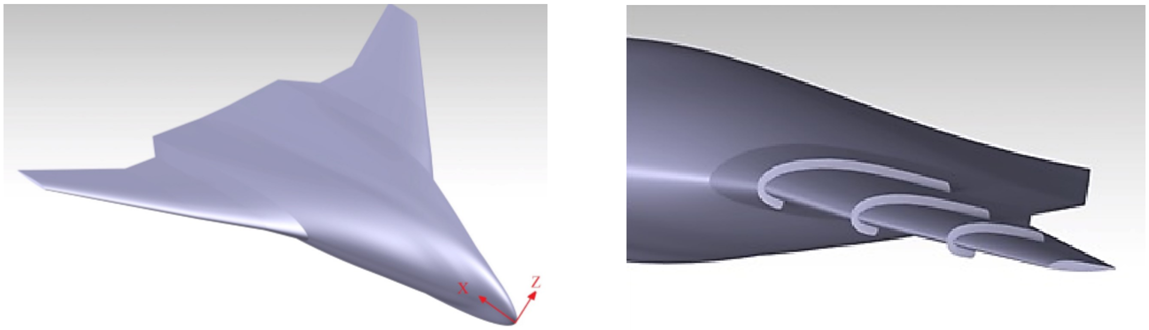

(a) Baseline Blended Wing Body

(b) Wing Fences on Blended Wing Body

Figure 17. Ceron-Munoz Blended Body Test Configurations
[30]

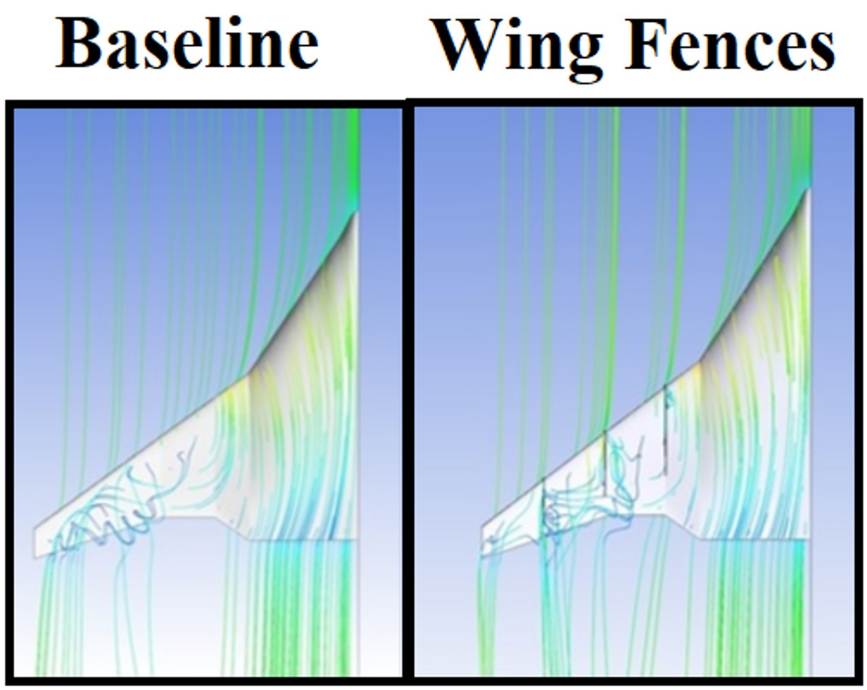

Figure 18. Streamlines
[30]

III. Methodology

3.1 Facility and Equipment

3.1.1 Wind Tunnel

Experiments were conducted in the AFIT open-circuit low-speed wind tunnel. It is located in Building 644 room L154 and was constructed by Aerolab. The tunnel test section measures 41 in. (1.041 m) wide by 33 in. (0.838 m) high, including 3-sided optical access, and may attain airspeed up to 150 mph (67.1 m/s) or M = 0.2, within the range of incompressible flow. The transverse velocity distribution across the test section and within the boundary-layers is typically within 1.0% of the mean, and the turbulence measured at the test section centerline is less than 0.1% at full speed. A schematic of the wind tunnel is shown in Figure 19.

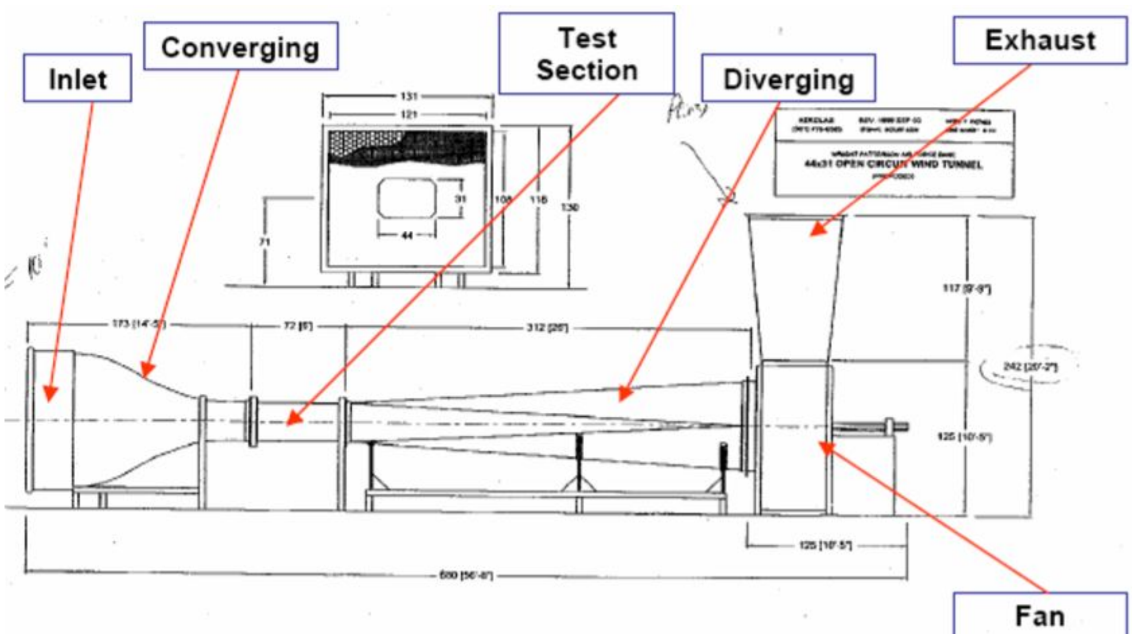

Figure 19. AFIT Low Speed Wind Tunnel Schematic (DeLuca 2004:26)

3.1.1.1 Sting Setup and Force Balance

For global force and moment measurements, the AFIT six-component force balance (via sting mount) capable of measuring forces up to 50 lbf in the normal and 10 lbf in the axial directions is used. The sting mount is screwed to an internal connection piece, with fits into the aft end of the wing model and is secured with an upper screw. This data allow for creation of lift, drag, and pitch moment plots with respect to angle of attack and will be used to determine the performance of each wing configuration. Below are the equations for lift and drag as a function of normal force (N) and axial force (A), assuming that there is no sideslip. Note that in this case, α refers to the angle of attack of the sting, not the model itself.

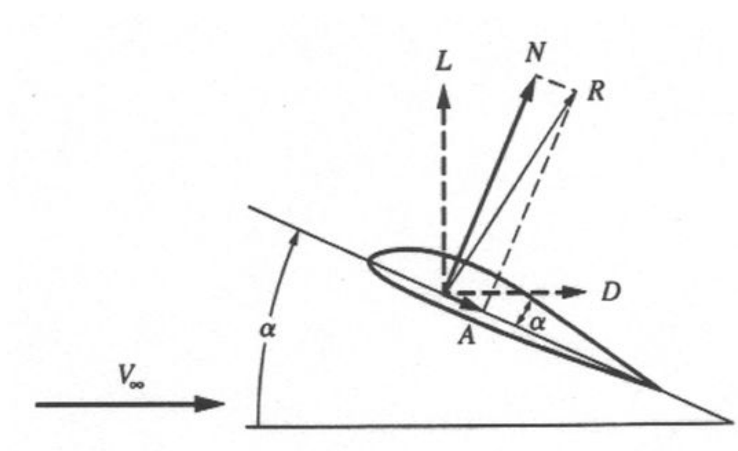

Figure 20. Components of Aerodynamic Force

$$D = Nsin(\alpha) - Acos(\alpha) \tag{1}$$

$$L = Ncos(\alpha) - Asin(\alpha) \tag{2}$$

Lift (L), drag (D), and pitch moment (PM) were nondimensionalized using density (ρ), freestream velocity (V_∞), the planform area of the wing (S), and the mean chord

of the wing ($\bar{c}$).

$$C_D = \frac{D}{\frac{1}{2}\,\rho\,V_\infty^2\,S} \tag{3}$$

$$C_L = \frac{L}{\frac{1}{2}\,\rho\,V_\infty^2\,S} \tag{4}$$

$$C_M = \frac{PM}{\frac{1}{2}\,\rho\,V_\infty^2\,S\,\bar{c}} \tag{5}$$

3.1.2 Airfoil and Wing

The NACA 0012 laminar airfoil was chosen for the wing model in this investigation. The aircraft was designed in Solidworks as two wings and a fuselage. It was 3D printed in VeroClear material using a Stratesys Objet Eden 500v 3D printer. These pieces were epoxied together and sanded at the AFIT machine shop. The model was painted black to provide contrast for the fluorescent tuft visualization and also to strike fear into the hearts of men. In the present study, the selected Reynolds number is 500,000 based on the wing root, resulting in an approximate freestream velocity 45 mph (66 ft/s or 20.1 m/s). The root chord of the wing is 14 in, the tip chord is 2.88 in, with a 45° sweep angle and a wing span of 23.5 in.

Due to design constraints, the model was built with the sting connecting at a -7.82° degree offset relative to the centerline of the body. In Figure 21, the offset is visible in the fuselage, and the internal chamber can also be seen.

From the nose, the mounting block connection point is 7.5 in behinds the nose of the model. Based on the Solidworks model of the baseline model, the center of gravity (CG) is 6.8 in behind the model nose. The aerodynamic center is defined as the location where (on average) there is no change in pitch moment with respect to changes in α. This was calculated by looking at the linear region of the baseline model C_L vs. α plot, which was 0° to 20° in terms of the sting, or -7.82° to 12.12° in terms of the model (with the -7.82° angle offset factored in.) Within this linear

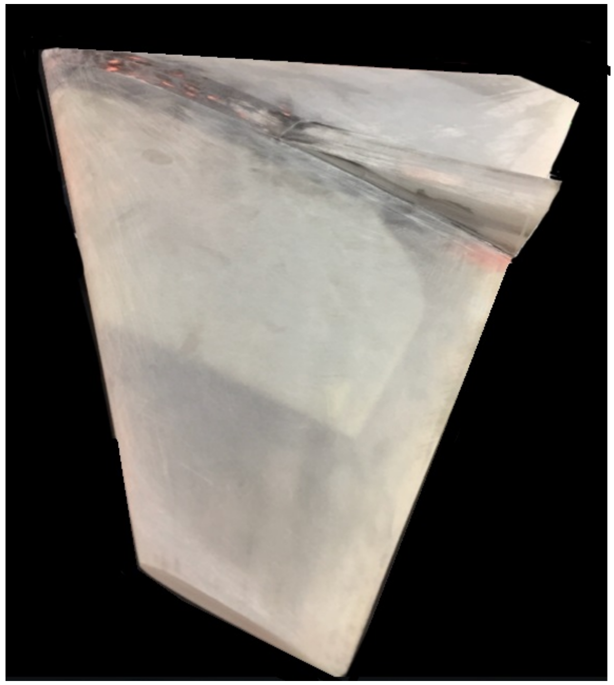

Figure 21. Baseline Model, Before Painting

region, the pitch moment was plotted and fitted with a first order polynomial. An aerodynamic center value was entered, and the slope of the curve fit was calculated. The AC was iterated until the $C_{M\alpha}$ slope value was equal to 0 within a tolerance of 0.0001. The calculated AC is located 8.686 in behind the model nose. This AC value was recalculated at other Reynolds numbers for additional validation. The airfoil geometry is presented in Fig. 22.

Based on a preliminary study, the fence and slot configurations were both located at z/b = 70%. This location provided the largest performance gains for the configuration tested. The fence height is 60% of the maximum thickness of the airfoil at the fence location (0.6 t_{max}). Based on the previous studies discussed, both the passive boundary-layer fence and the active flow control slot would wrap around the leading edge to 0.25 x/c. However, the slot only spans from 0.25 x/c on the pressure side to 0.75 x/c on the suction side due to internal geometric constraints of the wing. Because of structural constraints, the slot will not reach all the way to the trailing

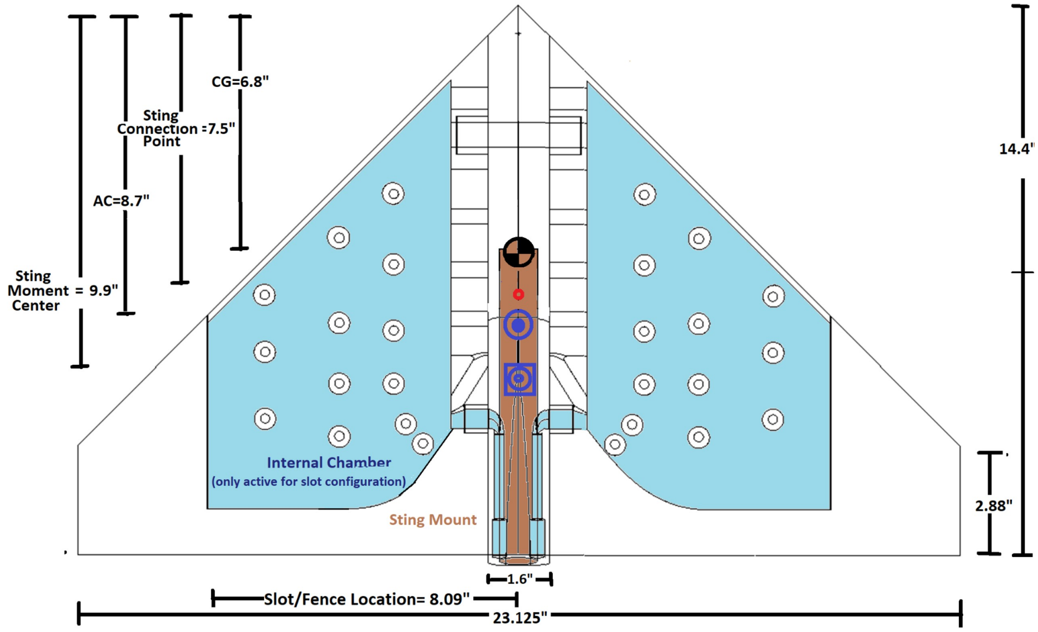

Figure 22. Boundary-Layer Fence Model

edge, and only covers the front 75% of the upper wing chordline at the 70% span. To prevent flexing in the wing outboard of the slot, additional tear-drop shaped supports were placed spanning the internal the width of the slot. The Solidworks models of the final configurations can be seen in Figure 24.

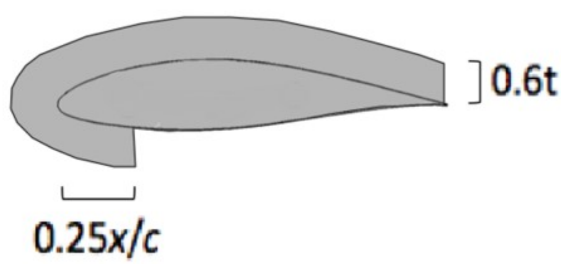

Figure 23. Boundary-Layer Fence Geometry

3.1.3 Active Flow Control Setup

By definition, active flow control requires additional energy to operate. In this experimental investigation, the additional energy comes in the form of shop air being

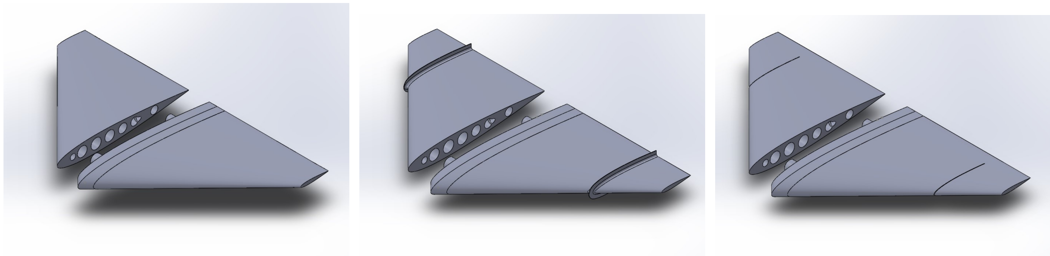

(a) Baseline Configuration (b) Fence Configuration (c) Slot Configuration

Figure 24. Experiment Configurations

pumped into the two internal chambers inside each side of the delta wing, which then flowed out of the slots to make the two fluidic fences. To help provide a uniform distribution of air coming out of the slot, a large internal chamber was used, and the internal structural supports were placed to break up the flow path of air pumped into the back of the model. To help insure equal strength fences, the two internal chambers are entirely independent and are connected to different mass flow controllers (Fig. 44). Two identical 1500 standard liters per minute (SLPM) Alicat Mass Flow controllers were used. Plastic hoses connected the mass flow controller to a connector which then locked to sections of copper pipe that had been epoxied into the back of the model (Fig. 25).

As previously stated, active flow control is implemented in the form of wall-normal, steady blowing from a single slot that is placed directly where the passive BLF existed. The slot is measured to be 0.037 in (1mm) wide and 6.850 in (174mm) long. Internally, the slot is 0.197 in (5mm) deep to allow for flow to exit the slot normal to the wing surface.

The momentum coefficient (C_μ) calculation incorporates the slot area (A_{slot}), the wing planform area (S), the volumetric flow rate through the slot ($\dot{V}$), the freestream velocity (V_∞), and the assumption of incompressible flow ($\rho_\infty = \rho_{slot}$).

$$C_\mu = \frac{\dot{m}_{slot}\ V_{slot}}{\frac{1}{2}\ \rho_\infty\ V_\infty^2\ S} * 100 \tag{6}$$

where

$$\dot{m}_{slot} = A_{slot}\ \rho_{slot}\ V_{slot} \tag{7}$$

and

$$V_{slot} = \dot{V}/A_{slot} \tag{8}$$

resulting in the final equation for C_μ:

$$C_\mu = 2\ \frac{A_{slot}}{S}\ \frac{\rho_{slot}}{\rho_\infty}\ \frac{(\dot{V}_{slot}/A_{slot})^2}{V_\infty^2} * 100 \tag{9}$$

With the known volumetric flow rates through the slot exit of 200, 400, 600, 800, and 1000 SLPM, the resulting momentum coefficient values are $C_\mu = 0.49\%$, 1.95%, 4.40%, 7.82%, and 12.22%. This terminology for C_μ is also used by Walker et al and others in the literature [5].

3.2 Data Acquisition

3.2.1 Global Wing Force via Force Balance

Each trial began with the nulling of the balance, and then the collection of a tare file. With the tunnel off, the sting was moved through the angles of attack that would be collected during the trail, and global wing forces were measured over a period of twenty seconds at 1 Hz. The resulting tare file would be subtracted from the actual trial, allowing the final data file to neglect the weight of the model and only report the aerodynamic forces and moments. The standard angle of attack range used in the lab was from 0° to 40°. (Due to the -7.82° angle offset of the model, this was -7.82° to 32.18° relative to the centerline of the model.) From 0° to 18°, data was taken at

Figure 25. Slot Air Setup

1° increments. From 18° to 40°, data was taken at 0.5° increments to get a higher data resolution near stall.

3.2.2 Surface Flow Visualization via Mini-tufts

For surface flow visualization, mini-tufts (Fig. 4) are applied to the suction surface of the wing. Originally developed by Crowder et al. circa 1980, the fluorescent mini-tuft technique allows for minimally-intrusive flow visualization in wind tunnel testing [21].

The mini-tufts are 0.3 in long lengths of monofilament nylon thread attached to the left side of the delta wing temporarily with strips of black scotch tape using the tuft board technique outlined in *Low Speed Wind Tunnel Testing*, Chapter 5.3 on "Surface Flow Visualization" [27]. The tufts are oriented in the streamwise direction. The tufts are spaced 0.35 in apart along the effective chord and spanwise directions,

creating a skewed grid that aligns with the streamwise freestream flow. This tuft orientation facilitates the determination of crossflow angles (measured relative to the effective chordline) [5].

Once the tufts were affixed to the wing, the model was placed in the wind tunnel and all ambient lights were turned off in the wind tunnel room. A black light was installed above the wind tunnel, and a cellphone was positioned above the wind tunnel, pointing down through a clear panel. The Slow Shutter Version 4.9.2 application was used to take a 4 second long exposure photo. The light sensitivity was set to 1/4, the ISO was automatic, the capture mode used was Light Trail, and the Boost setting was activated.

Initial photos were found to have a strong glare and pink overtones, as seen in Figure 26a. By taking the photos through a protective UV face shield, these issues were largely resolved (Fig 26b). Though this provides a convenient and low-cost filter, the curved surface of the shield has the potential of producing distortion. A section of the *Handbook of Flow Visualization* describes the selection of exciter and barrier filters that spectrally separate the light such that the illumination is increased without increasing the excitation light intensity [31]

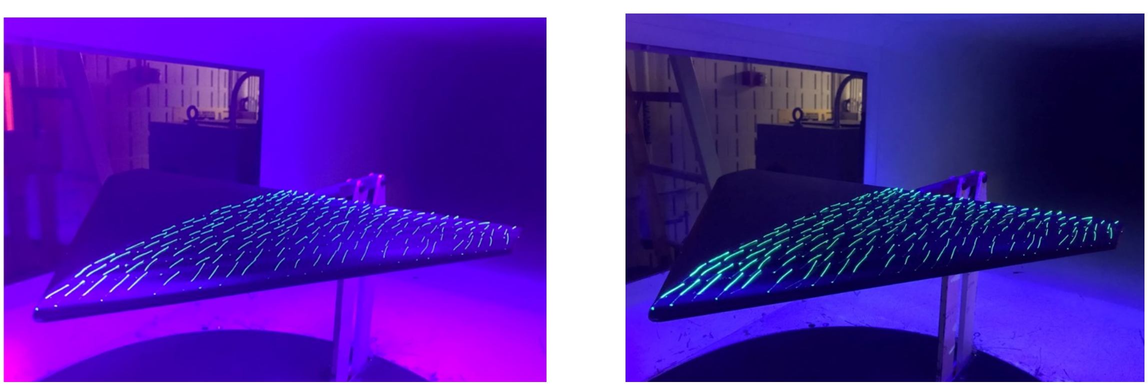

(a) Original Photo. (b) Photo Taken Through UV Face Shield.

Figure 26. Flow Visualization Setup

The three models (baseline, fence, slot) were run through the normal angle of

attack profile (0° to 40°), with one photo taken at every degree increment. The use of a long exposure photo gives an indication of flow direction, flow separation, and stall. Tufts that remained stationary or pointing in the direction of the freestream were assumed to be attached. When the flow is separated and therefore unsteady, the tuft moves in a fanning motion and creates a coned imaged. Figure 27 shows different levels of tuft disturbance. Typically, the presence of reverse flow indicates flow separation [5].

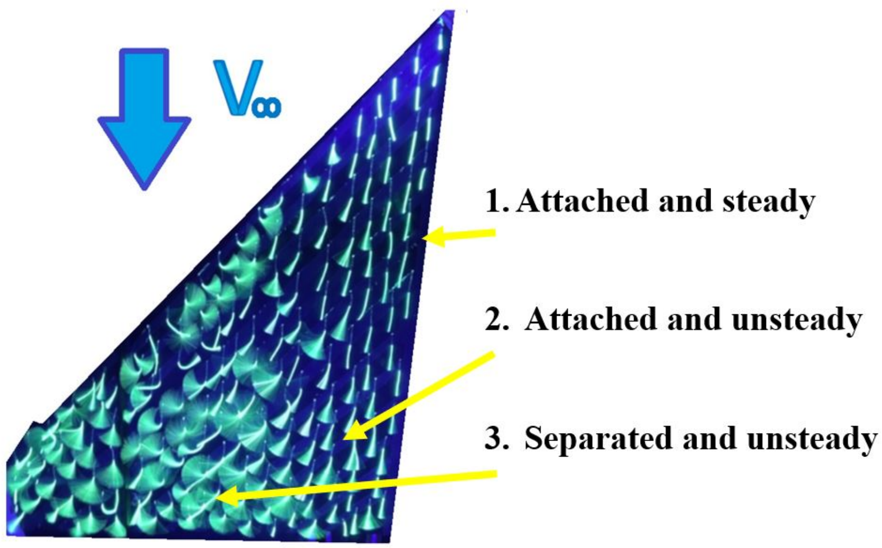

Figure 27. Example of Separated Flow Visualization using Fluorescent Tufts

3.3 Data Processing

The full MATALB code file can be found in Appendix A. The process for processing the load cell data is outlined below.

1. Import data file and tare file
2. Identify room conditions and model specifications
3. Apply solid body blockage corrections due to wing and fuselage

4. Subtract Tare Data from Main Data File
    (a) Load the static tare data for the alpha sweep without the wind
    (b) Separate each force from the file
    (c) Fit data to a 4^{th} order polynomial as an x-y plot (α vs. Force) for each of the 6 force sensors
    (d) Subtract the effect of the static weight (ie. tare files) with the tare polynominals
5. Correct forces and moments for balance interactions with manufacturer specified K matrix
6. Calculate axial, side, and normal forces from the corrected balance forces in the body axis reference frame
7. Make relevant corrections
    (a) Wind speed correction
    (b) Solid body blockage corrections due to wing and fuselage
    (c) Drag coefficient correction
    (d) Angle of attack due to upwash correction
    (e) Pitch moment correction
8. Verify Mean Aerodynamic Chord (MAC) by plotting C_M vs. α; slope should be approximately zero.
9. Plot data

3.3.1 Tare Files

As was outlined in Section 3.2.1, the first step of each run was to take a tare file, where the configuration was swept through the standard 0° to 40° profile with the wind tunnel off. After that, the actual data file was taken at 45 mph. During data processing, the tare file was subtracted from the data file, resulting in the net impact of the different configurations without factoring in the weight of the model. Table 2 provides breakdown of the data file/ tare file combinations, and what conclusions could be drawn from each.

Model	**Data File (Sweep from -7 to 33 deg)**		**Tare File**		**Goal "Determine the..."**
	Speed	**Setup**	**Speed**	**Setup**	
Baseline	45 mph	-	0 mph	-	Net Impact of Baseline
Fence	45 mph	-	0 mph	-	Net Impact of Fence
Slot (all SLPMs)	45 mph	Slot air on, Hose on	0 mph	Slot air off, Hose on	Net Impact of Slot
Slot Model Setup In	0 mph	Slot air off, Hose on	0 mph	Slot air off, Hose on	Impact of Hose
	0 mph	Slot air on, Hose on	0 mph	Slot air off, Hose on	Slot Air Forces

Table 2. Tare Breakdown

3.4 Experiment Accuracy and Uncertainty

All quantitative measurements were taken through the AFIT 6-DOF sting-mounted balance. The The standard for assessing uncertainty for low speed experimental wind tunnel results was the root-sum square method, which is outlined in a 1953 paper from Kline and McClintock [32]. The uncertainty of the C_D and C_L was assessed at the Reynolds number of 5.0 x 10^5. The preliminary study also involved testing at a higher speed (60 mph) which gave a Reynolds number of 6.6 x 10^5 based on the root chord. At higher speeds, the lift and drag components were higher, which made the

bias and precision errors proportionally less impactful and the resulting total uncertainty is lower. However, because the standard test Reynolds number was 5.0 x 10^5 for the entire main investigation, the uncertainty analysis was focused on that test condition.

This uncertainty method involves taking the equation for the parameters C_D and C_L, and breaking them into the variables that were measured in the wind tunnel. The variables for calculating C_D and C_L are the unresolved normal force measurement on the balance in pounds (N), the unresolved axial force measurement on the balance force in pounds (A), the freestream velocity of the wind tunnel (V_∞), and the density of the freestream velocity (ρ_∞)

This procedure is outlined below for the calculation of the uncertainty of C_D.

$$C_D = \frac{N sin(\alpha) - A cos(\alpha)}{0.5\ \rho_\infty\ V_\infty^2\ S} \tag{10}$$

The partial of equation 10 was taken with respect to N, A and V_∞.

$$\frac{\partial(C_D)}{\partial(N)} = \frac{sin(\alpha)}{2\ \rho_\infty\ V_\infty^2\ S} \tag{11}$$

$$\frac{\partial(C_D)}{\partial(A)} = \frac{-cos(\alpha)}{2\ \rho_\infty\ V_\infty^2\ S} \tag{12}$$

$$\frac{\partial(C_D)}{\partial(V)} = \frac{4\ (A\ cos(\alpha) - N\ sin(\alpha))}{\rho\ V_\infty^3\ S} \tag{13}$$

$\bar{c}$	0.825
S	1.385 ft^2
$\mathbf{V}_\infty$	66 ft/s
T	70 $°F$
$\mathbf{P}_{barometric}$	28.95 inches Hg

Table 3. Relevant Parameters for Error Analysis

The "worst case" scenario for error is that all the errors are occurring in the same direction such that the error is maximized. This worst case error for C_D was calculated in equation 14, such that ΔN and ΔA are the possible errors in the normal force and axial force.

$$\Delta\ C_{Dworst} = |(\frac{\partial(C_D)}{\partial(N)})\Delta N| + |(\frac{\partial(C_D)}{\partial(A)}\Delta A| + |(\frac{\partial(C_D)}{\partial(V)}\Delta V| \tag{14}$$

A more realistic possible error for C_D is the geometric mean of the errors, and this is calculated in equation 17.

$$\Delta C_{Drealistic} = \sqrt{(\frac{\partial(C_D)}{\partial(N)}\Delta N)^2 + (\frac{\partial(C_D)}{\partial(A)}\Delta A)^2 + (\frac{\partial(C_D)}{\partial(V)}\Delta V)^2} \tag{15}$$

For the AFIT #3 balance, the uncertainty specified by the manufacturer are $\Delta\ N$=0.02lbs, which is 0.4% of the max normal load of 50lb, and $\Delta\ A$=0.0725lbs, which is 0.29% of the max axial load of 25lbs. The velocity error $\Delta\ V$ was calculated from the pressure in the tunnel.

$$\Delta V = \sqrt{(\frac{\partial(V)}{\partial(\rho)}\Delta\rho)^2 + (\frac{\partial(V)}{\partial(P_o - P)}\Delta(P_o - P))^2} \tag{16}$$

Such that

$$\Delta\rho = \sqrt{(\frac{\partial(\rho)}{\partial(T)}\Delta T)^2 + (\frac{\partial(\rho)}{\partial(P_{barometric})}\Delta P_{barometric})^2} \tag{17}$$

The final range of lift-to-drag ratio was then determined as:

$$C_{Drange} = C_D \pm \Delta\ C_D \tag{18}$$

The uncertainties for C_L were calculated similarly and displayed below.

	At $C_\mu = 12.22\%$			
Angle of Attack α	$\mathbf{C}_{Lworst}$	$\mathbf{C}_{Dworst}$	$\mathbf{C}_{Lrealistic}$	$\mathbf{C}_{Drealistic}$
-7°	0.0103	0.0153	0.0069	0.0114
33°	0.0249	0.0210	0.0178	0.0138

Table 4. Uncertainty at upper and lower α

IV. Results and Analysis

4.1 Preliminary Study: Cardstock Fence Location

The primary purpose of the preliminary fence location study was to determine where the 3D printed boundary-layer fence and slot would be located. The first portion of the study involved determining the best fence location among z/b = 50%, 60%, 70%, and 80%. For optimal use of time and research funds, stiff cardstock was used to construct temporary fences for the preliminary studies. These temporary fences were then taped onto the 3D printed baseline model and run through the standard profile of -7° to 33° to find the best location of those tested where the performance enhancement of the BLF is the largest without the addition of any negative performance characteristics. The primary interest was in the approximate location for maximum effectiveness for a BLF. This was not a full optimization study of location; instead, the purpose was to find the approximate best location of the given options to maximize performance gains for the main study. The BLF design parameters such as fence height amd length were not varied at all. Based on the studies outlined in the literature review, it was decided that the optimal fence heights would be 60% of the maximum thickness at the spanwise location, and that the fence would span the entire suction surface and wrap around the leading edge to 0.25x/c of the underside of the wing.

4.1.1 Lift Performance

Maximum lift coefficient (C_{Lmax}) is a common way to assess the performance limitations of a wing. Before any flow control devices were added, the maximum lift coefficient of the baseline model at 45 mph was determined to be 0.805, occurring at $\alpha = 21.37°$, as shown in Figure 28. Swept delta wings have a much more gradual

stall than unswept rectangular wings, so the baseline model does not fully stall until 23.5°, where there is a continual decrease in the coefficient of lift.

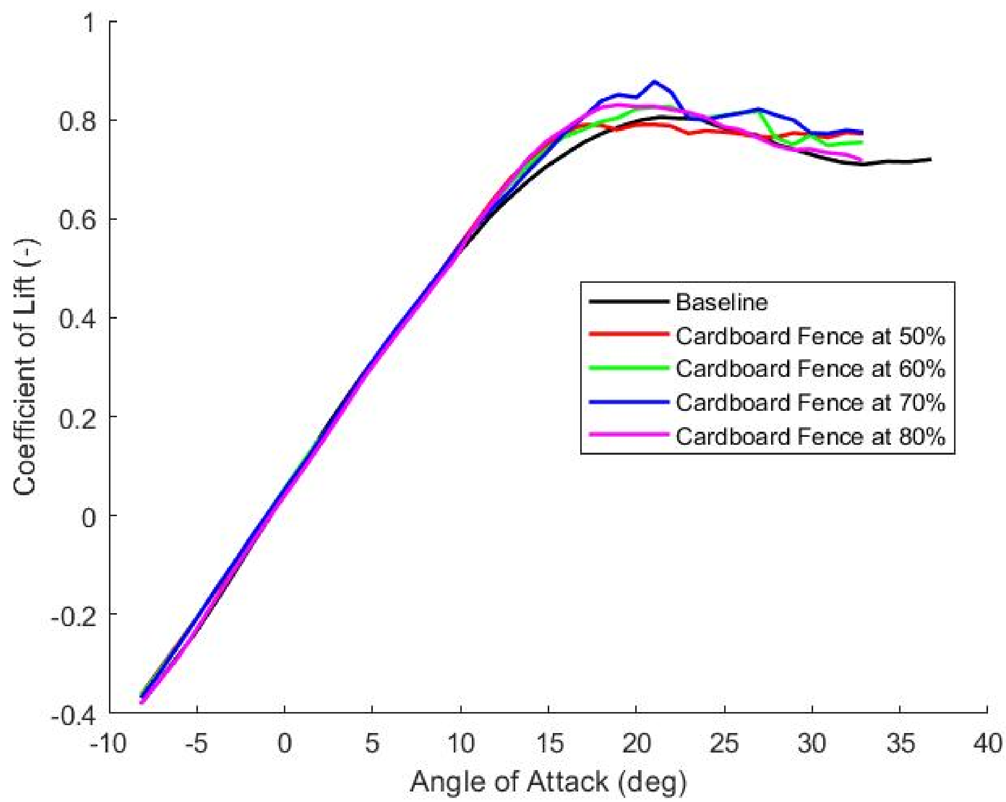

Figure 28. Coefficient of Lift, Temporary Fences, 45 mph

Figure 29 presents a close-up view of the data given in Figure 28 in the stall region. With the addition of a wing fence at 50% span, the initial peak of the lift coefficient was found to be 0.789, occurring at $\alpha = 17°$, which is a 2% reduction in maximum lift compared to the baseline. The addition of the fence at 50% span resulted in a large extension of the stall after C_{Lmax} is reached. Instead of a definite drop in C_L, there is a secondary increase at 21° that reaches the C_{Lmax} of 0.790, then a gradual decline, with smaller peaks occurring at 24°, 29° and 32°. The C_L drops by only 0.02 over the next 15°. This indicates that the fence is changing the flow characteristics such that the stall is less drastic, but the overall maximum lift produced is negatively

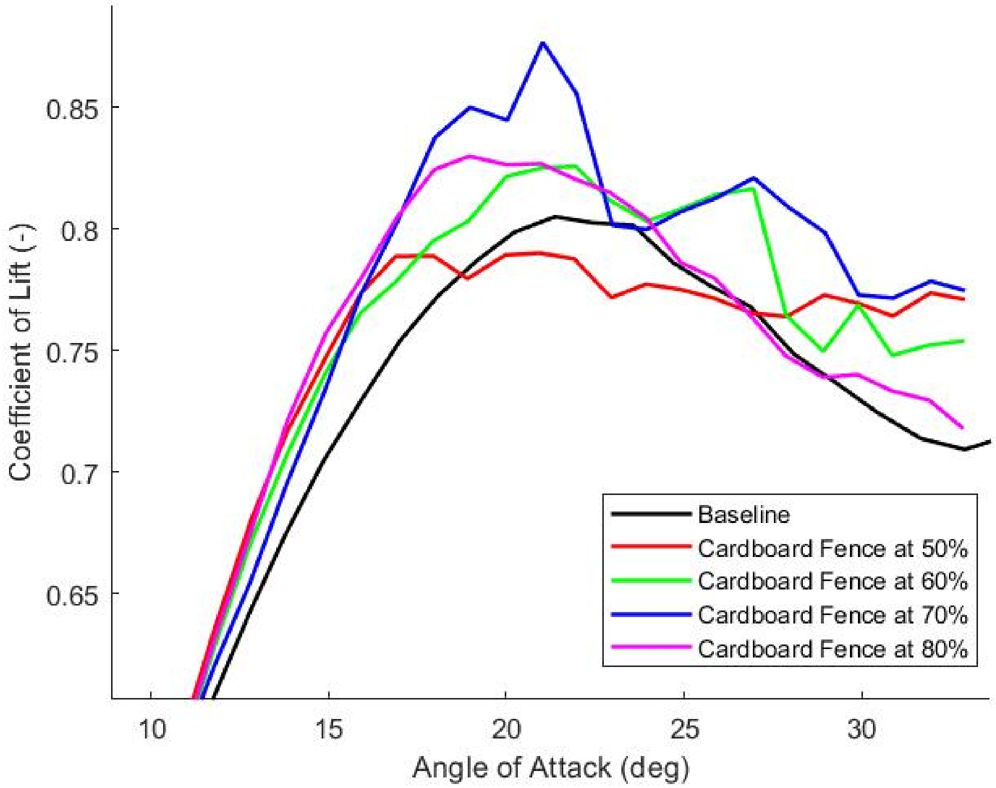

Figure 29. Coefficient of Lift at high α, Temporary Fences, 45 mph

impacted.

With the addition of a wing fence at 60% span, the maximum lift coefficient is 0.826, occurring at $\alpha = 22.2°$, a 2.5% improvement from the baseline. Like the previous fence, the addition of the fence at 60% span also resulted in delayed-stall characteristics. Like the 50% span fence, the 60% span fence sees a sharp drop off (at 22.2°) and a secondary increase at 27° that approaches a comparable C_L value to that of the C_{Lmax}. After this secondary peak, there is a definite drop in C_L (instead of the gradual decrease seen with the 50% span fence.) With respect to lift performance, the 60% span fence saw an improvement in C_{Lmax} and an additional secondary peak. This is a positive impact because it means the wing is producing lift until almost 27°, whereas the baseline wing stalled at 23.5°.

The 70% span fence location is shown to have the largest value for C_{Lmax}. With the addition of a wing fence at 70% span, the maximum lift coefficient is 0.877, occurring at $\alpha = 21.02°$, an 8.9% improvement in lift performance from the baseline. The 70% fence had the same delayed-stall characteristics, with the secondary peak occurring around 26.5°. The size and location of the 70% span secondary peak is very similar to the 60% span secondary peak size, with the only significant difference being a slight increase in the drop-off angle of attack, meaning the aircraft is continuing to produce lift until around 28°.

With the addition of a wing fence at 80% span, the maximum lift coefficient is 0.830, occurring at $\alpha = 18.95°$, a 3.1% improvement in maximum lift performance from the baseline. The 80% span fence does not have the secondary peak and possesses the same delayed-stall characteristics as the baseline. The 80% span fence was shown to have a 3% higher C_{Lmax}, but actually stalls earlier than the baseline.

To support the existence of the secondary peak, the baseline and the fence locations at 70% span and 80% span were repeated at 60mph, which increased the Reynolds number to Re = 6.62 x 10^5. Figure 30 shows that the trend of the C_L - α plot is the same for the different velocities, indicating that the secondary peak is an actual result of the boundary-layer fence, as opposed to a setup anomaly.

4.1.2 Pitch Moment Performance

Pitch moment is used to assess the impact of the boundary-layer fences on the longitudinal static stability of the aircraft. Typically, a BLF is applied to a wing with hopes of improving lift performance, improving pitch moment characteristics, or both. By looking a t the experimental results for the baseline model, this wing shows no apparent need for pitch moment characteristic improvements. For this reason, the focus of this investigation will largely be on improving lift performance without

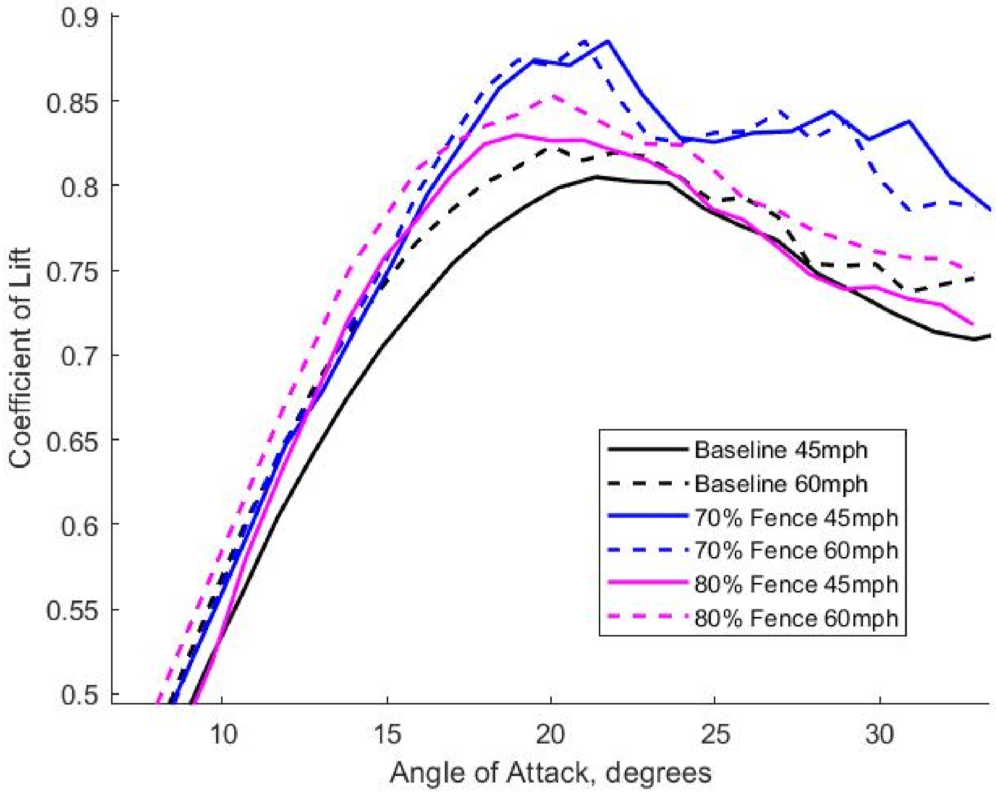

Figure 30. Coefficient of Lift at high α, Temporary Fences, 45 mph and 60 mph

degrading pitch moment characteristics.

Figure 31 shows the pitch moment coefficient (C_M) vs. angle of attack. The trend of the baseline data is that C_M is approximately zero at low angles of attack, with a slight negative $C_{M\alpha}$ slope value until 5°. From 5° to 16°, there is a positive slope, with the highest C_M value occurring at 16°, then there is a significant drop off of the C_M curve.

The addition of the cardboard fences cause an more negative initial C_M value, with the further inboard fences having greater negative values. There is a slight positive $C_{M\alpha}$ slope for all fence configurations. For the 70% and 80% fence locations, the pitch drop occurs earlier and is more gradual than the baseline configuration. For the 50% and 60% fence locations, there is an additional increase in C_{Malpha} at 14°

before the pitch drop. The pitch drop has a much steeper slope than the baseline configuration.

Physically, when a wing approaches stall, the center of pressure moves forward, causing an upward pitch moment, or a positive $C_{M\alpha}$. This can be seen in the increase in C_M before stall occurs. After stall, there is a sharp pitch down moment, seen in the drop in the graph. The positive $C_{M\alpha}$ slope shows unstable longitudinal static stability characteristics, while negative $C_{M\alpha}$ values show restorative stability.

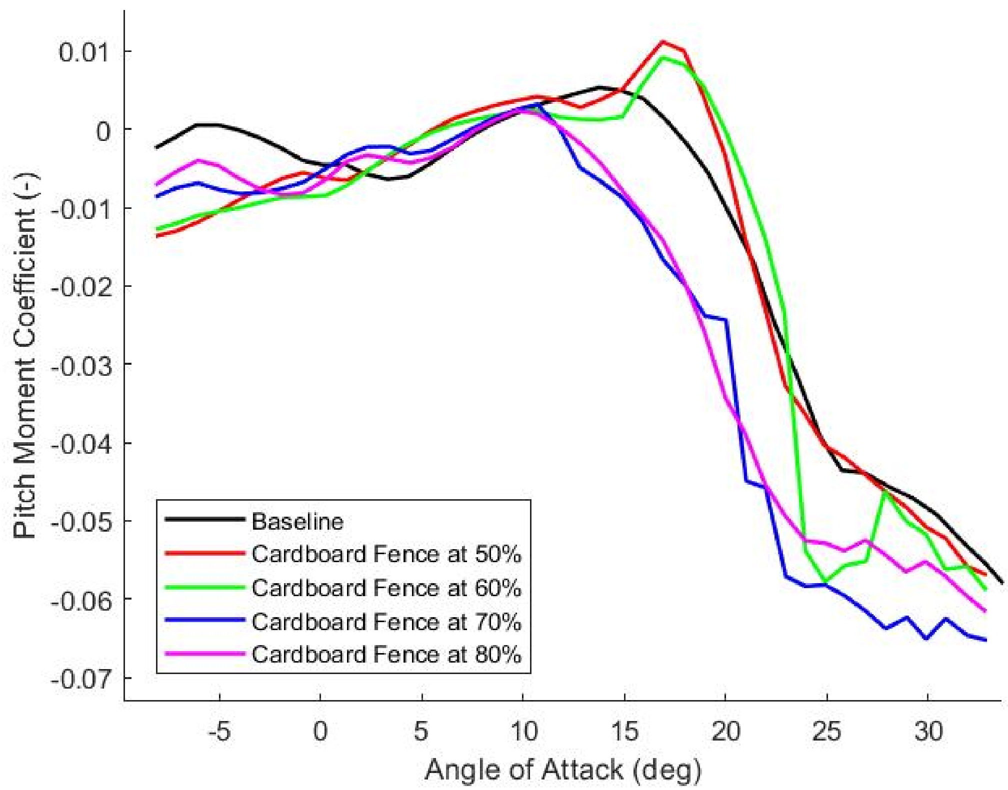

Figure 31. Pitch Moment Coefficient, Temporary Fences, 45 mph

4.1.3 Drag Performance

The drag performance is less of a consideration when assessing wing fence attributes than lift or pitch moment. Drag is a major consideration in foregoing passive

BLFs because the majority of flight is spent in cruise, where endurance is important. Passive flow control methods are always engaged, and thus are always providing drag even when the flow control is not providing any benefit. Because AFC allows the user to turn off the AFC device when it is not needed, the drag impact of the device becomes less of a consideration. In instances where the AFC is needed, like takeoff/-landing and high angle of attack maneuvering, generating additional lift is worth the drag penalty. For completeness, the drag performance will still be discussed.

As seen in Figure 32, the general trend of the data is the same for all configurations, with the minimum drag location occurring around 0°, and an increase as drag gets more positive or more negative.

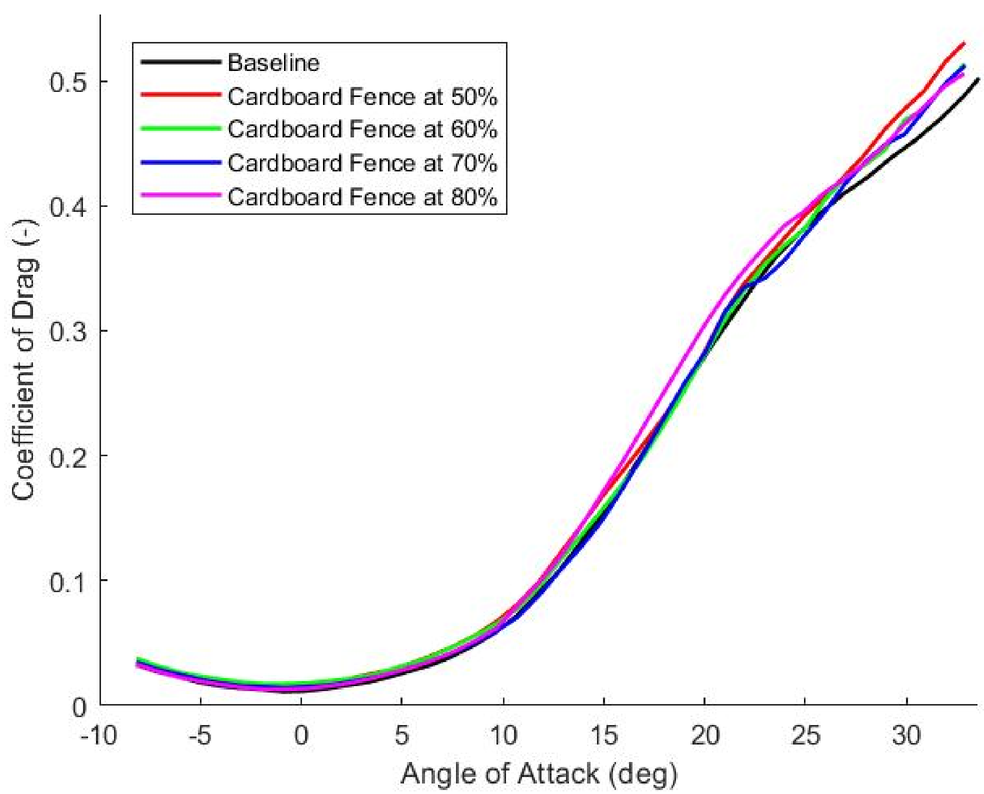

Figure 32. Coefficient of Drag, Temporary Fences, 45 mph

The primary takeaway from the drag data of the preliminary fence study was one

of confidence in the data. The trend between the cardstock models was that the baseline model had the lowest drag, followed in descending order from 80% span to 50% span. Recall that the height of the fence was $0.6t_{max}$, so the 80% fence was physically shorter and smaller than the 50% fence. With this in mind, it makes sense that the the smallest fence had the lowest drag. This trend is more obvious at lower angles of attack (Fig 33). Because axial force (and by extension, drag force) is difficult to measure accurately, the logical progression of the C_D fence trend was an encouraging sign.

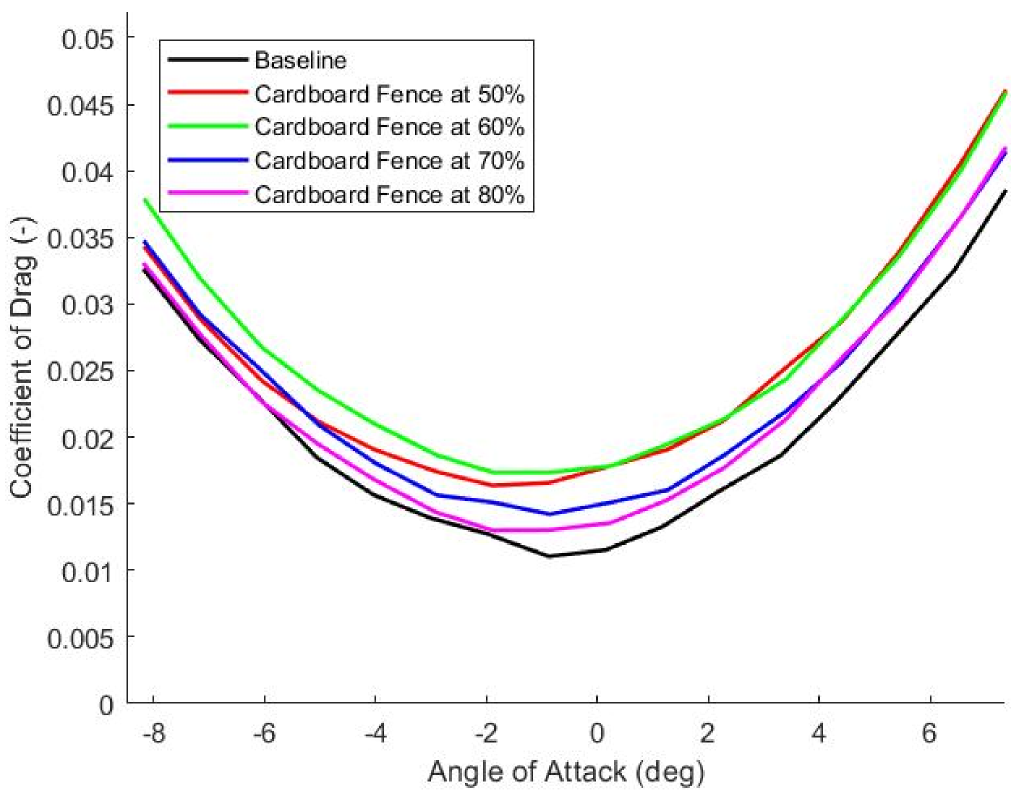

Figure 33. Coefficient of Lift at low α, Temporary Fences, 45 mph

Because the 70% span fence location saw the highest gains in maximum lift coefficient, a delay in α_{stall}, and no sharp destabilizing pitch moment characteristics, this configuration was chosen. Walker also used a 70% span fence location, providing

some independent corroboration of the results of this preliminary study. At this point in the study, the fence and slot model were 3D printed and prepared for testing.

4.2 Main Study: Active Flow Control vs. Passive Boundary-Layer Fence

Sections 4.2.1, 4.2.2, and 4.2.3 address the performance and flow visualization of the three main configurations. Section 4.3 provides some additional analysis of how the experiment setup, specifically the slot forces, influences the performance trends of the three main configurations.

4.2.1 Lift Performance Comparison

The primary indicator of performance improvement for this investigation is the change in coefficient of lift, with particular interest in the C_{Lmax} value. As stated in Section 4.1.1, the maximum lift coefficient of the baseline model at 45 mph was determined to be 0.805, occurring at $\alpha = 21.37°$ (Fig. 34). Note that any reference to a "fence" or "boundary-layer fence" past this point refers to the permanent fence model, unless explicitly referencing the temporary fences. With the addition of the passive boundary-layer fence at 70% span, the maximum lift coefficient is 0.875, occurring at $\alpha = 21.55°$, an 8.7% lift improvement from the baseline and no delay in stall. It is also notable that this is the same C_{Lmax} value (within 0.3%) that the cardstock fence model was tested at. This gives some additional confidence in the trends seen in the preliminary study, even through the cardstock fences were not as stiff and aerodynamically clean as the 3D printed material.

The 3D printed fence model did not experience the secondary peak that was observed with the temporary fences in the preliminary study. The addition of this fence gave a 8.7% increase in the C_{Lmax}, with minimal change in the stall angle.

The slot model was run at 200, 400, 600, 800, and 1000 standard liters per minute

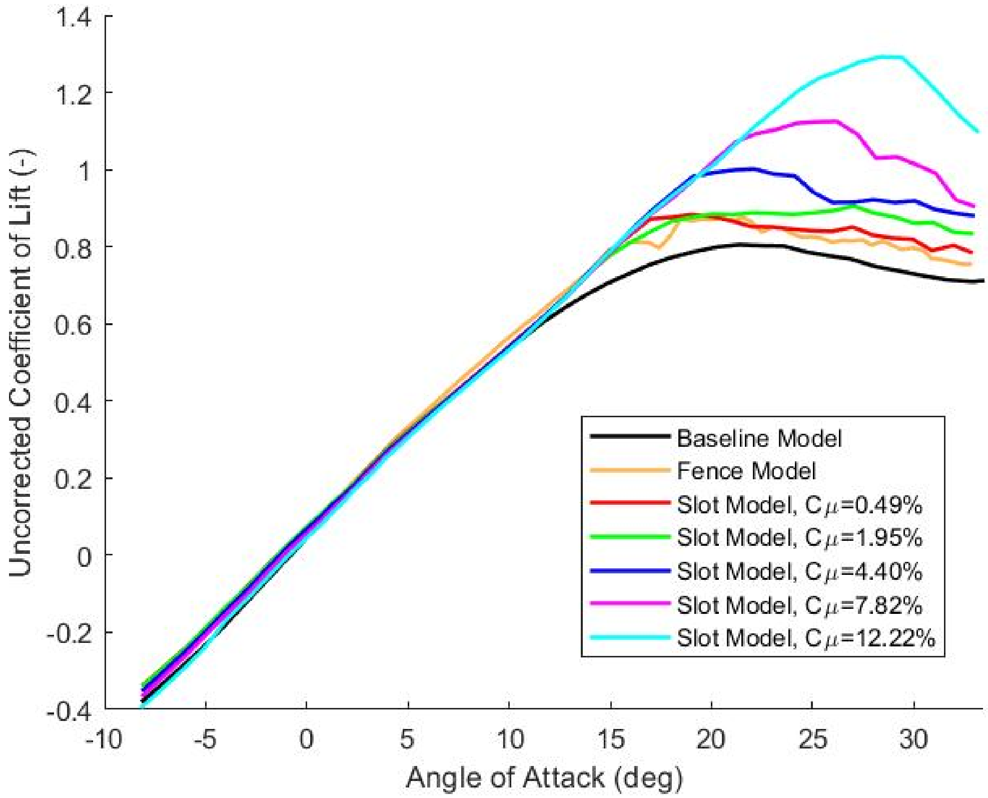

Figure 34. Uncorrected Coefficient of Lift, All Configurations, 45 mph

(SLPM), which is equivalent to a C_μ = 0.49%, 1.95%, 4.40%, 7.82%, and 12.22%, respectively. As the volumetric flow rate increased, the C_{Lmax} increased and stall was delayed.

For the slot model operating at $C_\mu = 0.49\%$ (200 SLPM), C_{Lmax} was 0.883, occurring at 19.0°. This is a 9.7% increase in the C_{Lmax} as compared to the baseline model. The stall is not sudden, which is not unusual for a delta wing. Even continuing 15° after C_{Lmax} , the model only drops to a C_L of 0.099. This configuration did stall at an angle of attack that was 2.4° lower than the baseline model. The slot model operating at $C_\mu = 1.95\%$ (400 SLPM) shows similar characteristics, where C_{Lmax} = 0.905 occurred at 27.0°. This is a 12.4% increase in the C_{Lmax} as compared to the baseline model. Again, the stall is extended and not very drastic, only dropping to

Configuration	Flow rate (SLPM)	$C\mu$	C_{Lmax}	α_{CLmax}	Percentage ΔC_{Lmax}
Baseline	-	-	0.805	21.4°	-
BLF	-	-	0.875	22.6°	8.7
Slot Model	200	0.49%	0.883	19.0°	9.7
	400	1.95%	0.905	27.0°	12.4
	600	4.40%	1.001	22.1°	24.4
	800	7.82%	1.125	26.2°	39.6
	1000	12.22%	1.290	29.4°	60.3

Table 5. Uncorrected Coefficient of Lift at 45 mph, All Configurations

a C_L of 0.071 at 33°. This configuration stalled significantly later than the baseline model. The slot model operating at C_μ = 4.40% (600 SLPM) shows similar characteristics, where C_{Lmax} = 1.001 occurred at 22.1°. This is a 24.4% increase in the C_{Lmax} as compared to the baseline model. This configuration stalled slightly later than the baseline model. There was a minor secondary peak occurring at 28°. The slot model operating at C_μ = 7.82% (800 SLPM) shows similar characteristics, where C_{Lmax} = 1.125 occurred at 26.2°. This is a 39.6% increase in the C_{Lmax} as compared to the baseline model. This configuration stalled later than baseline model. There was a minor secondary peak occurring at 29°. The slot model operating at C_μ = 12.22% (1000 SLPM) has no secondary peak and displays a sharp drop off that is more reminiscent of that of a straight wing. C_{Lmax} was 1.290, occurring at 29.4°. This increase represents a 60.3% increase in the C_{Lmax} as compared to the baseline model, and a significant delay in the stall angle of attack.

4.2.2 Pitch Moment Characteristics Comparison

Figure 35 shows the pitch moment coefficient for the baseline model, the permanent boundary-layer fence, and the slot model at all flow rates.

As outlined in Section 4.1.2, the overall trend of the baseline data is that C_M is approximately zero at low angles of attack, and has a increase in C_M, then gradual

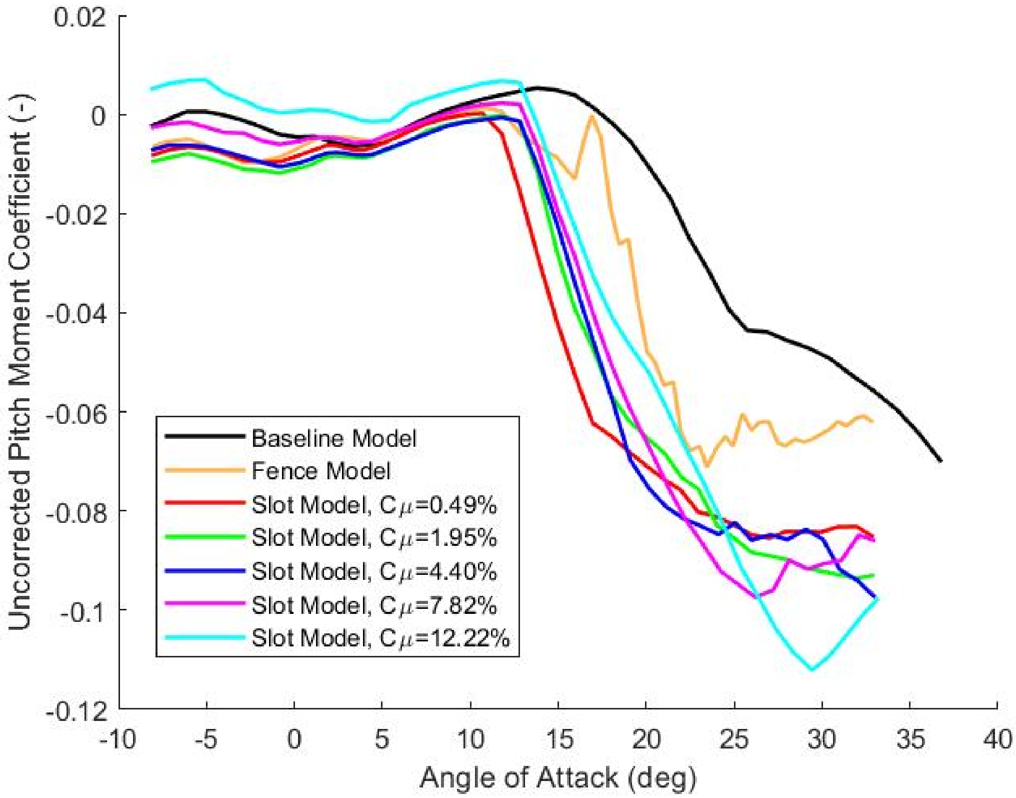

Figure 35. Uncorrected Pitch Moment Coefficient, All Configurations, 45 mph

drop of the C_M curve.

The passive boundary-layer fence model starts at a slightly lower C_M (-0.00645), but follows the same trend until around 10° angle of attack. At larger angles, there is a dip in C_M, indicating a brief pitch down. There is a sharp increase in C_M at 16°, then a steep drop at 17°. This decrease in C_M continues until 22°, with another brief C_M peak at 25°. The fence model has more of a jagged path compared to the baseline model, which is particularly apparent at high angles of attack. This jagged profile was seen with repeated trials of the fence model.

The general trend of the slot data is that the initial C_M value increases as flow rate increases. The $C_\mu = 0.49\%$ configuration begins with an initial C_M value of -0.00835, and $C_\mu = 12.22\%$ configuration having a positive initial value of 0.00507 (see Section

4.3 for explanation of the changing initial values). Regardless of flow rate, all the slot configurations experience a sharp drop in C_M (or pitch down moment) from between 10° to 13°. The point of the C_M drop varies depending on the configuration, dropping earlier for the lower flow rates.

This drop off continues until around 25°. The highest two blowing configurations of $C_\mu = 7.82\%$ and 12.22% have an increase in Δ C_M of 0.0111 and 0.0146 respectively. The angles of attack where the pitch up occurs are the same angles of attack where the C_{Lmax} occurs; 26.2° for $C_\mu = 7.82\%$ and 29.4° for $C_\mu = 12.22\%$. This slight pitch up is a destabilizing tendency during stall.

Pitch moment plots are valuable because they provide an indication of how lift distribution changes with angle of attack. A negative C_M indicates a pitch down motion, which in turn can be interpreted as:

1. a decrease in lift at the front half of the wing
2. an increase in lift at the back half of the wing
3. some combination of (1) and (2)

These changes could also be expressed by a change in the center of pressure. Figure 36 shows the florescent tuft flow visualization in the middle of the C_M drop. The straight undisturbed tufts outboard of the slot indicates that the flow is still attached in these locations, which has also been demonstrated in other studies [5]. This region of attached flow is a region of lift located behind the aerodynamic center, which would create the pitch down moment seen graphically.

4.2.3 Drag Performance Comparison

Though drag reduction is not the goal of flow control, it is a consideration in any thorough aerodynamic investigation. Figure 37 shows the drag coefficient of

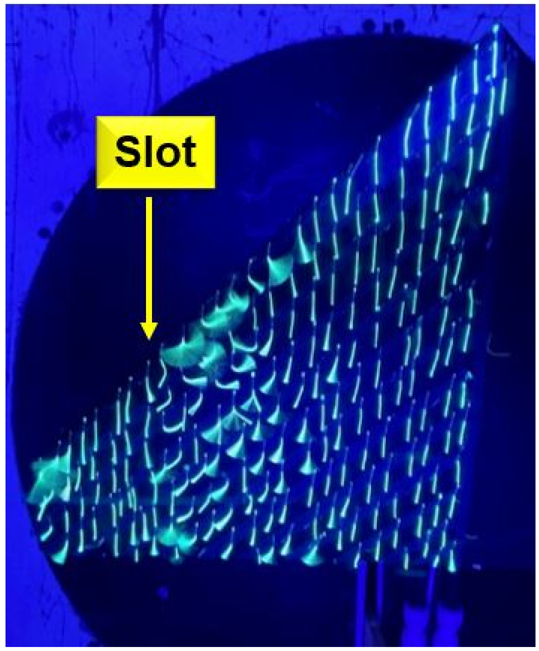

Figure 36. Slot Model Tuft Flow, C_μ = 7.82% at 15°

the different configurations. The baseline model and the fence model are statistically identical until 18°, at which point the fence model briefly has a C_D that is (on average) 5% larger for the higher angles of attack.

The slot model exhibits significantly lower drag than the baseline and fence model, with the higher flow rate corresponding to the lowest C_D values (see Section 4.3 for explanation). From -7° to 12°, the general trend of the data is the same. The highest slot momentum of C_μ=12.22% has a smooth curve with no inflection points until around 30.4°, where the slope decreases.

The C_μ=7.82% curve follows the trend of C_μ=12.22% until 21.2°, where there is an inflection point where the drag curve increases. Around 27°, the slope of the C_μ=7.82% curve returns to that of the lower momentum curves, which is slightly greater than the baseline at high angles of attack. The C_μ=4.40% curve also follows the trend of C_μ=12.22%, with a drag increase at 18.8°. Around 21°, the slope of the C_μ=4.40% curve returns to that of the lower momentum curves. The C_μ=1.95%

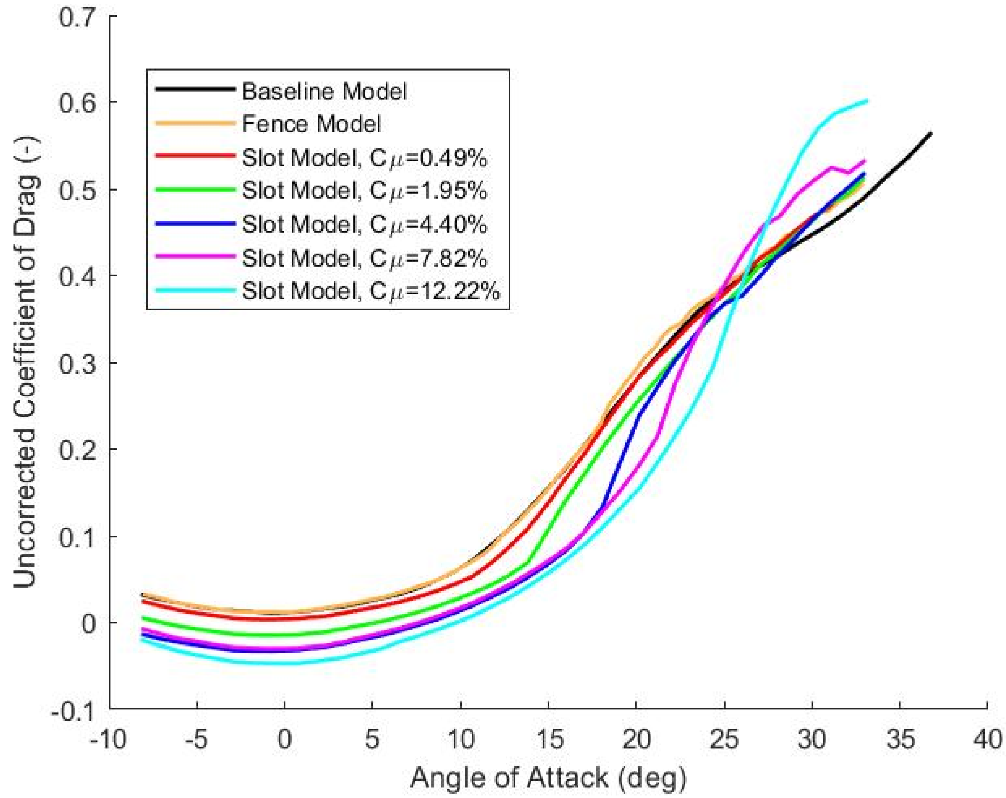

Figure 37. Uncorrected Coefficient of Drag, All Configurations, 45 mph

curve experiences an inflection point in the drag slope around 13.8°. The C_μ=0.49% curve experiences a minor inflection point in the drag slope around 10.69°.

4.3 Slot Forces and Moments

When pressurized air is flowing into the back of the model and out of the slot, this slot air applies resultant forces and moments to the sting that are independent of the typical forces measured when the wind tunnel is on.

Figure 38 illustrates the predicted blowing pattern of the model. One observation from the experiment was the flow out of the leading edge of the slot was minimal compared to the upper and lower sections of slot. Based on this, and Walker et al.'s velocity profile (Fig. 55b), it was assumed that the mass flow out the front of the

model was lower than the rest of the wing. The slot air (light blue arrows) exerts a net slot force (dark blue arrow), which then creates a resultant force acting on the model (dark red arrow). This resultant force can be expressed in terms of lift and drag (light red arrows), which can then be factored out of the total C_D, C_L, and C_M plots discussed in Section 4.2.

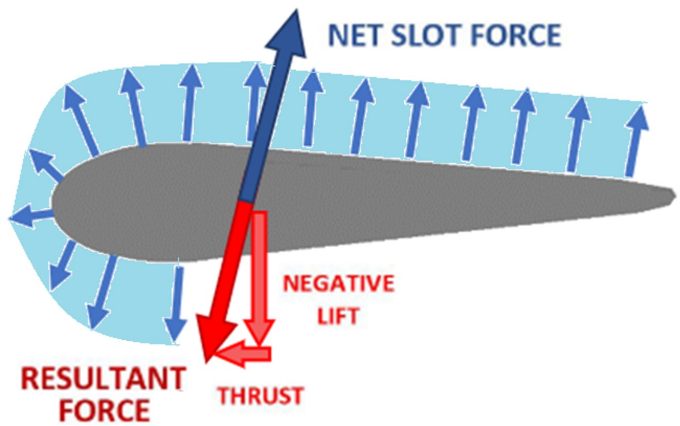

Figure 38. Expected Velocity Profile

This section deals with "bench-top" force and moment values, meaning they were taken when the wind tunnel was off, and no external aerodynamic forces were being applied. This is a useful technique that provides insight about the slot, but it is important to note that the slot forces and moments will change when when the wind tunnel is on. With freestream air flowing over the model, the surface pressure over the wing is different than the static case, which impacts the distribution of the air coming out of the slot. Additionally, as the model moves through different angles of attack, the pressure distribution also changes, which changes the flow distribution out of the slot. For example, when the tunnel is on, the low pressure region of the suction peak (as discussed in Section 2.1) provides a path of less resistance for the air in the internal chamber to flow out of the slot, so the slot flow will likely be higher near the front of airfoil compared to what a bench-top test would reflect.

The slot forces were measured by running the standard -7° to 33° sweep profile

with the tunnel off. These values were subtracted from the tare file for each model to eliminate the impact of the model weight and thus isolate the slot forces. As the model increases in angle of attack, the normal and axial forces on the model change. When the wind tunnel is off and there is no slot air, the net lift and drag should be zero, which would result in the coefficient of lift and drag also being zero. No airflow over the wing corresponds to no lift or drag. (Refer back to Equations 1 and 2 for the relationship between lift, drag, normal force, and axial force.)

The first step of the wind tunnel process was to null the weight of the sting and model. This weight must be factored back into the forces acting on the model in order to get correct force value trends. The force data was taken with the tunnel off (0 mph).

4.3.1 Impact of Slot Forces on Lift and Drag

Figure 39 outlines the resultant vector orientation based on the benchtop lift and drag values (wind tunnel off, slot air on). The location where the drag is maximized should correspond to the lift being zero. As drag decreases, lift increases. As angle of attack increases, Figure 39 illustrates how the changes in lift and drag (light red arrow) modify the resultant vector (dark red arrow) according to the angle of attack. The resultant force magnitude and direction does not change with respect to the model orientation. The resultant force is in the opposite direction of the net slot force (blue arrow).

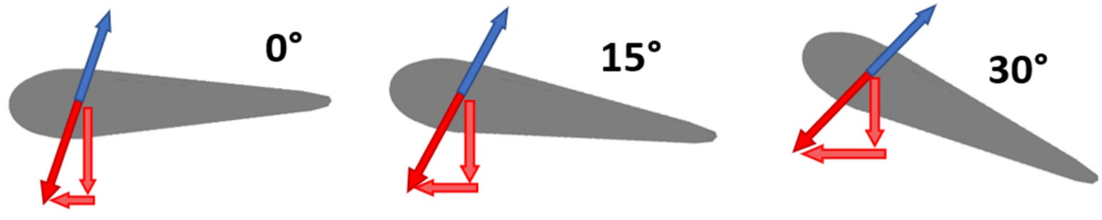

Figure 39. Lift and Drag Components

As angle of attack increases, the negative lift component decreases (so lift increases) and the thrust component increases (so drag decreases.) Eventually, the resultant vector will point completely forward, at which point, the magnitude of drag is maximized and lift is zero. After this point, lift will be positive and the thrust component will begin to decrease again.

When looking at the main C_D vs α plot, each of the slot models start at a negative C_D value, with the higher flow rates having a greater initial negative C_D value (Fig. 37). This is also reflected in the benchtop slot forces, which all have negative C_D values that are more negative as the slot flow rate increases. Figure 40 illustrates the drag force that is generated from the slot air. The measured lift and drag forces can be related to the lift and drag components shown in Figure 39. As expected, thrust (or negative drag) is generated because a component of the slot air flow is pushing back, providing a resultant force forward. As angle of attack increases, drag decreases (or thrust increases).

Figure 41 illustrates the lift force that is generated from the slot air. As expected, negative lift is generated because a component of the composite slot air flow is pointing up, providing a resultant force down. As angle of attack increases, negative lift decreases (Fig. 39).

A way to verify the force data is that the resultant vector of lift and drag should be constant at all angles of attack, with the resultant magnitude increasing as the C_μ increases. Figure 42 illustrates the magnitude of the resultant force vector calculated across all angles of attack. This was calculated using the Pythagorean Theorem in Equation 19. As the C_μ increases, the amount of variation in the resultant force increases.

$$F_{Resultant} = \sqrt{F_{Lift}^2 + F_{drag}^2} \tag{19}$$

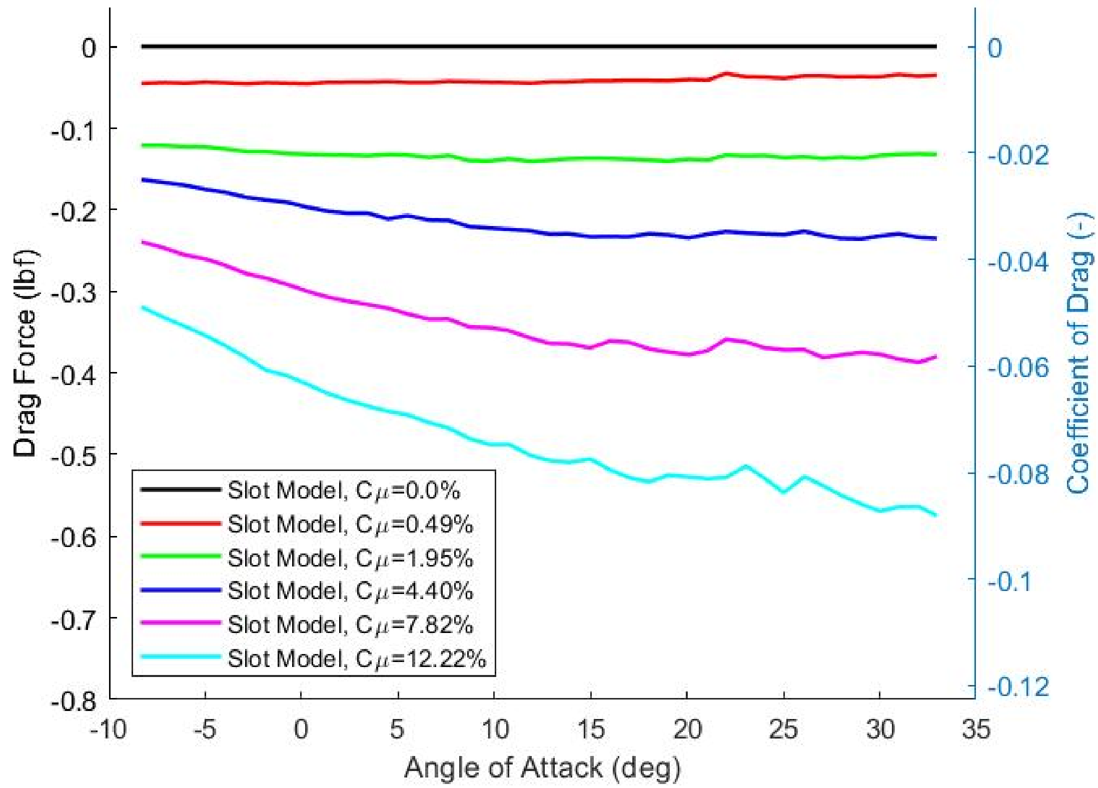

Figure 40. Benchtop Drag Forces, All Slot Configurations, 0mph

4.3.2 Impact of Slot Forces on Pitch Moment

When looking at the main C_M vs α plot, each of the slot models start at a negative C_M value, with the higher flow rates having a greater initial negative C_M value (Fig. 35). Assuming the resultant vector is not changing orientation with respect to the wing profile, the pitch moment should be constant with angle of attack. The benchtop slot forces all have positive C_M values, with increasing magnitude with increasing C_μ (Fig. 43.)

The applied force from the slot is constant with angle of attack, and the moment arm also does not change, so pitch moment should be constant across all angles of attack. By looking at the 0° case in Figure 39, one can see the orientation of the resultant vector with respect to the moment center of the sting, where the pitch

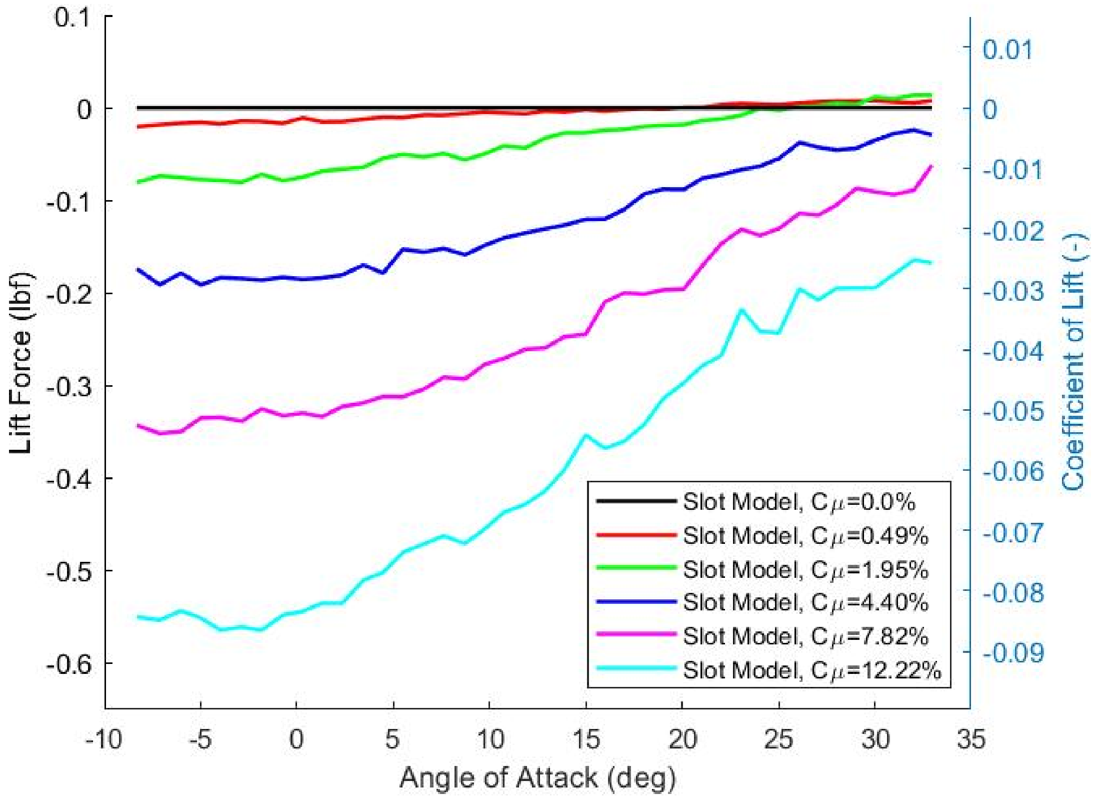

Figure 41. Benchtop Lift Forces, All Slot Configurations, 0mph

moment data was taken. Figure 44 shows the location of the sting moment center, but the exact location of where the resultant force vector is acting is unknown.

Because it is unlikely that the moment arm is changing, this decrease is likely to be caused by a change to the resultant vector. For the slope to increase, there would need to be an increase in strength of the resultant vector or a shift in the resultant vector downward.

As shown by the red line on the left of the Figure 44, the resultant force vector could potentially act anywhere along the length of the slot, depending on how air is directed out of the internal chamber. The sting moment center is located within this range. If the resultant force was located ahead of this point, the data shown would be a pitch-down moment that would be constant across all angles of attack, but would

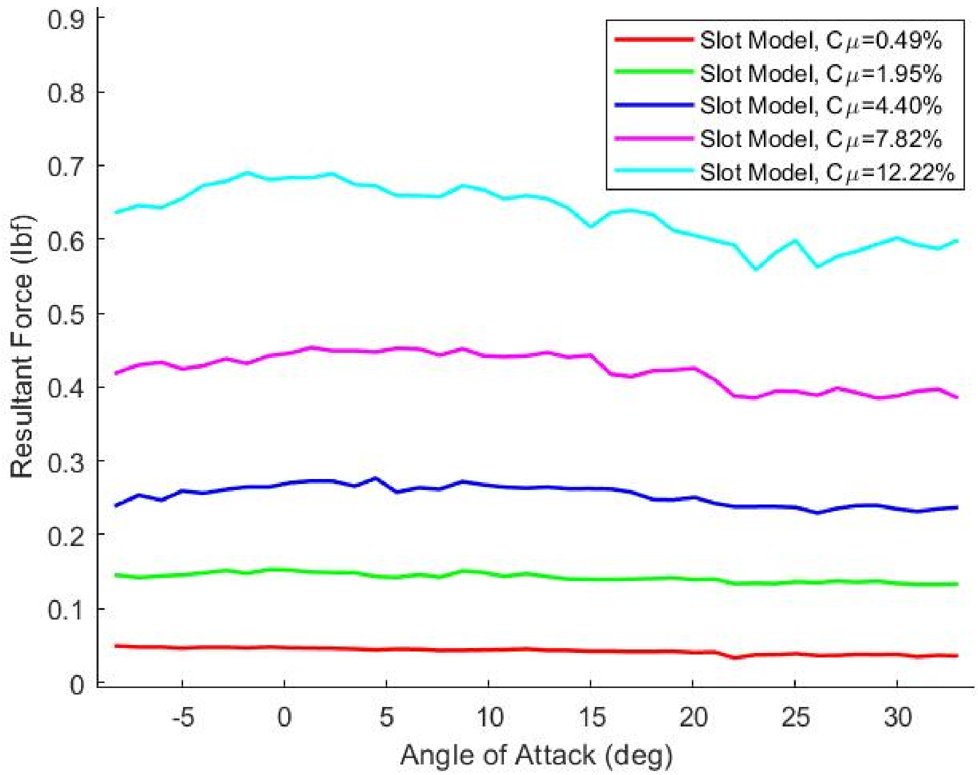

Figure 42. Resultant of Lift and Drag Slot Forces

increase in magnitude as the flow rate of the slot increased. If the resultant force was located behind this point, the data would show the same characteristics, but with a positive pitch up moment. The positive pitch moments seen in Figure 43 indicate that the resultant force occurs in the back half of slot location. This may be due to the inlet for air source being located in the back of the internal chamber.

4.4 Data Corrected for Slot Forces and Moments

The corrected lift, drag, and pitch moment performance corrections for the slot configurations are presented in Figures 45-47. These were acquired by subtracting the benchtop slot forces and moments (presented in Section 4.3) from the main data (presented in Section 4.2)

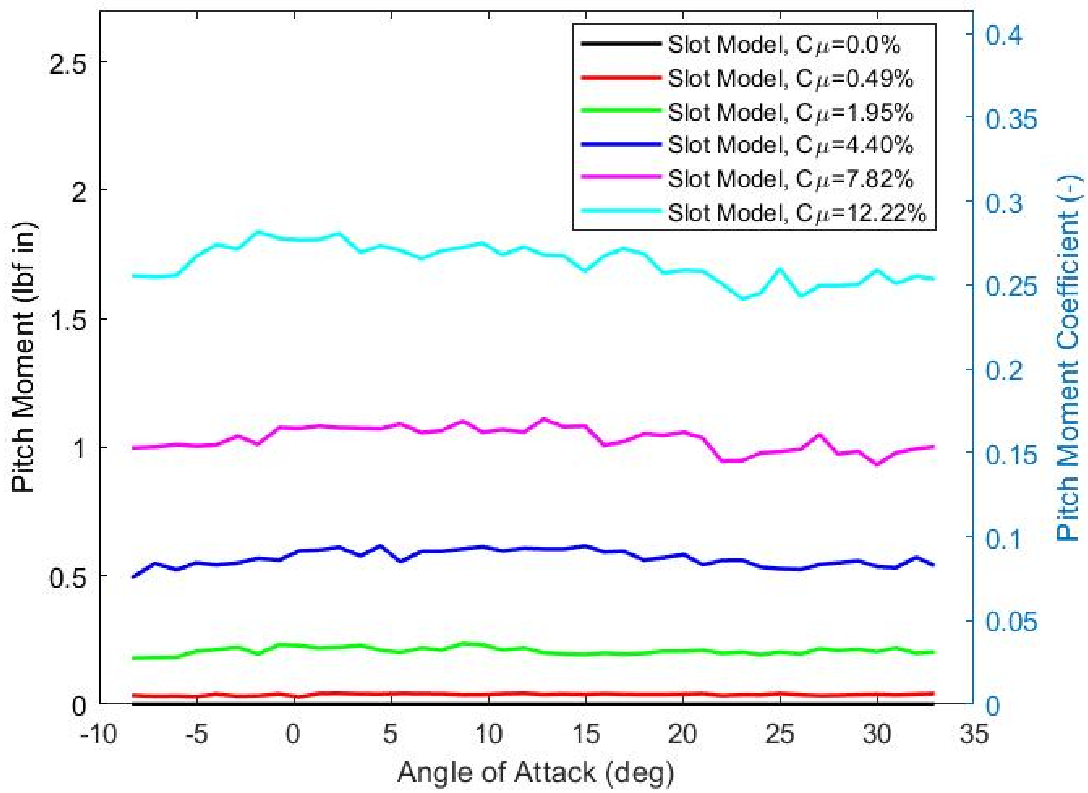

Figure 43. Benchtop Pitch Moment, All Slot Configurations, 0mph

With the corrections applied to the coefficient of lift in Figure 45, the general trend of the data is the same, but shifted up slightly. The shift is greater at low angles of attack based on Figure 41. The corrections indicate that, with the slot forces factored out, the AFC slot provides a lift increase across the entire range of angle of attack, whereas the uncorrected values only provided a notable lift improvement past 10°. The corrected C_{Lmax} values are shown in Table 6.

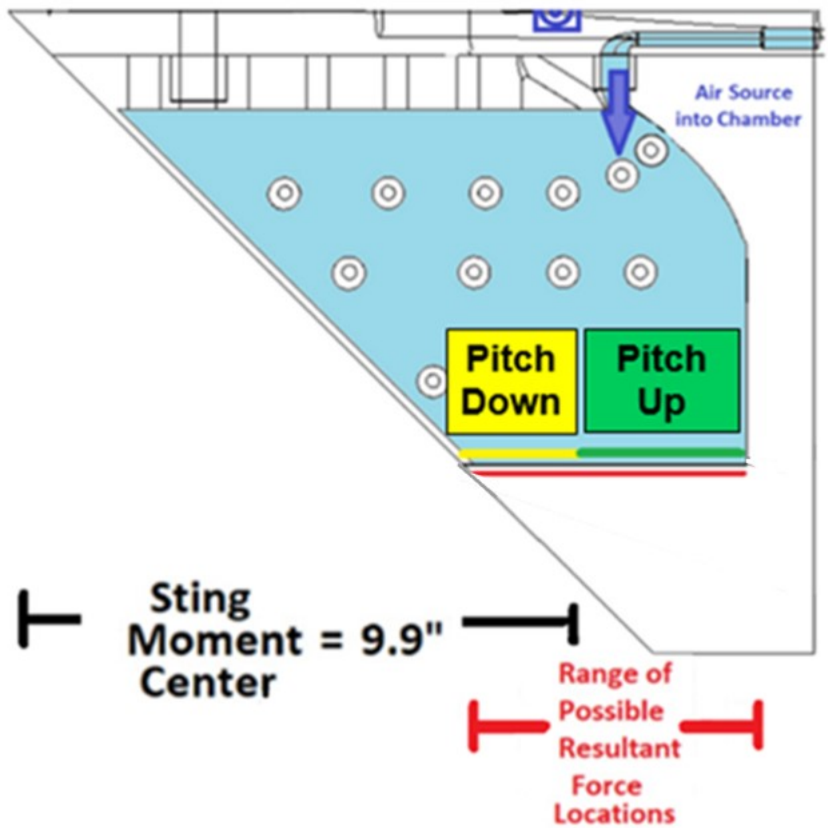

Figure 44. Internal Layout with Possible Resultant Locations

As previously stated, the benchtop slot force data will not directly correspond to the operational slot force data because of the changes in surface pressure over the wing when the wind tunnel is on. There is a coupling effect that cannot be isolated using benchtop force measurements. With the corrections applied to the coefficient of drag in Figure 46, the C_D lines also shifted up slightly, which partially corrects for the problem of negative C_D values. There should be an additional correction factor if the aerodynamic coupling could be accounted for. The plot shift is greater at as angle of attack increases, as seen in Figure 40. As a result, the slot configurations past 24° have higher drag values compared to the baseline and fence model.

With the corrections applied to the pitch moment coefficient of in Figure 47, the flat region of the plot (from -7° to 12°) has a clear shift down based on the slot momen-

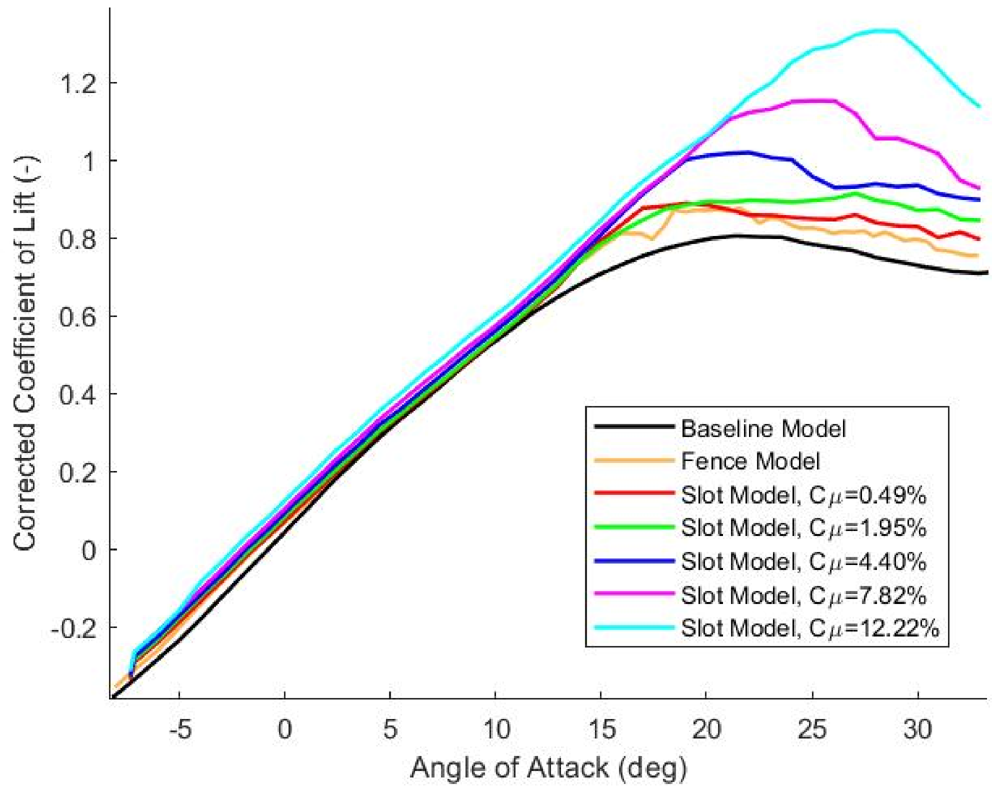

Figure 45. Corrected Coefficient of Lift, All Configurations, 45 mph

tum configuration. Higher momentum values had more negative initial C_M values. The slot force correction additional also caused the path of the pitch drop region (from 12° to 20°) to overlap more closely between the different slot configurations. (The uncorrected lines in this region were more spaced out.)

Configuration	Flow rate (SLPM)	$C\mu$	C_{Lmax}	α_{CLmax}	Percentage ΔC_{Lmax}
Baseline	-	-	0.805	21.4°	-
BLF	-	-	0.875	22.6°	8.7
Slot Model	200	0.49%	0.888	19.0°	10.3
	400	1.95%	0.914	27.0°	13.5
	600	4.40%	1.019	22.1°	26.6
	800	7.82%	1.151	26.2°	43.0
	1000	12.22%	1.330	29.0°	65.22

Table 6. Corrected Coefficient of Lift, 45 mph

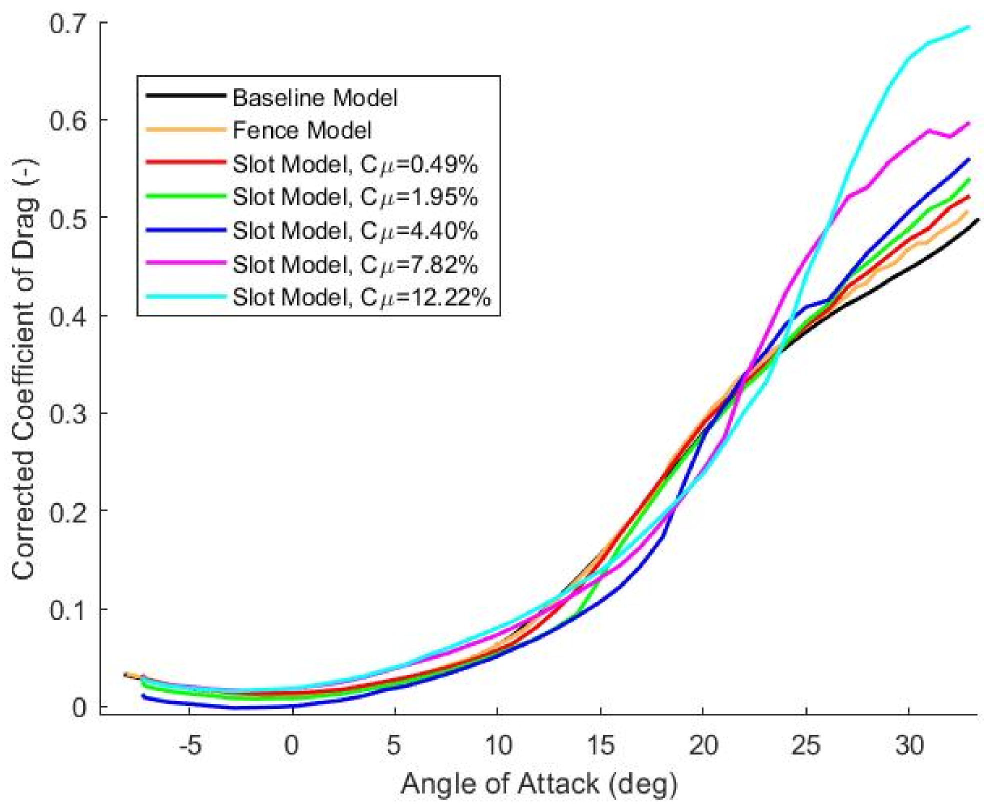

Figure 46. Corrected Coefficient of Drag, All Configurations, 45 mph

4.5 Surface Flow Visualization Results

All flow visualization photos are taken such that the freestream is coming from the top of the page down. Before diving into the flow visualization results, it is important to recap the benefits and limitations of fluorescent tuft flow visualization.

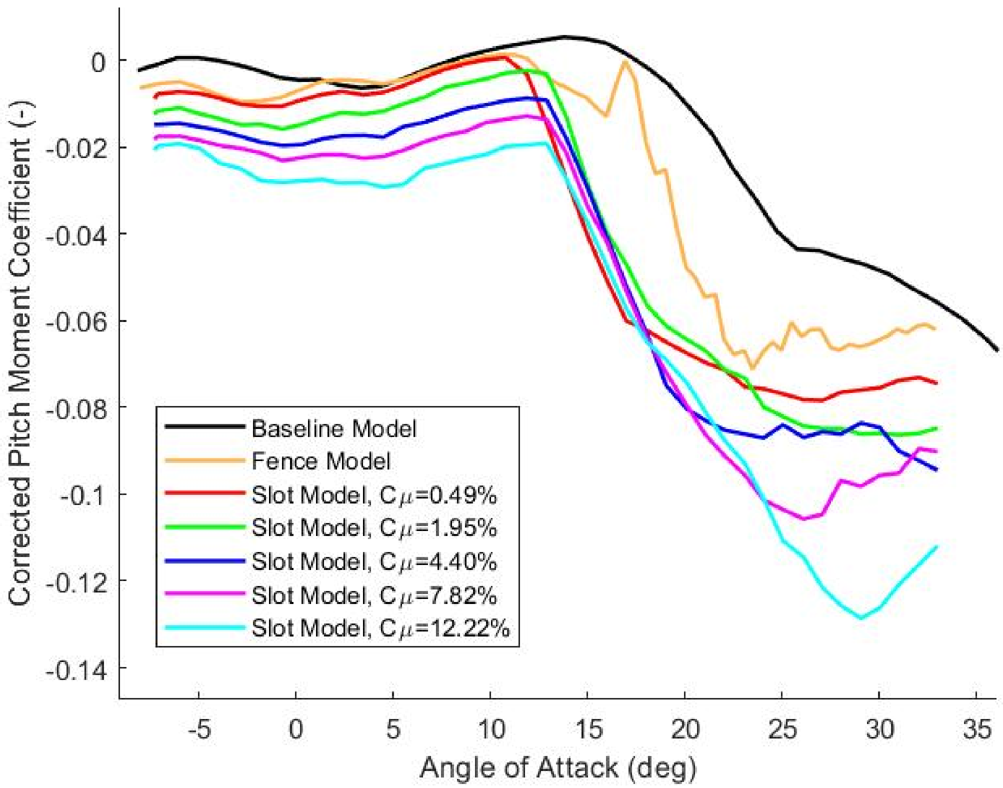

Figure 47. Corrected Pitch Moment Coefficient, All Configurations, 45 mph

This technique is valuable as a simple, low cost option that provides insight about the flow on the surface. The presence of surface tufts can also operate as a boundary-layer trip, facilitating an earlier transition from laminar to turbulent flow. Because the presence of tufts can cause differences in the flow field, care should be taken when making definitive statements about observed flow mechanisms.

Comparing the configurations at 15°, there is a clear indicator of attached flow outboard for both the fence model (Fig. 49b) and the slot model (Fig. 49c). The slot model appears to have a larger area of attached flow outboard of the wing, which may be contributing to the significant lift gains compared to the fence model. There also appears to be an increased region of separated flow inboard of the fence model and the slot model compared to the baseline model. Because the C_L plot indicates

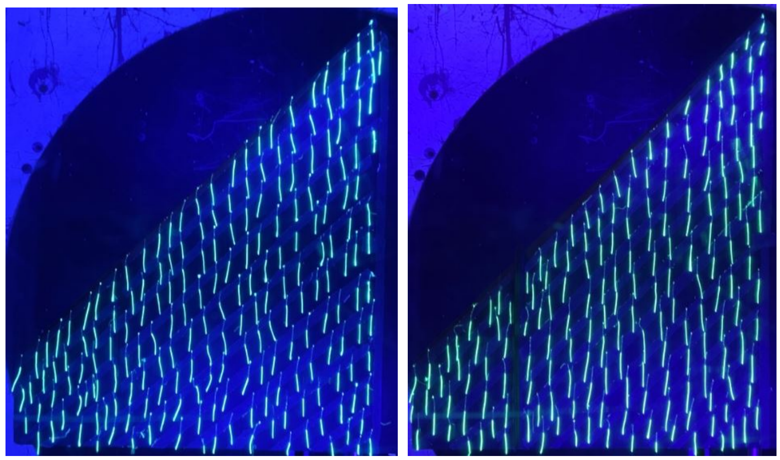

(a) Baseline Model (b) Fence Model

Figure 48. Fluorescent Tuft Visualization, 0°

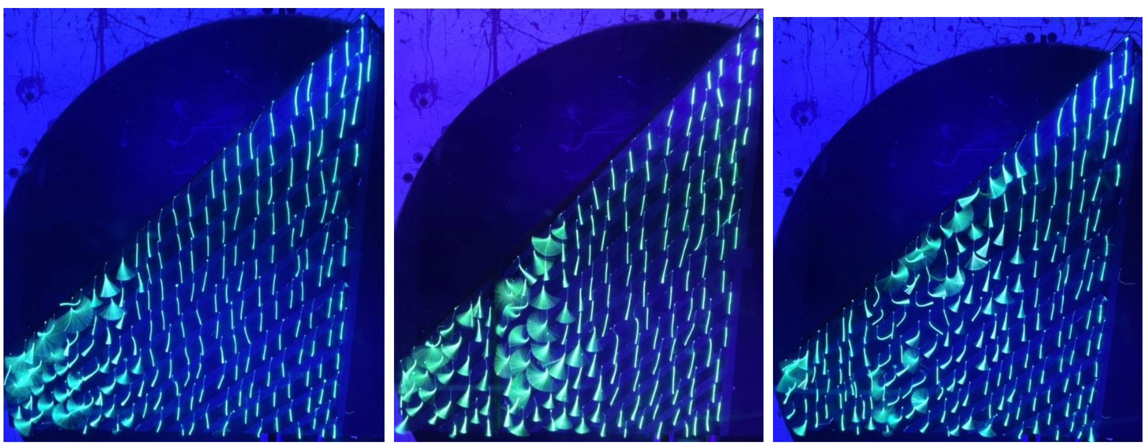

(a) Baseline Model (b) Fence Model (c) Slot Model, C_μ = 7.82%

Figure 49. Fluorescent Tuft Visualization, 15°

that a larger amount of lift is being generated at 15°, this shows that the region of attached flow more than compensates for the separated flow inboard.

At 25°, there is a indicator of attached flow outboard for the AFC slot model (Fig. 50c), while the BLF fence model appears to have separated (Fig. 50b). The slot model appears to have large region of attached flow outboard of the wing, and flow inboard of the fence directed toward the slot. This potentially indicates an entrainment effect where flow is being pulled into the slot. The fence model shows a much larger region

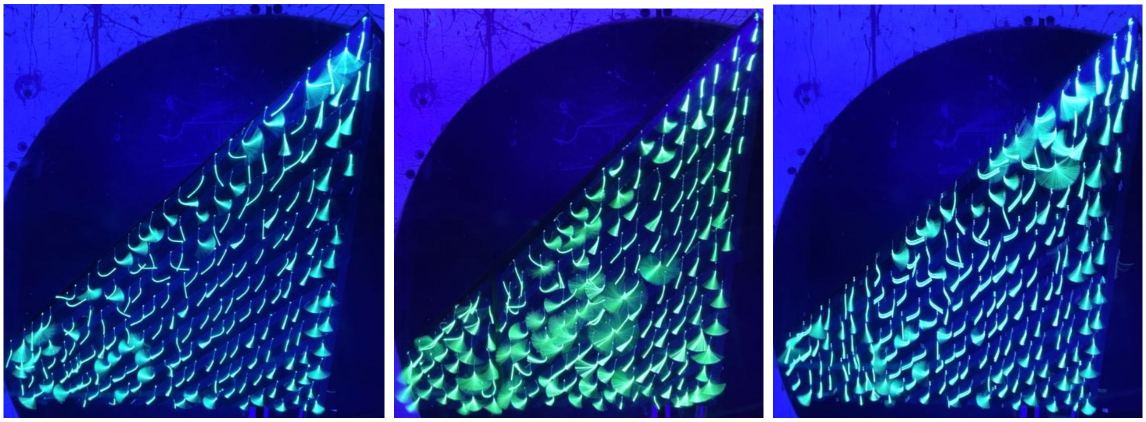

(a) Baseline Model (b) Fence Model (c) Slot Model, $C_\mu = 7.82\%$

Figure 50. Fluorescent Tuft Visualization, 25°

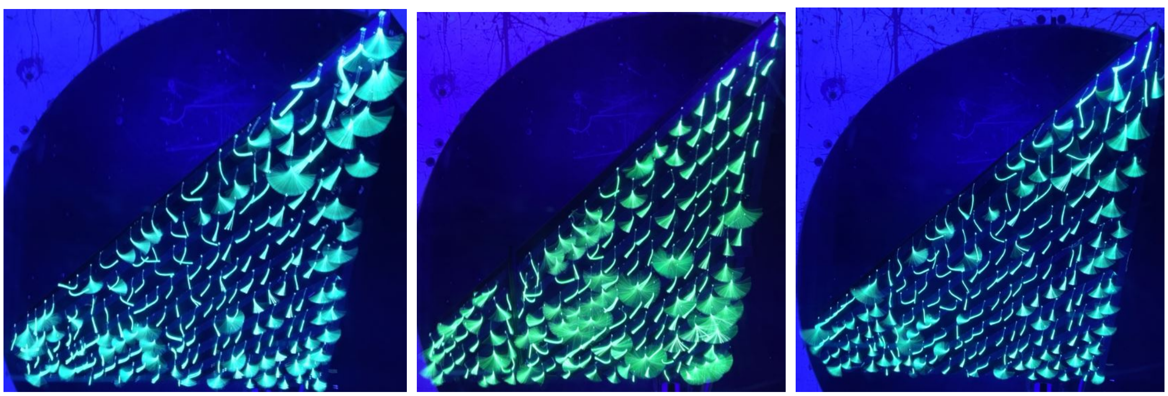

(a) Baseline Model (b) Fence Model (c) Slot Model, $C_\mu = 7.82\%$

Figure 51. Fluorescent Tuft Visualization, 33°

of separated flow inboard, even when compared to the baseline model.

Comparing the configurations at the maximum angle of attack tested, the fence model shows a lot of tuft movement, while the slot model seemed to show a wave of separated flow moving from the tip inward, then the tufts inboard of the fence showed minimal movement and remained pointed outboard of the fence. This may be an indicator of entrainment from the slot directing flow over the top of the wing back toward the slot, thus energizing the flow. However, the baseline model at 25° (Fig. 50a) shows the tufts pointing inward, so this observation may also be an indicator of spanwise flow, or just a by-product of how the tufts were affixed to the board. Future

work where the tufts are glued to the model will shed some light on this question.

4.6 Comparison with Previous Studies

This investigation had comparable lift gains to previous investigations when looking at the passive BLF, but there were significant lift gains for the AFC slot when compared to Walker et al.'s [10] AFC slot on the swept rectangular wing.

Salmi [1] and Pratt [2] both performed research on an NACA 63_1-A012 tapered swept rectangular wing in the 1950s to investigate the impact of boundary-layer fences. They both looked at the impact of fence location, fence thickness, and multiple fences, with Salmi also adding twist and camber (which resulted in higher C_{Lmax} values.) They found the use of boundary-layer fences provided an increase in C_{Lmax} between 4% and 6% compared to the baseline with the fence location at 0.575 z/b. Both found that the 0.575 z/b location was more effective at lift generation than the 0.80 z/b location. Pratt found a much greater increase in lift performance at the 0.80 z/b location (28.7%) compared to Salmi (6.5%). Both saw minimal change in the stall angle.

Walker [10] tested an NACA 64_3-618 untapered swept rectangular wing and a boundary-layer fence at 0.7 z/b at a Reynolds number of 100,000 (38 mph). He saw also minimal change in the stall angle, but experienced a 12.8% increase C_{Lmax} compared to the baseline, which was larger than the increase Pratt [2] and Salmi [1] studies. This is additionally notable because because Walker uses a lower aspect ratio than in previous swept wings. The use of an AFC blowing slot with $C_\mu = 11.9\%$ resulted in a 14.3% increase in C_{Lmax}. While Walker did not see much increase in the angle of attack where C_{Lmax} occurred, he saw significant delay in the angle of attack where the wing stalled.

The present study used a swept delta wing instead of swept rectangular wing.

The BLF model had an 8.7% increase in C_{Lmax} compared to the baseline, which is similar to the values found by Pratt and Salmi. However, the delta wing AFC saw an enormous increase in lift compared to Walker's AFC, even with comparable C_μ values. The aspect ratio for this study was 2.7, which should have a lower C_{Lmax} values than a similar wing with a higher aspect ratio.

Comparing the C_L vs. α trends of Walker (Fig. 56a) and the current study (Fig. 52b), there appears to be a difference in how the AFC impacts the lift. For Walker's swept rectangular wing, the addition of the AFC slot follows the trend of the BLF model, with a similar C_{Lmax} value but also causing a significant extension in the angle of attack that stall occurs. The passive BLF drops off around 27°, while the AFC maintains lift until 36°.

With the current study, even the lowest flow rate tested (200 SLPM, $C_\mu = 0.49\%$) results in the entire C_L vs. α curve shifting up. The curve is extended further as the flow rate increase. This results in incremental increases in C_{Lmax}. Another factor that contributes to the high percentage increase in C_{Lmax} is that the increase is taken with reference to the baseline model. Delta wings are not optimized for lift generation, and the baseline delta wing model has a much lower lift ($C_{Lmax} = 0.805$) than Walker's swept wing ($C_{Lmax} = 1.33$).

Because delta wings do not have a sudden stall characteristic, there is not a noticeable delay in the stall for the lower C_μ AFC configurations. Even the baseline configuration has a relatively flat curve. At higher blowing ratios, lift continues to be generated at higher angles of attack, but the stall occurs more suddenly.

Additionally, all of the Walker et al. slot flow rates tested generated less lift compared to the baseline at lower angles of attack, and it is only around 20° that the slot models begin to experience higher lift numbers. The two lowest flow rates tested ($C_\mu = 0.69\%$ and $C_\mu = 2.77\%$) have very little benefit compared to the baseline

model, and clearly under-perform compared to the passive BLF model.

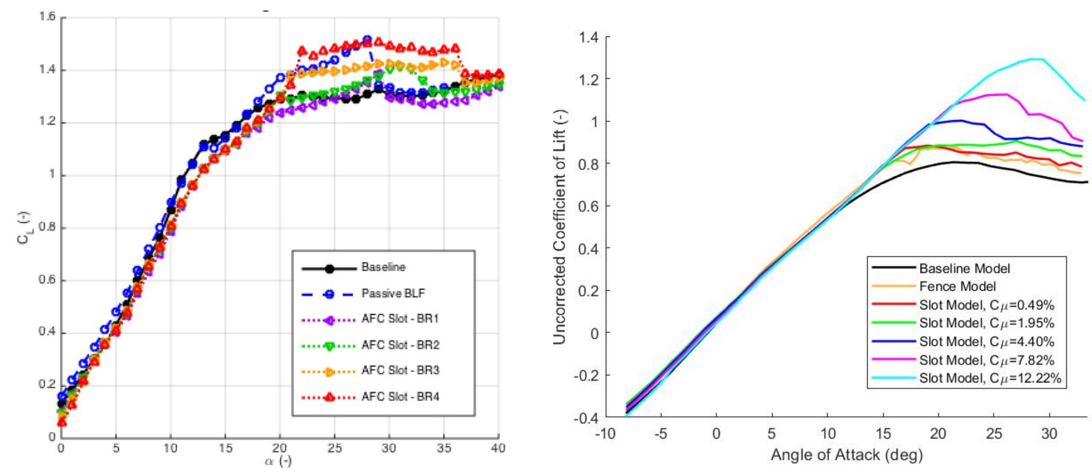

(a) Walker et al. Data, Re = 100,000 (b) Current Study Data, Re = 500,000

Figure 52. Uncorrected Coefficient of Lift Comparison, 45 mph

One of big issues that Walker et al. found with the application of passive and active boundary-layer fences caused a sudden increase in C_M at high angle of attacks, which corresponds to a destabilizing pitch up near stall. It was a point of interest for this investigation to see if that same pitch up tendency would be present with delta wings.

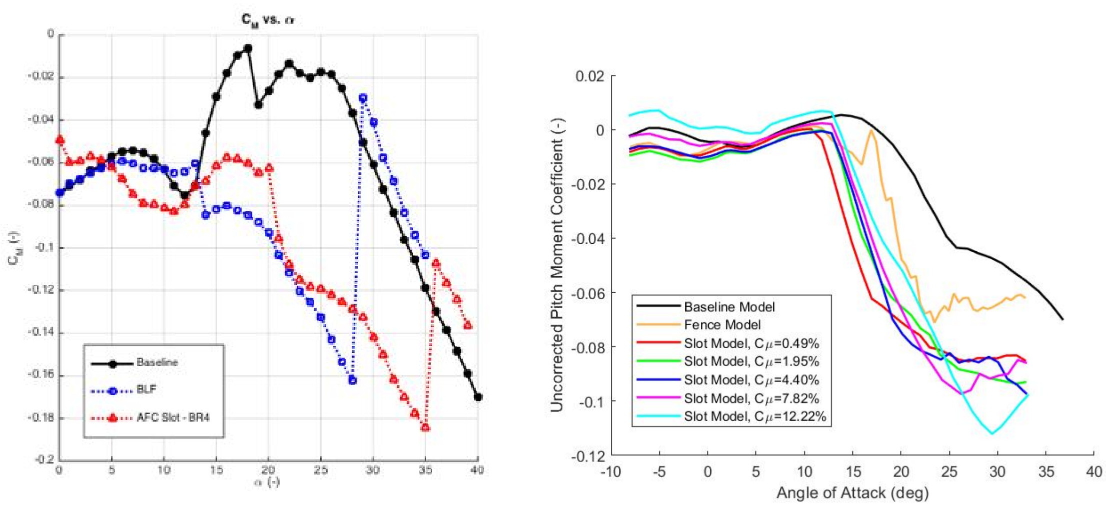

(a) Walker et al. Data, Re = 100,000 (b) Current Study Data, Re = 500,000

Figure 53. Uncorrected Pitch Moment Coefficient

Demoret Data, Uncorrected for Slot Forces				
Configuration	**Flow rate (SLPM)**	**C_μ**	**Percentage ΔC_{Lmax}**	**ΔC_{Lmax}**
BLF	-	-	8.7%	0.07
Slot Model	200	0.49%	9.7%	0.08
	400	1.95%	12.4%	0.10
	600	4.40%	24.3%	0.20
	800	7.82%	39.8%	0.32
	1000	12.22%	60.2%	0.49

Walker et al Data, Uncorrected for Slot Forces				
Configuration	**Blowing Ratio**	**C_μ**	**Percentage ΔC_{Lmax}**	**ΔC_{Lmax}**
BLF	-	-	14.3%	0.19
Slot Model	1	0.69%	4.5%	0.06
	2	2.77%	6.8%	0.09
	3	6.23%	7.5%	0.10
	4	11.08%	12.8%	0.17

Table 7. Uncorrected Comparison with Walker et al., 45 mph

This sharp pitch up can be seen in Walker's C_M vs. α plot (Fig. 53a). Comparatively, the current study does not have this peak (Fig. 53b). The lack of this "hard stall" characteristic with the delta wing model is an encouraging indicator about the use of flow control on a delta wing.

Because much of the current study operated as a continuation of the Walker et al, the significant differences in C_{Lmax} values were an unexpected result. There was evidence that the entrainment effect was providing an additional increase in lift compared to the passive BLF, but that does not account for the differences seen. The presence of vortex lift is a possible differentiator between the swept delta wing and the swept rectangular wing, but the delta wing did not have the high sweep angle normally associated with strong leading edge vortcies.

Walker's wing design had an internal tube that opened into a long, thin chamber that spanned the length of the slot. This design resulted in a less uniform velocity profile along the slot (shown in Figure 55b) instead of the ideal average slot velocity profile (shown in Figure 55a.)

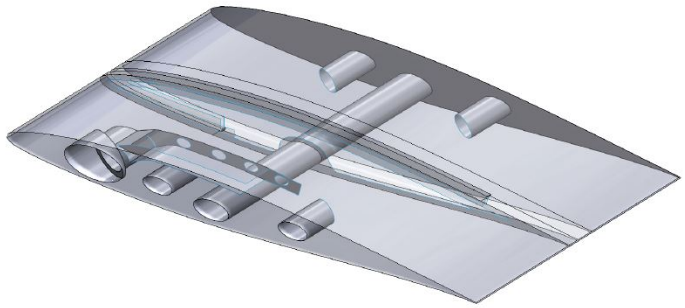

Figure 54. Walker et al. CAD model of AFC slot geometry for modular 2" wingspan

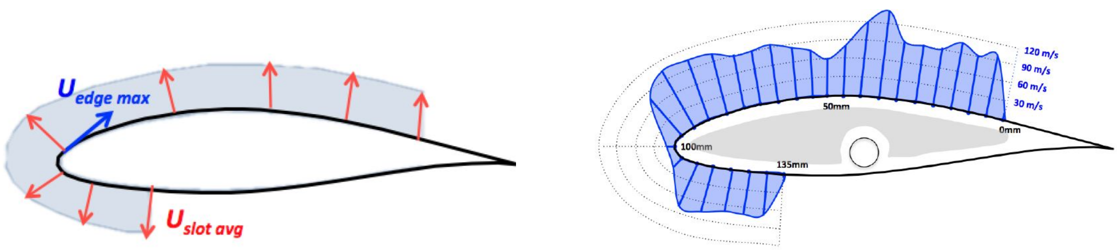

(a) Ideal Uniform Wall Normal Blowing

(b) Walker Experimental Benchtop AFC Slot, BR=3

Figure 55. Velocity Distribution

Based on Walker's benchtop velocity distribution (Fig 55b), one can estimate the resultant slot force vector as basically straight up. Looking at his benchtop lift and drag forces (which he nondimensionalized for easier comparison with his other results), the trends fit this resultant vector estimation. Drag is basically zero and lift is maximized at 0°, indicating the resultant vector is pointing straight down relative to the model (Fig 58). As angle of attack increases, the thrust (or negative drag) component increases and the lift decreases (Fig. 57). Walker did not report the benchtop pitch moment characteristics.

Table 8 shows the corrected values with the slot forces being subtracted from the original value.

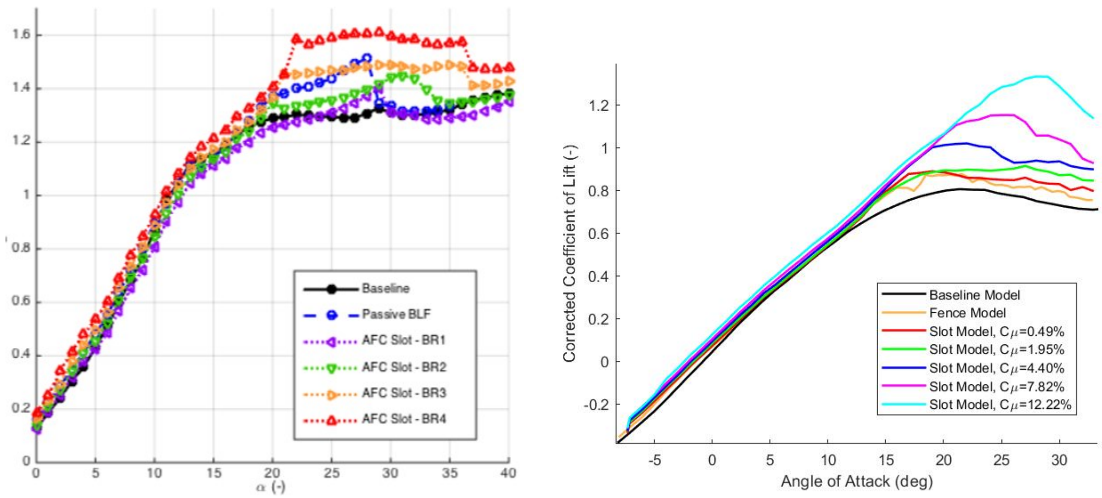

(a) Walker et al. Data, Re = 100,000 (b) Current Study Data, Re = 500,000

Figure 56. Corrected Coefficient of Lift Comparison

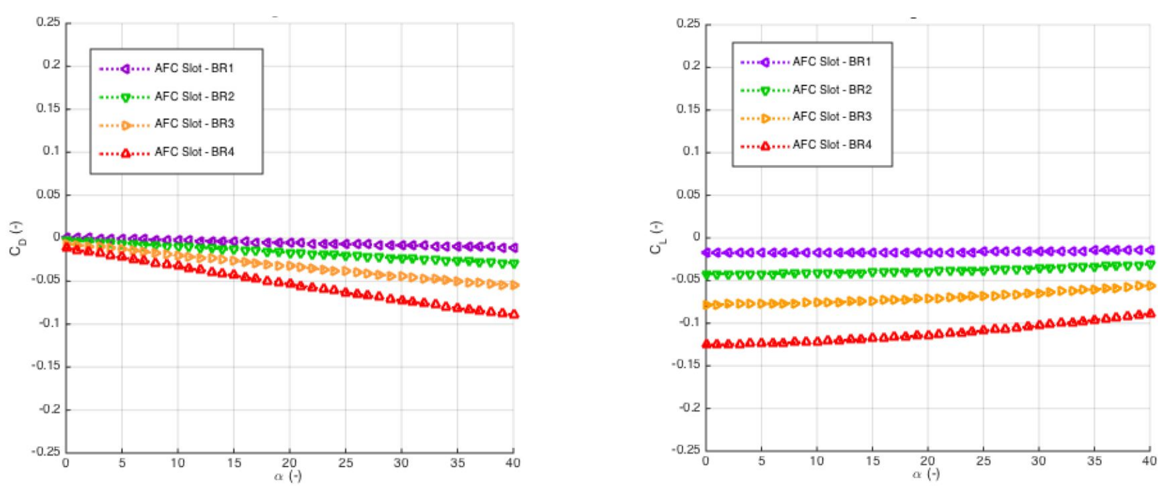

(a) Coefficient of Drag (b) Coefficient of Lift

Figure 57. Walker et al. Benchtop Forces

Demoret Data, Corrected for Slot Forces				
Configuration	Flow rate (SLPM)	C_μ	Percentage ΔC_{Lmax}	ΔC_{Lmax}
BLF	-	-	8.7%	0.07
Slot Model	200	0.49%	10.3%	0.08
	400	1.95%	13.5%	0.10
	600	4.40%	26.6%	0.21
	800	7.82%	43.0%	0.35
	1000	12.22%	65.2%	0.53

Walker et al Data, Corrected for Slot Forces				
Configuration	Blowing Ratio	C_μ	Percentage ΔC_{Lmax}	ΔC_{Lmax}
BLF	-	-	14.3%	0.19
Slot Model	1	0.69%	5.3%	0.07
	2	2.77%	9.0%	0.12
	3	6.23%	11.3%	0.12
	4	11.08%	20.3%	0.27

Table 8. Corrected Comparison with Walker et al., 45 mph

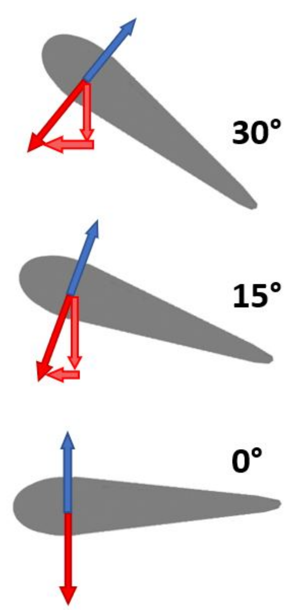

Figure 58. Walker et al. Lift and Drag Components Diagram

V. Conclusion

5.1 Conclusion

The effect of passive and active boundary-layer fences (BLF) on performance is evaluated on a NACA 0012 delta wing (c_{root} = 14in, c_{tip} = 2.8in, $\Lambda = 45°$, b = 23.5in) at a Reynolds number of Re = 5.0 x 10^5 based on the root chord. The performance improvements of a passive BLF are replicated and improved upon using an active flow control (AFC) fluidic fence created by a wall-normal steady-blowing jet from a slot. The application of a passive BLF at a spanwise location of 70% z/b resulted in an 8.7% increase in C_{Lmax} compared to the baseline, with no destabilizing pitch moment characteristics and no significant change in angle of attack where stall occurs. The application of an AFC slot operating from C_μ = 0.49% to 12.22% resulted in an increase in C_{Lmax} ranging from a 9.7% to 60.3% respectively and no destabilizing pitch moment characteristics. The blowing configuration C_μ = 0.49% resulted in an early onset stall of -2.4°, while the configurations operating from C_μ = 1.95% to 12.22% resulted in a delay of stall between 0.7° to 8.0° angle of attack respectively. The fluorescent tuft flow visualization method provided evidence that the AFC slot maintained a significant region of attached flow outboard of the fence past the point that the passive BLF had separated. There was also indication of an entrainment phenomenon, but more investigation is required to assert this definitively. Figure 59 illustrates the overall conclusion visually; the addition of the AFC slot was able to replicate and improve upon the performance benefits of the passive BLF. These performance gains will allow for significant performance benefits at higher angles of attack (with AFC turned on), while still allowing for efficient performance at lower angles of attack (with AFC turned off).

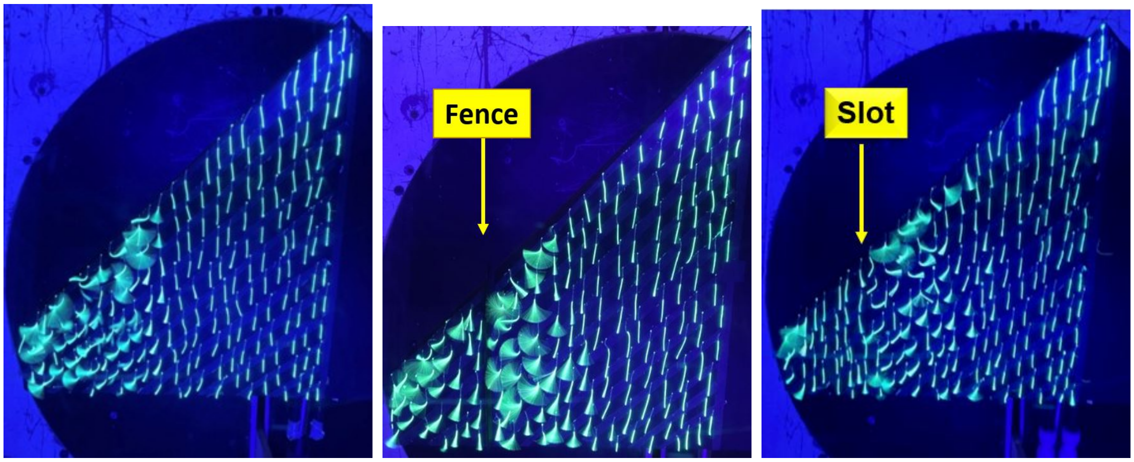

(a) Baseline Model (b) Fence Model (c) Slot Model, 800 SLPM

Figure 59. Fluorescent Tuft Visualization, 15°

5.2 Future Work

First priority for future investigation is to ensure there are no issues with the setup. The second priority will be to determine the mechanism by which the AFC slot operates differently compared to a swept wing. This investigation had comparable lift gains to previous investigations when looking at the passive BLF, but there were significant lift gains for the AFC slot. Future work will look to validate these gains and gain a greater understanding of why these gains are so large.

The first step to validate the high ΔC_L gains will be to repeat all analysis at different Reynolds numbers. This will be accomplished by changing the operating freestream velocity to 30 mph and 60 mph. The use of computational fluid dynamics (CFD) will allows for higher Reynolds number testing without regard for the limits of the force balance or the wind tunnel. Computational results with similarly high gains can be compared to the CFD analysis performed by in Walker's investigation. CFD also provides the ability to isolate experiment variables more effectively, thus allowing a thorough optimization study of slot spanwise location, slot width, slot length, and slot wrap-around orientation. To accurately model the slot velocity distribution for

any CFD model, the single-wire hotwire probe or pitot tube setup should be used to determine the experimental velocity distribution out of the slot (producing a plot similar to that seen in Figure 55b).

The use of CFD would also provide additional flow visualization, including the presence of LEVs and counter-rotating vortices. The use of the 3-D hotwire and stereo-PIV would also allow for additional insight about the 3-dimensional flow field. The fluorescent tufts provided surface flow visualization, but the use of tape to affix the tufts results in a less "clean" configuration compared to gluing the tufts. Eventually, tufts should be permanently attached with a lacquer-type adhesive applied with a hypodermic syringe, which is a method was adapted from Dobney et al. [33].

This investigation compared a 30° swept rectangular wing with a 45° swept delta wing, and found much higher gains for the delta wing. The LEV phenomenon discussed in Section 2.2 is typically associated with highly-swept delta wings, which are greater than 45°. A sweep of the delta wing in this experiment is right at the cutoff where LEVs are expected to form. The more moderate sweep angle of 45° was chosen to reflect operational platforms like the F-16, but retesting at a lower and higher sweep angles should help partially isolate the impact of the LEVs, and help determine the extent vortex lift is contributing to high ΔC_L gains.

Appendix A. MATLAB Code for Processing Load Cell Data

```

%******   Adapted for the AFC setup Balance AFIT-1 by Lt. Anna Demoret **************
%**********     Calculation of Lift, Drag, Moments *******************

%This Code will transfer measured Forces and Moments on the AFIT 1 balance to Wind
%(earth) centered frame of reference by correctiing for tare effects, balance
%interactions, and wind tunnel irregularities, then gives a file with all the
%corrected data
%
clear;
clc;
close all;
format long
% %*****************************************************
%                                INPUT DECK
%FIRST FILL THE FOLLOWING INFORMATION (modified by A. Demoret on 19 August)
%% Import Data File
opts = spreadsheetImportOptions("NumVariables", 24);

% Specify sheet and range
opts.Sheet = "Slot_800slpm_45_2";
opts.DataRange = "A2:X1261";

% Specify column names and types
opts.VariableNames = ["AoA", "Yaw", "Speed", "Norm", "Pitch", "Axial", "Side", "Yaw1", "Roll", "L2", "A2", "RFO", "RFI", "RAO", "RAI", "LFO", "LFI", "LAO", "LAI", "degF", "in_Hg", "secs", "MassFlowA", "MassFlowB"];
opts.VariableTypes = ["double", "double", "double", "double", "double", "double", "double", "double", "double", "double", "double", "double", "double", "double", "double", "double", "double", "double", "double", "double", "double", "double", "double", "double"];

% Import the data
Slot800slpm452 = readtable("C:\Users\13215\Documents\AFIT\Thesis\AFC\AFC_2\Slot_800slpm_45_2.xlsx", opts, "UseExcel", false);


%% Import Tare data
opts = spreadsheetImportOptions("NumVariables", 24);

% Specify sheet and range
opts.Sheet = "Slot_Tare_AirOff_TunnelOff";
opts.DataRange = "A2:X316";

% Specify column names and types
opts.VariableNames = ["AoA", "Yaw", "Speed", "Norm", "Pitch", "Axial", "Side", "Yaw1", "Roll", "L2", "A2", "RFO", "RFI",
```

```
"RAO", "RAI", "LFO", "LFI", "LAO", "LAI", "degF", "in_Hg", "secs", "MassFlowA", "MassFlowB"];
opts.VariableTypes = ["double", "double", "double", "double", "double", "double", "double", "double", "double", "double", "double", "double", "double", "double", "double", "double", "double", "double", "double", "double", "double", "double", "double", "double"];

% Import the data
SlotTareAirOffTunnelOff = readtable("C:\Users\13215\Documents\AFIT\Thesis\AFC\AFC_2\Slot_Tare_AirOff_TunnelOff.xlsx", opts, "UseExcel", false);

clear opts

%%
DataFile=table2array(Slot800slpm452([2:end],:));
TareFile=table2array(SlotTareAirOffTunnelOff([2:end],:));

Masskg=2.05;                                  % Mass of the wing kgs
T_room = mean(DataFile(:,20)) + 459.67;          %deg R ****Changed for each day of testing****
P_barro =  mean(DataFile(:,21)) * 0.4911541;     %Psi ****Changed for each day of testing****

% % % load('Tare_TunnelOff');                     %tarefile tare.txt
% % % TareFile = lowaspect_tare(:,1:9);
% % % load Sweep_15fts;                           %datafile .txt
% % % DataFile = lowaspect_50mverocph(:,1:9);

% % for ii=1:9        % plot cols of TareFile for visual
% %     plot(TareFile(:,ii));   waitforbuttonpress();
% % end
% % close
AngleOffsetofModel=-7.82

%Offset distances from the Mounting Block to the Model CG (inches)
MAC=1.186
X_cmb = 2.375-MAC;  % the locaton actual aero center is 1.15" behind the screw,
% from the nose, the mount is 7.5" back adn the cg is 6.8" back
Y_cmb = 0;% 2.375 -0.118-0.1; % use +0.22 for c/4 for b = 11.4" wings           %inches  (from origin @ balance center w/ + forward)
Z_cmb = 0;                                   %inches  (from origin @ balance center w/ + down)

% Required for the Solid body blockage corrections due to wing and fuselage

Body_Volume =100.21 / 12^3 ;       %(ft^3): Get from solidworks file
Wing_Area = ((((14.375-2.88)*23.125)/2)+23.125*2.88)/ 12^2;             %(ft^2): Get from solidworks file
```

```
% %
% % % Required for the Pitching Moment Correction
% %
% %  l_t =  9/12;                                          % ft = length from tail MAC to aircraft CG
% %  Span_t =23.125 / 12;                                   % ft = horizontal span
% %  Tail_Area = (9.42962435) / 144;                        % ft^2 =  horizontal tail area
% % %
% BEFORE CONTINUING IT IS NECCESARY TO CHANGE THE NAME:
% 1. INPUT DATA FILE 2. INPUT DATA TARE FILE 3. OUTPUT DATA FILE

% ########################################################################
%II.-   Room Conditions and Model Specifics :
%       UNITS are in Ft, Sec, lbm, Psf, Rankine, fps
% ########################################################################

Mass = (Masskg * 1000) * 0.0022046;                                              %lbm
Gas_Const = 1716;                                                                                  %ft-lbf/Slug-R
Density = (P_barro * 144)/(1716 * T_room);                                  %lbm/ft^3 or lbf-s^2/ft^4
Root_Chord = 2.88 * (1/12);                                                                %ft
Span = 23.125 / 12;    %Import                                                                  %ft
Aspect_Ratio = Span^2 / Wing_Area;
Kinematic_Viscosity = .372e-6;                                                        %slug/ft-s
Speed_of_Sound = sqrt(1.4 * T_room * Gas_Const);                      %fps

%##########################################################
%III.-     Solid body blockage corrections due to wing and fuselage
%##########################################################% page 369 of Barlow's Low Speed Wind Tunnel Testing book
K_1 = 1.01;%0.9;
K_3 = .915;%0.93;
delta = 0.1125;
Tau_1 = 0.866; %0.83125
X_Section = (31/12)*(44/12);                          %AFIT wind tunnel test section in ft^2
Wing_Volume = Body_Volume;                            % ft^3

% This depends on whether it's a full a.c. or flat wing
Epsilon_sb_w = (K_1*Tau_1*Wing_Volume) / X_Section^(3/2);
%Epsilon_sb_b = (K_3*Tau_1*Body_Volume) / X_Section^(3/2);
%Epsilon_tot = Epsilon_sb_w + Epsilon_sb_b;
Epsilon_tot = Epsilon_sb_w ;
```

```
%#########################################################
% III.-  Load the static tare data for the alpha sweep w/o the wind ,
%        separate each force from the file, and fit a 4th order poly
%        as an x-y plot (AoA vs.Force) for each of the 6 force sensors.
%#########################################################

j=1;    k=1;    L=length(TareFile);

for i=1:L                                   %Run for all data points # of rows
    if i~=L                                 %if current row is not last row, go to next
        NEXT=i+1;                           %set next equal to the value of the next row
        VALUE2=TareFile(NEXT,1)  %set value2 as next row column 1
    else if i==L     %unless the it is the last value
        VALUE2=50;   %value2 set to 50 to end the sequence
    end
    end
    A(j,:)=TareFile(i,:);    %set row j of A equal to row i of TareFile
    VALUE1=TareFile(i,1);    %set value1 equal to row i column 1 of TareFile
    if VALUE1==VALUE2    %if value1 equals value2, go to next row
        j=j+1;
    else if VALUE1~=VALUE2   %if value1 and value2 are different check
        if length(A(:,1))<5         %if less than 5 values, ignored due to angle change
            j=1;
            clear A;
        else if length(A(:,1))>5  %if more than 5 values
                C=length(A(:,1));     %find length of A
                for m=1:9      %Average all rows of the like values in A
                    B(k,m)=mean(A(4:C,m));     %disregarding first 3 for vibrations
                end
                j=1;
                k=k+1;
                clear A
        end
        end

    end
    end
end

if B(k-1,1)<B((k-2),1)
    B=B(1:(k-2),:);
```

```
end

tare=[B];

%_________________________________End of inserted code
[row,col] = size(tare);

for k = 1:row

    theta_tare(k,:,:)    = tare(k,1).* (pi/180);
    NF_tare(k,:,:)       = tare(k,4);
    PM_tare(k,:,:)       = tare(k,5);
    AF_tare(k,:,:)        = tare(k,6);
    SF_tare(k,:,:)       = tare(k,7);
    YM_tare(k,:,:)       = tare(k,8);
    RM_tare(k,:,:)        = tare(k,9);

end

NF_poly = polyfit(theta_tare,NF_tare,4);
PM_poly = polyfit(theta_tare,PM_tare,4);
AF_poly  = polyfit(theta_tare,AF_tare,4);
SF_poly = polyfit(theta_tare,SF_tare,4);
YM_poly = polyfit(theta_tare,YM_tare,4);
RM_poly  = polyfit(theta_tare,RM_tare,4);

%#######################################################################
%IV.- Load the specific test run files,
%#######################################################################


clear ('AA','B','C','L')
%________________________________________
%load data1.txt;          % Raw data file to be read in:
% FIRE=DataFile(:,:);                      %

j=1;    k=1;    L=length(DataFile);

for i=1:L               %Run for all data points # of rows
    if i~=L  %if current row is not last row, go to next
        NEXT=i+1;   %set next equal to the value of the next row
        VALUE2=DataFile(NEXT,1);             %set value2 as next row column 1
    else if i==L          %unless the it is the last value
        VALUE2=50;   %value2 set to 50 to end the sequence
    end
    end
    A(j,:)=DataFile(i,:);     %set row j of A equal to row i of DataFile
    VALUE1=DataFile(i,1);                    %set value1 equal to row i column 1 of DataFile
    if VALUE1==VALUE2                    %if value1 equals value2, go to next row
```

```
        j=j+1;
    else if VALUE1~=VALUE2       %if value1 and value2 are different check
        if length(A(:,1))<5                     %if less than 5 values, ignored due to angle change
            j=1;
            clear A;
        else if length(A(:,1))>  %if more than 5 values
                C=length(A(:,1));       %find length of A
                for m=1:9                      %Average all rows of the like values in A
                    B(k,m)=mean(A(4:C,m));     %disregarding first 3 for vibrations
                end
                j=1;
                k=k+1;
                clear A
        end
        end
    end
    end
end

%  if B(k-1,1)<B((k-2),1)
%      B=B(1:(k-2),:)
%  end

sample_data=[B];

[row2,col2] = size(sample_data);


for i = 1:row2

%Angles of the model during test runs (Roll, Pitch {AoA}, Yaw {Beta}):

phi                 = 0;
theta(i,:)          = sample_data(i,1) .* (pi/180)-(0*pi/180);     % alpha     %radians
si(i,:)             = sample_data(i,2) .* (pi/180);                 %yaw negative beta          %radians
Wind_Speed(i,:)     = sample_data(i,3) .* (5280/3600);              %fps

%Flight Parameters (Re#, Ma#, Dynamic Pressure):
q = (.5 * Density) .* Wind_Speed.^2;    %lbf/ft^2
q_Corrected = q .* (1 + Epsilon_tot)^2; %lbf/ft^2
Wind_Speed_Corrected = Wind_Speed .* (1 + Epsilon_tot); %fps
Mach_Number = Wind_Speed_Corrected ./ Speed_of_Sound;   %NonDimensional
Reynolds_Number = ((Density * Root_Chord) .* Wind_Speed_Corrected) ./ Kinematic_Viscosity;  %NonDimensional
Flight_Parameters = [Mach_Number Reynolds_Number q_Corrected];

%individual forces and moments for each sensor:

```

```
%NEW NOTATION
NF_test(i,:,:)       = sample_data(i,4);
PM_test(i,:,:)       = sample_data(i,5);
AF_test(i,:,:)        = sample_data(i,6);
SF_test(i,:,:)       = sample_data(i,7);
YM_test(i,:,:)       = sample_data(i,8);
RM_test(i,:,:)        = sample_data(i,9);

% ########################################################################
%V.-   Subtract the effect of the static
%      weight with the tare polynominals above
% ########################################################################


%Evaluating the actual test theta angle (AoA) in the tare polynominal to
%determine the tare values for the angles tested in each run.
%
NF_eval = polyval(NF_poly,theta);
PM_eval = polyval(PM_poly,theta);
AF_eval  = polyval(AF_poly,theta);
SF_eval = polyval(SF_poly,theta);
YM_eval = polyval(YM_poly,theta);
RM_eval  = polyval(RM_poly,theta);

%The Time-Averaged (raw) forces and momentums NF,AF,SF,PM,YM AND RM measurd in the wind
%tunnel (body axis) with the tare effect of the weight subtracted off.

NF_resolved = NF_test - (NF_eval);
PM_resolved = PM_test - (PM_eval);
AF_resolved  = AF_test -  (AF_eval); % check this 8-17-04
SF_resolved = SF_test - (SF_eval);
YM_resolved = YM_test - (YM_eval);
RM_resolved  = RM_test -  (RM_eval);


Forces_minus_tare = [NF_resolved, AF_resolved, PM_resolved, RM_resolved, YM_resolved, SF_resolved]';

% ########################################################################
%VI.- CORRECT FORCES AND MOMENTS FOR BALANCE INTERATIONS (body axis)
% ##########################################################################

%USING THE REDUCTION EQUATIONS SET A MAXIMUN NUMBER OF INTERATIONS
%TO AVOIDE INFINIT LOOP
MAXIT=100;
```

```
%SET THE LIMIT FOR THE DIFFERENCE BETWEEN INTERATIONS(CRITERIA FOR FINISH THE INTERATIONS)
LIMIT=  10E-14;

%MATCHING EACH NAME WITH  THE DATA
% Prof. Reeder added :i
MNF=NF_resolved(i);
MAF=AF_resolved(i);
MPM=PM_resolved(i);
MRM=RM_resolved(i);
MYM=YM_resolved(i);
MSF=SF_resolved(i);

%INPUT OF THE CONSTANTS VALUES FROM THE MATRIX FOR SENSITIVITIES AND INTERATIONS
K=[0  4.399268E-4  1.070164e-3  -2.335572e-03  -4.978426e-03  -4.588672E-03  ...
   3.452811E-06  8.908818E-05  -2.295160E-07  -6.908871E-06  -4.755186E-06  1.454754E-05...
   1.320818E-05  1.801978E-04  8.21285E-07  -2.1139E-06  -3.828756E-06  1.00793E-07...
   -5.614922E-06  4.63941E-07  -1.783175e-06 -1.920484E-05  -1.425469e-04  -4.194190e-04...
   2.138726e-05  2.677231e-05  -8.068639e-06  8.368769e-02  0  4.670090E-03...
   1.351644E-02  -7.673816E-03  -1.531559E-02  -1.276559E-04  8.851767E-05  1.706343e-04...
  -8.531869E-06  4.02935E-06  4.933901E-06  5.555060E-05  2.191420E-05  -7.043307E-06...
   -2.045899E-06  -2.309221E-05  5.579486E-05  -5.740601E-06  4.804542E-06  4.235623E-06...
   4.16271e-04  -5.293348E-04  -1.403228E-05  1.885284E-05  -1.51005E-04  -1.260329E-04...
   2.935104e-3  -1.093373e-03  0  1.910192E-02  -4.622585e-03  1.560107E-03...
   8.87933E-08  9.939944E-05  -2.549351E-06  3.391426E-05  2.103073E-05  -2.345968E-05...
   5.470224E-05  -2.31077E-04  -1.503620E-06  -1.723195E-05  -2.187583E-05  1.976746E-06...
   -4.254878E-06  -3.588016E-06 -8.111438E-06  -3.065255E-05  -2.936682E-04  -4.061827E-04...
   3.25584E-05  3.201654E-05  -1.306233E-05  8.772813e-04  9.531368e-04  1.339564e-04...
   0  5.82722e-03  -5.94518e-03  3.049844e-06  -7.245581e-06  3.568688e-07...
   2.970840E-07  -6.31310E-06  -1.015843E-05  -3.438158E-05  5.038598E-06  1.422742E-05...
   -1.24878E-07  1.278136E-05  -5.37534E-06  5.285862E-06  -4.379908E-08  1.037692E-05...
   -7.676464E-06  -7.57301E-07  2.336961E-06  8.728879E-06  2.00573e-07  -1.61823e-06...
   -5.213668e-03  -8.336189e-04  3.526537e-03  6.566634e-03  0  5.378555E-03...
   -3.449386E-06  -2.280605E-05  7.700084E-07  3.251194E-04  -2.708812E-05  2.574849E-06...
   5.154723E-06  6.11821E-06  2.324892E-05  -2.15232E-04  1.235646E-04  5.201382e-07...
   3.022627E-04  -2.654001E-05  7.96853E-06  4.673283E-05
```

```
-1.036097E-06  6.249374E-05...
-2.281551E-06  1.221136E-06  1.844858E-05  9.249618e-03  1.559993E-04  -6.961975e-04...
8.275789E-03  -1.040704E-02  0  -2.966965E-06  -3.257055E-08  2.350408E-07  4.046199E-04...
-2.656955E-05  7.998584E-06  1.644095E-05  2.397679E-07  2.278976E-05  -1.846214E-04...
1.26536E-04  -3.296272E-07  1.492102E-04  -2.100877E-05  5.076868E-07  3.457275E-06...
-6.187814E-06  -2.994841e-06  1.050205e-06  1.512628e-06  -1.450988e-05];

%COMPUTE THE UNCORRECTED FORCES AND MOMENTS BY
%CONSIDERING THAT THE PRIME SENSITIVITY CONSTANTS ARE ALREADY APLIED:

NF1=MNF;
AF1=MAF;
PM1=MPM;
RM1=MRM;
YM1=MYM;
SF1=MSF;

%FOR THE FIRST INTERACTION LET US INITIALIZE THE VALUES OF FORCES AND
%MOMENTS WITH THE VALUES OF THE UNCORRECTED FORCES AND MOMENTS

NF(1)=NF1;
AF(1)=AF1;
PM(1)=PM1;
RM(1)=RM1;
YM(1)=YM1;
SF(1)=SF1;

%DOING THE INTERACTION EQUATIONS:

for n=2:MAXIT;


NF(n)=NF1-((K(2)*AF(n-1))+(K(3)*PM(n-1))+(K(4)*RM(n-1))+(K(5)*YM(n-1))+(K(6)*SF(n-1))+(K(7)*NF(n-1)^2)+...
        (K(8)*(NF(n-1)*AF(n-1)))+(K(9)*(NF(n-1)*PM(n-1)))+(K(10)*(NF(n-1)*RM(n-1)))+(K(11)*(NF(n-1)*YM(n-1)))+...
        (K(12)*(NF(n-1)*SF(n-1)))+(K(13)*(AF(n-1)^2))+(K(14)*(AF(n-1)*PM(n-1)))+(K(15)*(AF(n-1)*RM(n-1)))+...
        (K(16)*(AF(n-1)*YM(n-1)))+(K(17)*(AF(n-1)*SF(n-1)))+(K(18)*(PM(n-1)^2))+(K(19)*(PM(n-1)*RM(n-1)))+...
        (K(20)*(PM(n-1)*YM(n-1)))+(K(21)*(PM(n-1)*SF(n-1)))+(K(22)*(RM(n-1)^2))+(K(23)*(RM(n-1)*YM(n-1)))+...
        (K(24)*(RM(n-1)*SF(n-1)))+(K(25)*(YM(n-1)^2))+(K(26)*(YM(n-1)*SF(n-1)))+(K(27)*(SF(n-1)^2)));

AF(n)=AF1-((K(28)*NF(n-1))+(K(30)*PM(n-1))+(K(31)*RM(n-1))+(K(32)*YM(n-1))+(K(33)*SF(n-1))+(K(34)*NF(n-1)^2)+...
        (K(35)*(NF(n-1)*AF(n-1)))+(K(36)*(NF(n-1)*PM(n-1)))+(K(37)*(NF(n-1)*RM(n-1)))+(K(38)*(NF(n-1)*YM(n-1)))+...
```

```
          (K(39)*(NF(n-1)*SF(n-1)))+(K(40)*(AF(n-1)^2))+(K(41)
             *(AF(n-1)*PM(n-1)))+(K(42)*(AF(n-1)*RM(n-1)))+...
          (K(43)*(AF(n-1)*YM(n-1)))+(K(44)*(AF(n-1)*SF(n-1)))+(
             K(45)*(PM(n-1)^2))+(K(46)*(PM(n-1)*RM(n-1)))+...
          (K(47)*(PM(n-1)*YM(n-1)))+(K(48)*(PM(n-1)*SF(n-1)))+(
             K(49)*(RM(n-1)^2))+(K(50)*(RM(n-1)*YM(n-1)))+...
          (K(51)*(RM(n-1)*SF(n-1)))+(K(52)*(YM(n-1)^2))+(K(53)
             *(YM(n-1)*SF(n-1)))+(K(54)*(SF(n-1)^2)));

PM(n)=PM1-((K(55)*NF(n-1))+(K(56)*AF(n-1))+(K(58)*RM(n-1))+(K
   (59)*YM(n-1))+(K(60)*SF(n-1))+(K(61)*NF(n-1)^2)+...
          (K(62)*(NF(n-1)*AF(n-1)))+(K(63)*(NF(n-1)*PM(n-1)))+(
             K(64)*(NF(n-1)*RM(n-1)))+(K(65)*(NF(n-1)*YM(n-1)))
             +...
          (K(66)*(NF(n-1)*SF(n-1)))+(K(67)*(AF(n-1)^2))+(K(68)
             *(AF(n-1)*PM(n-1)))+(K(69)*(AF(n-1)*RM(n-1)))+...
          (K(70)*(AF(n-1)*YM(n-1)))+(K(71)*(AF(n-1)*SF(n-1)))+(
             K(72)*(PM(n-1)^2))+(K(73)*(PM(n-1)*RM(n-1)))+...
          (K(74)*(PM(n-1)*YM(n-1)))+(K(75)*(PM(n-1)*SF(n-1)))+(
             K(76)*(RM(n-1)^2))+(K(77)*(RM(n-1)*YM(n-1)))+...
          (K(78)*(RM(n-1)*SF(n-1)))+(K(79)*(YM(n-1)^2))+(K(80)
             *(YM(n-1)*SF(n-1)))+(K(81)*(SF(n-1)^2)));

RM(n)=RM1-((K(82)*NF(n-1))+(K(83)*AF(n-1))+(K(84)*PM(n-1))+(K
   (86)*YM(n-1))+(K(87)*SF(n-1))+(K(88)*NF(n-1)^2)+...
          (K(89)*(NF(n-1)*AF(n-1)))+(K(90)*(NF(n-1)*PM(n-1)))+(
             K(91)*(NF(n-1)*RM(n-1)))+(K(92)*(NF(n-1)*YM(n-1)))
             +...
          (K(93)*(NF(n-1)*SF(n-1)))+(K(94)*(AF(n-1)^2))+(K(95)
             *(AF(n-1)*PM(n-1)))+(K(96)*(AF(n-1)*RM(n-1)))+...
          (K(97)*(AF(n-1)*YM(n-1)))+(K(98)*(AF(n-1)*SF(n-1)))+(
             K(99)*(PM(n-1)^2))+(K(100)*(PM(n-1)*RM(n-1)))+...
          (K(101)*(PM(n-1)*YM(n-1)))+(K(102)*(PM(n-1)*SF(n-1)))
             +(K(103)*(RM(n-1)^2))+(K(104)*(RM(n-1)*YM(n-1)))
             +...
          (K(105)*(RM(n-1)*SF(n-1)))+(K(106)*(YM(n-1)^2))+(K
             (107)*(YM(n-1)*SF(n-1)))+(K(108)*(SF(n-1)^2)));

YM(n)=YM1-((K(109)*NF(n-1))+(K(110)*AF(n-1))+(K(111)*PM(n-1))
   +(K(112)*RM(n-1))+(K(114)*SF(n-1))+(K(115)*NF(n-1)^2)+...
          (K(116)*(NF(n-1)*AF(n-1)))+(K(117)*(NF(n-1)*PM(n-1)))
             +(K(118)*(NF(n-1)*RM(n-1)))+(K(119)*(NF(n-1)*YM(n
             -1)))+...
          (K(120)*(NF(n-1)*SF(n-1)))+(K(121)*(AF(n-1)^2))+(K
             (122)*(AF(n-1)*PM(n-1)))+(K(123)*(AF(n-1)*RM(n-1))
             )+...
          (K(124)*(AF(n-1)*YM(n-1)))+(K(125)*(AF(n-1)*SF(n-1)))
             +(K(126)*(PM(n-1)^2))+(K(127)*(PM(n-1)*RM(n-1)))
             +...
          (K(128)*(PM(n-1)*YM(n-1)))+(K(129)*(PM(n-1)*SF(n-1)))
             +(K(130)*(RM(n-1)^2))+(K(131)*(RM(n-1)*YM(n-1)))
             +...
          (K(132)*(RM(n-1)*SF(n-1)))+(K(133)*(YM(n-1)^2))+(K
             (134)*(YM(n-1)*SF(n-1)))+(K(135)*(SF(n-1)^2)));

SF(n)=SF1-((K(136)*NF(n-1))+(K(137)*AF(n-1))+(K(138)*PM(n-1))
   +(K(139)*RM(n-1))+(K(140)*YM(n-1))+(K(142)*NF(n-1)^2)+...
          (K(143)*(NF(n-1)*AF(n-1)))+(K(144)*(NF(n-1)*PM(n-1)))
```

```
            +(K(145)*(NF(n-1)*RM(n-1)))+(K(146)*(NF(n-1)*YM(n-1)))+...
            (K(147)*(NF(n-1)*SF(n-1)))+(K(148)*(AF(n-1)^2))+(K(149)*(AF(n-1)*PM(n-1)))+(K(150)*(AF(n-1)*RM(n-1)))+...
            (K(151)*(AF(n-1)*YM(n-1)))+(K(152)*(AF(n-1)*SF(n-1)))+(K(153)*(PM(n-1)^2))+(K(154)*(PM(n-1)*RM(n-1)))+...
            (K(155)*(PM(n-1)*YM(n-1)))+(K(156)*(PM(n-1)*SF(n-1)))+(K(157)*(RM(n-1)^2))+(K(158)*(RM(n-1)*YM(n-1)))+...
            (K(159)*(RM(n-1)*SF(n-1)))+(K(160)*(YM(n-1)^2))+(K(161)*(YM(n-1)*SF(n-1)))+(K(162)*(SF(n-1)^2)));


% SET THE LIMIT FOR THE DIFFERENCE BETWEEN INTERATIONS(CRITERIA FOR FINISH THE INTERATIONS)

DIFFNF(n)=abs(NF(n)-NF(n-1));
DIFFAF(n)=abs(AF(n)-AF(n-1));
DIFFPM(n)=abs(PM(n)-PM(n-1));
DIFFRM(n)=abs(RM(n)-RM(n-1));
DIFFYM(n)=abs(YM(n)-YM(n-1));
DIFFSF(n)=abs(SF(n)-SF(n-1));


if DIFFNF(n)&&DIFFAF(n)&&DIFFPM(n)&&DIFFRM(n)&&DIFFYM(n)&&DIFFSF(n) < LIMIT
 break

end

end

%disp('THE FINAL VALUES ARE (NF,AF,PM,RM,YM,SF):')
Corrected_Data(:,i)= [NF(n);AF(n);PM(n);RM(n);YM(n);SF(n)];

%disp('THE FINAL DIFFERENCE BETWEEN INTERATIONS ARE(FOR NF,AF,PM,RM,YM,SF) :')
%FINAL_DIFFERENCE=[DIFFNF(n),DIFFAF(n),DIFFPM(n),DIFFRM(n),DIFFYM(n),DIFFSF(n)]

%disp('THE NUMBER OF INTERATIONS USED WAS:')
%n

% ##############################################################################
%VII.- Calculation of the Axial, Side, & Normal Forces from the corrected balance
%      forces in the Body Axis reference frame
% ##############################################################################

Forces_b(:,i) = [Corrected_Data(2,i); Corrected_Data(6,i); Corrected_Data(1,i)];

```

```
%Calculation of the Drag, Side, & Lift Forces in the Wind Axis reference
%frame

Forces_w = [Forces_b(1,:).*cos(theta').*cos(si')+Forces_b(2,:).*sin(si')+Forces_b(3,:).*sin(theta').*cos(si');      %in radians
            -Forces_b(1,:).*sin(si').*cos(theta')+Forces_b(2,:).*cos(si')-Forces_b(3,:).*sin(theta').*sin(si');
            -Forces_b(1,:).*sin(theta')+Forces_b(3,:).*cos(theta')];

%First entry is the moments calculated by the balance or direct calculation
%in the Body Reference Frame.  Balance measures Roll (l), Yaw is about the
%z-axis (n), and Pitch is about the y-axis (m).  Distances from strain
%gages to C.G. are in INCHES.  Moments are in-lbf. See pp. 236-238 of
%Barlow et. al., 3rd ed.

m = Corrected_Data(3,i);

n = Corrected_Data(5,i);

l = Corrected_Data(4,i);

Moments_b(:,i) = [l; m; n];


%Second entry is the conversion from the "Balance Centeric" moments to the
%Wind Reference monments with respect to the Balance Center (bc)

% Moments_w_bc = [Moments_b(1,:).*cos(theta').*cos(si')-Moments_b(2,:).*sin(si')+Moments_b(3,:).*sin(theta').*cos(si');
%                Moments_b(1,:).*sin(si').*cos(theta')+Moments_b(2,:).*cos(si')+Moments_b(3,:).*sin(theta').*sin(si');
%               -Moments_b(1,:).*sin(theta')+Moments_b(3,:).*cos(theta')];

%Finally, the balance centered moments are converted to moments about the
%Model's Center of Mass (cm) or Center of Gravity (CG)

cgdist=sqrt((X_cmb)^2+(Z_cmb)^2); %Obtaining the direct distance between the
                                  %center of the balance and the center of mass
w=atan(-Z_cmb/X_cmb);  %Obtaining the angle between cgdist and the x axes at zero angle of attack

X_cm(i,:)= cos(theta(i,:))*cos(si(i,:))*X_cmb -sin(si(i,:))*
```

```
Y_cmb+sin(theta(i,:))*cos(si(i,:))*Z_cmb ;
Y_cm(i,:)= sin(si(i,:))*cos(theta(i,:))*X_cmb + cos(si(i,:))*Y_cmb + sin(theta(i,:))*sin(si(i,:))*Z_cmb;                %appropriate for very small y_cmb and reasonable si
Z_cm(i,:)= -sin(theta(i,:))*X_cmb+cos(theta(i,:))*Z_cmb ;



% Moments_w_cg_u = [Moments_w_bc(1,:) + Z_cm(i,:)*Forces_w(2,:) + Forces_w(3,:)* Y_cm(i,:);
%                  Moments_w_bc(2,:) - Forces_w(3,:)* X_cm(i,:) + Forces_w(1,:)* Z_cm(i,:);
%                  Moments_w_bc(3,:) - Forces_w(1,:)* Y_cm(i,:) - Forces_w(2,:)* X_cm(i,:)];

% ######################################################################

%VIII.- Calculation of the actual Lift and Drage nondimensional Coefficients, uncorrected for tunnel effects, (Cl
%       and Cd)
% ######################################################################

C_D_u = Forces_w(1,:) ./ (q_Corrected' .* Wing_Area);
C_Y_u = Forces_w(2,:) ./ (q_Corrected' .* Wing_Area);
C_L_u = Forces_w(3,:) ./ (q_Corrected' .* Wing_Area);                    %Keuthe & Chow pg 178
Coefficients = [C_L_u; C_D_u; C_Y_u]';
 Ave_Cl = mean(Coefficients(:,1));
 Ave_Cd = mean(Coefficients(:,2));

end
for ij = 1:row2
  Moments_w_bc(1,ij) = Moments_b(1,ij)*cos(theta(ij,1))*cos(si(ij,1)) - Moments_b(2,ij)*sin(si(ij,1))+ Moments_b(3,ij)*sin(theta(ij,1)).*cos(si(ij,1)) ;
  Moments_w_bc(2,ij) = Moments_b(1,ij).*sin(si(ij,1))*cos(theta(ij,1)) + Moments_b(2,ij)*cos(si(ij,1))+Moments_b(3,ij)*sin(theta(ij,1)).*sin(si(ij,1));
  Moments_w_bc(3,ij) = -Moments_b(1,ij).*sin(theta(ij,1))+Moments_b(3,ij)*cos(theta(ij,1));

 end
for ij = 1:row2
 Moments_w_cg_u(1,ij) = Moments_w_bc(1,ij) + Forces_w(2,ij)*Z_cm(ij,:) + Forces_w(3,ij).* Y_cm(ij,:);
 Moments_w_cg_u(2,ij) = Moments_w_bc(2,ij) -  Forces_w(3,ij)*X_cm(ij,:) + Forces_w(1,ij)* Z_cm(ij,:);
 Moments_w_cg_u(3,ij) = Moments_w_bc(3,ij) -  Forces_w(1,ij)*Y_cm(ij,:) - Forces_w(2,ij)* X_cm(ij,:);

end
% ######################################################################
```

```
%IX           Drag Coefficient Correction
% ######################################################################
% bv/b=0.75 with taper =.2 and  AR=2.7 see figure 10.11--> be =20.234
C_D_o = min(Coefficients(:,2));
C_L_u_sqrd = Coefficients(:,1).^2;
Delta_C_D_w = ((delta * Wing_Area) / X_Section) .* C_L_u_sqrd;
C_D_Corrected = C_D_u' + Delta_C_D_w;

% ######################################################################
%X.-  Angle of Attack due to upwash Correction
% ######################################################################

alpha_before = sample_data(:,1);
alpha =[alpha_before]+[AngleOffsetofModel]; %18APR05 change to 5 for sting block angle, then back to 0 for Aero 517 SU 2005 ************************************
Delta_alpha_w = ((delta * Wing_Area) / X_Section) .* (57.3 * C_L_u);
alpha_Corrected = alpha + Delta_alpha_w';

% ######################################################################
%XI.-  Pitching Moment Correction -- CAREFUL wing vs. full a.c.
% ######################################################################

% tau2 = 0.65;
 c_bar = 9.9/ 12;                       % ft = Mean Chord of wing
% V_bar =  0/ (Wing_Area * c_bar);                        % Horizontal tail volume ratio
% eta_t = 1.0;
% epsilon_o = 0;
% i_t = pi/4;                                              % radians
% i_w = 0;
% Aspect_Ratio_t = Span_t^2 / Tail_Area;
%
% D_epslion_D_alpha = ((2 .* C_L_u) ./ (pi* Aspect_Ratio))';
% epsilon = epsilon_o + (D_epslion_D_alpha .* alpha_Corrected);
% alpha_t = alpha_Corrected - i_w - epsilon + i_t;
% C_L_alpha_t = 0 %((0.1* Aspect_Ratio) / (Aspect_Ratio_t +2)) * 0.8;
% D_Cm_cg_t_D_alpha_t = -C_L_alpha_t* V_bar * eta_t;
% Delta_C_m_cg_t = ((D_Cm_cg_t_D_alpha_t) * (delta*tau2) * (
```

```
    Wing_Area / X_Section) .* (C_L_u * 57.3))';

Cl_w_cg =   Moments_w_cg_u(1,:) ./ (q_Corrected' .* (Wing_Area * Span*12));
Cm_w_cg_u = Moments_w_cg_u(2,:) ./ (q_Corrected' .* (Wing_Area * c_bar*12));
Cn_w_cg =   Moments_w_cg_u(3,:) ./ (q_Corrected' .* (Wing_Area * Span*12));

Cm_w_cg_corrected = Cm_w_cg_u; %-Delta_C_m_cg_t';  %no tail
Corrected_Moment_Coefficients = [Cl_w_cg' Cm_w_cg_corrected' Cn_w_cg'];

%% Obtain MAC value
LinearRange=[0,20]; %from Cl_alpha plot
%Cm alpha loop
    [r]=find(alpha_Corrected>min(LinearRange) & alpha_Corrected<max(LinearRange));
LinAlpha=alpha_Corrected(r);
LinCoefM=Cm_w_cg_corrected(r)';
%figure(111);
%plot(LinAlpha,LinCoefM,'b');
p=polyfit(LinAlpha,LinCoefM,1);
f1 = polyval(p,LinAlpha);
hold on
%plot(LinAlpha,f1,'r--')
title('\it C_m_c_g vs \alpha','FontWeight','bold','FontSize',11); xlabel('Angle of Attack (\alpha)'); ylabel('Pitch Moment Coefficent(C_m_c_g)');
%print -dmeta PITCHING_MOMENT_VS_ALPHA

xl = xlim;
yl = ylim;
xt = 0.55 * (xl(2)-xl(1)) + xl(1) ;%location
yt = 0.90 * (yl(2)-yl(1)) + yl(1);
xt2 = 0.10 * (xl(2)-xl(1)) + xl(1); %location
yt2 = 0.20 * (yl(2)-yl(1)) + yl(1);
yt3 = 0.15 * (yl(2)-yl(1)) + yl(1);
caption = sprintf('y = %f * x + %f', p(1), p(2));
text(xt, yt, caption, 'FontSize', 10, 'FontWeight', 'normal');

explain = sprintf('The Aero center is defined as the location with (on average) no change in moment');
explain2 = sprintf(' with changing alpha. This verifies the iterated MAC location of %.3f inches.', MAC);
text(xt2, yt2, explain, 'FontSize', 8, 'FontWeight', 'normal');
text(xt2, yt3, explain2, 'FontSize', 8, 'FontWeight', 'normal');

hold off
%%

%OBTAINING THE MOMENT COEFFICIENTS CORRECTED ABOUT THE CENTER OF THE
%BALANCE

Cl_w_bc =   Moments_w_bc(1,:) ./ (q_Corrected' .* (Wing_Area *
```

```
Span*12));
Cm_w_bc_u = Moments_w_bc(2,:) ./ (q_Corrected' .* (Wing_Area * c_bar*12));
Cn_w_bc =   Moments_w_bc(3,:) ./ (q_Corrected' .* (Wing_Area * Span*12));

Cm_w_bc_corrected = Cm_w_bc_u ;  %no tail
Corrected_Moment_Coefficients_bc = [Cl_w_bc' Cm_w_bc_corrected' Cn_w_bc'];



% ##########################################################################
%XIII.- PLOTS
% ##########################################################################

%***************1.- C_L VS C_D PLOT ***********************************
 % %***************2.- C_L VS ALPHA PLOT ***********************************

figure(1);
plot(alpha_Corrected,Coefficients(:,1),'b');
% axis([-6 18 -0.4 1.0]);
legend('Slot Model, 800 SLPM, 800 SLPM, 800 SLPM (45 mph)','Location',  'southeast');
grid on;
title('\it C_L vs \alpha, Slot Model, 800 SLPM, 800 SLPM','FontWeight','bold','FontSize',11); xlabel('Angle of Attack (\alpha)'); ylabel('Lift Coefficient (C_L)');
% %print -dmeta C_L_VS_ALPHA_NO_TAIL
% %***************3.- C_D VS ALPHA PLOT ***********************************
%
figure(3);
plot(alpha_Corrected,C_D_Corrected,'b');
grid on;
% axis([-6 18 0 0.2]);
legend('Slot Model, 800 SLPM, 800 SLPM (45 mph)');
title('\it C_D vs \alpha Slot ','FontWeight','bold','FontSize',11); xlabel('Angle of Attack (\alpha)'); ylabel('Drag Coefficient (C_D)');
% print -dmeta C_D_VS_ALPHA_NO_TAIL
% %***************4.- C_D vs. C_L squared PLOT ***********************************
%

 figure(4);
 plot(C_D_Corrected,C_L_u_sqrd,'b');
 legend('Slot Model, 800 SLPM, 800 SLPM (45 mph)');
 grid on;
 title('\it C_D vs. C_L squared','FontWeight','bold','FontSize',11); xlabel('Drag Coefficient, C_D'); ylabel('Lift Coefficient^2 (C_L^2)');
```

```matlab
 %print -dmeta C_L_AND_CD_VS_ALPHA_NO_TAIL
%**************4.- Lift, Drag and side Forces VS ALPHA PLOT ***********************************

figure(5);
plot(alpha_Corrected,Forces_w(1,:),'b.-.',alpha_Corrected,Forces_w(2,:),'r',alpha_Corrected,Forces_w(3,:),'*');
legend('Drag','Side force','Lift')
grid on;
title('\it Lift, Drag and side Forces VS \alpha   (45 mph)','FontWeight','bold','FontSize',11); xlabel('Angle of Attack (\alpha)'); ylabel('Lift, Drag or Side Force');
%print -dmeta FORCES_VS_ALPHA_NO_TAIL

%**************5.- Side Force Coefficient C_y VS ALPHA PLOT ***********************************

figure(7);
plot(alpha_Corrected,Coefficients(:,3),'b.-.');
grid on;
title('\it C_Y vs \alpha  s (45 mph)','FontWeight','bold','FontSize',11); xlabel('Angle of Attack (\alpha)'); ylabel('Side Force Coefficient (C_Y)');
%print -dmeta SIDEFORCE_COEFF_VS_ALPHA_NO_TAIL
% %**************6.- Rolling moment (Cl cg) VS ALPHA PLOT ***********************************

figure(8);
plot(alpha_Corrected,Corrected_Moment_Coefficients(:,1),'b.-.');
grid on;
title('\it C_l (roll moment)vs \alpha ','FontWeight','bold','FontSize',11); xlabel('Angle of Attack (\alpha)'); ylabel('Rolling Moment Coefficent(C_l_c_g)');
%
%**************7.- YAW moment (Cn cg) VS ALPHA PLOT ***********************************

figure(9);
plot(alpha_Corrected,Corrected_Moment_Coefficients(:,3),'b.-.');
grid on;
title('\it C_n_c_g vs \alpha','FontWeight','bold','FontSize',11); xlabel('Angle of Attack (\alpha)'); ylabel('Yaw Moment Coefficent(C_n_c_g)');
print -dmeta YAW_MOMENT_VS_ALPHA_NO_TAIL

% %**************8.- Pitching moment (Cm cg) VS ALPHA PLOT ***********************************
%
figure(10);
plot(alpha_Corrected,Corrected_Moment_Coefficients(:,2),'b');
grid on;
title('\it C_m_c_g vs \alpha','FontWeight','bold','FontSize',11); xlabel('Angle of Attack (\alpha)'); ylabel('Pitch Moment Coefficent(C_m_c_g)');
print -dmeta PITCHING_MOMENT_VS_ALPHA

```

```
%Walker Graphs

figure(11)
plot(alpha_Corrected,NF_test,'g')
hold on
plot(alpha_Corrected,NF_eval,'r')
plot(alpha_Corrected,NF_resolved,'b')
legend('Tunnel Data','Tare Data','Subtracted Data')
xlabel('Angle of Attack (\alpha in degrees)'); ylabel('Normal Force (**UNITS**)');
grid on;
title('Normal Force, Slot Config')
hold off

figure(12)
plot(alpha_Corrected,AF_test,'g')
hold on
plot(alpha_Corrected,AF_eval,'r')
plot(alpha_Corrected,AF_resolved,'b')
legend('Tunnel Data','Tare Data','Subtracted Data')
grid on;
title('Axial Force, Slot Config')
xlabel('Angle of Attack (\alpha in degrees)'); ylabel('Axial Force (**UNITS**)');
hold off

figure(13)
plot(alpha_Corrected,PM_test,'g')
hold on
plot(alpha_Corrected,PM_eval,'r')
plot(alpha_Corrected,PM_resolved,'b')
grid on;
legend('Tunnel Data','Tare Data','Subtracted Data')
title('Pitch Moment, Slot Config')
xlabel('Angle of Attack (\alpha in degrees)'); ylabel('Pitch Moment (**UNITS**)');
hold off

%% corrected vs uncorrected plots
% Corrected_Data(:,i)= [NF(n);AF(n);PM(n);RM(n);YM(n);SF(n)];
figure(14)
plot(alpha_Corrected,NF_resolved)
hold on
plot(alpha_Corrected,Corrected_Data(1,:)')
legend('Uncorrected NF', 'Corrected NF')
title('Normal Force, With and Without Corrections')

figure(15)
plot(alpha_Corrected,AF_resolved)
hold on
plot(alpha_Corrected,Corrected_Data(2,:)')
legend('Uncorrected AF', 'Corrected AF')
title('Axial Force, With and Without Corrections')

figure(16)
plot(alpha_Corrected,PM_resolved)
hold on
```

```
plot(alpha_Corrected,Corrected_Data(3,:)')
legend('Uncorrected PM', 'Corrected PM')
title('Pitch Moment, With and Without Corrections')
```

Bibliography

1. R. J. Salmi, "Low-Speed Longitudinal Characteristics of a 45 degree Sweptback Wing of Aspect Ratio 8 with High-Lift and Stall-Control Devices at Reynolds Numbers from 1,500,000 to 4,800,000," *National Advisory Committee for Aeronautics*, vol. RM L51J04, 1952.

2. G. L. Pratt and E. R. Shields, "Low Speed Longitudinal Characteristics of a 45 Degrees Swept Back Wing," *NACA Research Memorandum*, no. February, pp. 1–32, 1952.

3. R. Seele, E. Graff, J. Lin, and I. Wygnanski, "Performance enhancement of a vertical tail model with sweeping jet actuators," *51st AIAA Aerospace Sciences Meeting including the New Horizons Forum and Aerospace Exposition 2013*, no. January, pp. 1–19, 2013.

4. M. M. Walker, K. Hipp, S. I. Benton, and J. P. Bons, "Control of Post Stall Airfoil Using Leading-Edge Pulsed Jets," *AIAA Journal*, vol. 55, pp. 365–376, 2017.

5. M. Walker and J. P. Bons, "The Effect of Passive and Active Boundary-Layer Fences on Swept-Wing Performance at Low Reynolds Number," in *2018 AIAA Aerospace Sciences Meeting*, 2018.

6. J. Winslow, H. Otsuka, B. Govindarajan, and I. Chopra, "Basic understanding of airfoil characteristics at low Reynolds numbers (104–105)," *Journal of Aircraft*, vol. 55, no. 3, pp. 1050–1061, 2018.

7. M. A. McVeigh and E. Kisielowski, "A Design Summary of Stall Characteristics of Straight Wing Aircraft," *NASA Contractor Report*, vol. 1648.

8. C. W. Harper and R. L. Maki, “A Review of the Stall Characteristics of Swept Wings,” *NASA Technical Note*, vol. 2373, no. July 1964, 1964.

9. P. Tewes, L. Taubert, and I. Wygnanski, “On the effect of sweep on separation control,” *AIAA AVIATION 2014 -7th AIAA Flow Control Conference*, no. June, pp. 1–18, 2014.

10. M. M. Walker, “Replicating the Effects of a Passive Boundary-Layer Fence via Active Flow Control,” PhD Dissertation, The Ohio State University, 2018.

11. E. C. Polhamus, “Sharp-Edge Delta Wings Based O N a Leading-Edge-Suction Analogy,” *NATIONAL AERONAUTICS AND SPACE ADMINISTRATION For*, p. 18, 1966.

12. W. Shyy and H. Liu, “Flapping Wings and Aerodynamic Lift: The Role of Leading-Edge Vortices,” *AIAA Journal*, vol. 45, no. 12, pp. 2817–2819, 2007.

13. C. P. Ellington, C. van den Berg, A. P. Willmott, and A. L. R. Thomas, “Leading-edge vortices in insect flight,” *Nature*, vol. 384, no. 6610, pp. 626–630, 1996. [Online]. Available: https://doi.org/10.1038/384626a0

14. C. W. Smith, J. N. Ralston, and H. W. Mann, “Aerodynamic Characteristics of Forebody and Nose Strakes Based on F-16 Wind Tunnel Test Experience.” *NASA Contractor Reports*, vol. 1, no. 3053, 1979.

15. R. J. Salmi, “Effects of Leading-Edge Devices and Trailing-Edge Flaps on Longitudinal Characteristics of Two 47.7 degreee Sweptback Wings of Aspect Ratios 5.1 and 6.0 at a Reynolds Number of 6.0 x 106,” *National Advisory Committee for Aeronautics*, vol. NACA RM, no. L50F20, pp. 1–77, 1952.

16. L. Egenburg and A. Saweljew, “”Das G im Wörtchen ”MiG”: Michail Josifowitsch Gurjewitsch”.” *Fliegerrevue*, vol. 1, 1993.

17. USAF, “T-1A Jayhawk.”

18. É. Lorenceau, D. Quéré, and J. Eggers, “Air entrainment by a viscous jet plunging into a bath,” *Physical Review Letters*, vol. 93, no. 25, pp. 1–4, 2004.

19. N. Chandler and J. Strickland, “How the Dyson Bladeless Fan Works.”

20. W. Liebe and W. Eisenmann, “Vorrichtung zum Verhindern der Ausbreitung von Stroemungsstoerungen an Flugzeugfluegeln (Device for preventing the spread of flow disturbances on aircraft wings),” 1938.

21. J. P. Crowder, “In-flight propeller flow visualization using fluorescent minitufts,” *NASA Langlet Research Center Flow Visualization and Laser Velocimetry*, p. 91 95, 1982.

22. D. A. Solfelt, M. D. Williams, M. F. Reeder, and R. C. Maple, “Model, Simulation and Flight Tests for a T-38 Talon with Wing Fences,” *Journal of Aircraft*, vol. 47, p. 72, 2010.

23. A. Seifert, A. Darabi, and I. Wygnanski, “Delay of Airfoil Stall by Periodic Excitation,” *Journal of Aircraft*, vol. 335, no. 4, pp. 691–698, 1996.

24. L. G. Pack and A. Seifert, “Effects of sweep on the dynamics of active separation control,” *Aeronautical Journal*, vol. 107, no. 1076, pp. 617–629, 2003.

25. T. Naveh, A. Seifert, A. Tumin, and I. Wygnanski, “Sweep effect on parameters governing control of separation by periodic excitation,” *Journal of Aircraft*, vol. 35, no. 3, pp. 510–512, 1998.

26. D. Greenblatt and A. E. Washburn, “Influence of finite span and sweep on active flow control efficacy,” *AIAA Journal*, vol. 46, no. 7, pp. 1675–1694, 2008.

27. J. B. Barlow, W. H. Rae, and A. Pope, *Low-Speed Wind Tunnel Testing*, 3rd ed. Wiley-Interscience, 1999.

28. R. P. Hallion, "NASA's Contributions to Aeronautics," in *Sweep and Swing: Reshaping the Wing for the Jet and Rocket Age*, 2010.

29. M. Duvelleroy, "Airbus reveals its blended wing aircraft demonstrator," 2020.

30. H. Ceron-Munoz, D. Diaz-Izuierdo, J. Solarte-Pineda, and F. Catalano, "Aerodynamic Interference of Wingtip and Wing Devices on Blended Wing Body Model," in *29th Congress of the International Council of Aeronautical Sciences*, St. Petersburg, Russia, 2014, pp. 1–8.

31. J. P. Crowder, "Tufts," in *Handbook of Flow Visualization*, 2nd ed., W. J. Yang and R. H. Bedford, Eds. New York, NY: Taylor & Frances, 2001, pp. 131–161.

32. J. S. Kline and McClintock F. A., "Describing Uncertainties in Single-Sample Experiments," *ASME Journal of Mechanical Engineering*, pp. 3–8, 1953.

33. D. Dobney, P. Hanson, and S. Fiddes, "The minituft surface flow visualization method," *Royal Aircraft Establishment*, no. Tech Memo Aero 2038, 1985.